Grenville–age orogeny in central Dronning Maud Land, East Antarctica: constraints from new zircon U–Pb data from Jutulsessen, Gjelsvikfjella

Master of science thesis in Geoscience

Helene Marie Knudsen

Department of Earth Science
University of Bergen

June 2020

Abstract

The Mesoproterozoic Maud Belt within central Dronning Maud Land, East Antarctica, preserve important information about the tectonic setting along the eastern margin of the Kalahari Craton and is an essential key in both the Rodinia and Gondwana supercontinent. So far, limited geochronological data is covering the Grenville–age magmatic history, and more data is needed to get a better understanding of the formation of the Maud Belt. In this study, new SIMS U–Pb zircon ages are revealed from six high–grade granitoids conducted within the Jutulsessen nunataks in Gjelsvikfjella (west–central part of the Maud Belt). Five of the investigated samples report Grenville–age magmatism between ca. 1179–1061 Ma, while the remaining sample yields a Pan–African crystallization age at ca. 497 Ma. The oldest age group of ca. 1179–1131 Ma is considered to represent the initial volcanic arc magmatism forming the Maud arc, while the youngest Grenville–age of ca. 1061 Ma corresponds to a subsequent magmatic period of granitic intrusions. These data thus confirm Grenville–age magmatism in the area. Further, one potential inherited zircon core, ca. 1240 Ma, is detected from one of the Mesoproterozoic samples and may represent the involvement of older crustal components. Late Mesoproterozoic metamorphism has been recorded at ca. 1128 Ma and 1105 Ma from zircon rim overgrowths. This indicates metamorphism prior to the major metamorphic event between 1090–1030 Ma. However, the metamorphic ages do coincide with increased magmatic activity within the Maud Belt, and could thus reflect thermal imprints related to igneous emplacements during a magmatic pulse.

The Mesoproterozoic basement was later intensely reworked during late Neoproterozoic–early Paleozoic times, associated with the collisional phase of Gondwana. One of the Mesoproterozoic rocks documents this event by metamorphic zircon rim overgrowths around 549 Ma. Subsequently, the central Dronning Maud Land is suggested to have experienced extensional orogenic collapse, which led metamorphic imprints and post–tectonic magmatism, here detected from two samples at ca. 496 Ma and 497 Ma, respectively.

Acknowledgements

This thesis is part of my Master of Natural Science degree in Geoscience, Geology, at the Department of Earth Science, University of Bergen. Prof. Joachim Jacobs (UiB) and Ph.D. Cheng–Cheng Wang (UiB) have been supervisors for this project. I want to thank my main supervisor, Prof. Joachim Jacobs, for giving me the opportunity to work with this exciting project. I greatly appreciate his guidance and feedback throughout the project, and for always being available questions whenever needed. A big thanks also goes to my co–supervisor Cheng–Cheng Wang for helpful assistance, discussions, and constructive feedback during my writing of this thesis.

I would also like to thank Irina Dimitri for preparing my thin sections. Thanks to Leif–Erik Pedersen and Ida Marie Gabrielsen for kindly helping and introducing me to all stages of mineral separation.

Furthermore, I would like to thank all my fellow students for good company during five wonderful years at UiB, and my fellow students at "Hovedkvarteret". Thanks to Sara Kverme for reading through my text and help to improve my writing. A special thanks to my boyfriend, Lars, for his endless support and encouragement through this challenging work. Lastly, thanks to my friends and family for being supportive.

Helene Marie Knudsen
Bergen, May 2020

CONTENTS

1 Introduction

1.1 Study area

The investigated samples in this study were collected within the Jutulsessen nunataks located in the remote landscape of central Dronning Maud Land (cDML), East Antarctica (Fig. 1.1A). The mountain range of central Dronning Maud Land lies roughly parallel to the coastline and is exposed ca. 200–250 km inland (Owada et al., 2003; Elvevold et al., 2019). Jutulsessen claims an area between latitude 71°59'S to 72°07'S and longitude 02°51'E to 02°28'E. The highest mountain peak is approximately 2370 m a.s.l (Shrivastava et al., 2014). On the western side of Jutulsessen lies Troll research station operated by the Norwegian Polar Institute. The Jutulsessen Mountains are geographically a part of Gjelsvikfjella, which are bounded to the west by Mühlig–Hofmannfjella, while towards the east lies the H. U. Sverdrupfjella followed by the Jutulstraumen rift (Fig. 1.1B).

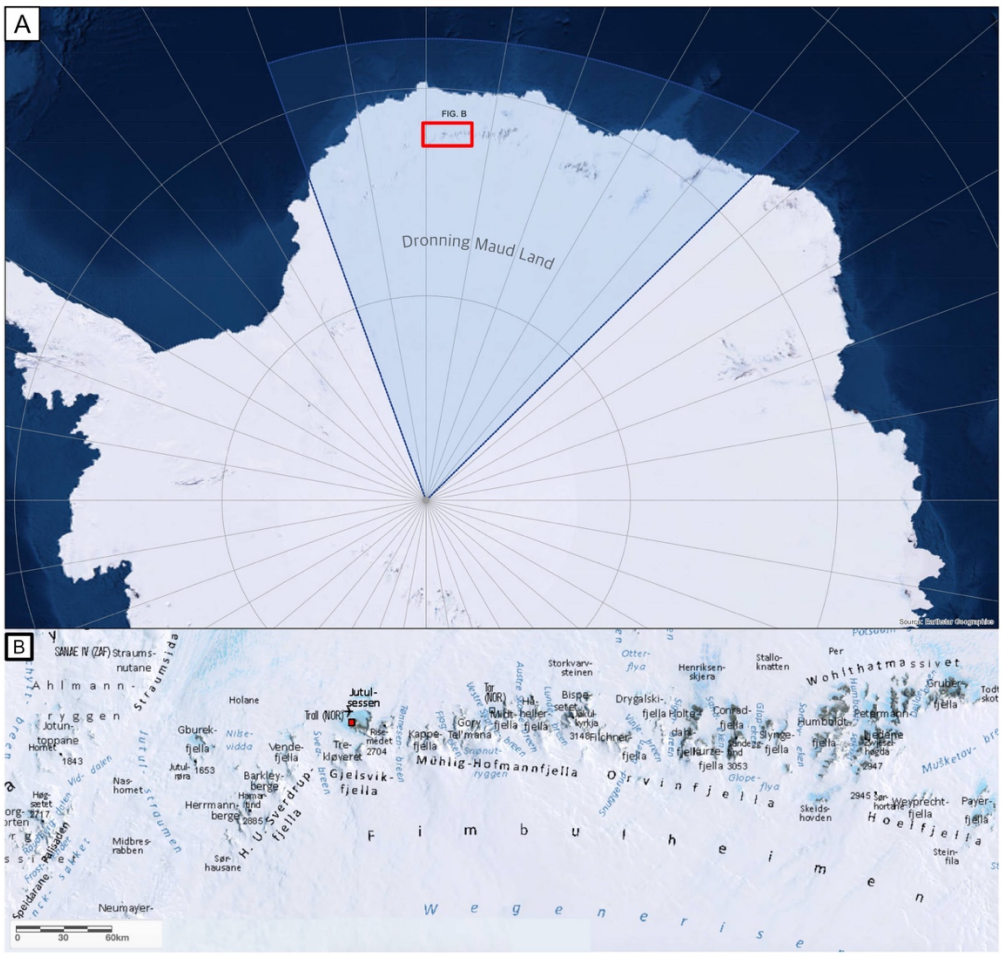

Figure 1.1: (A) An overview map of Dronning Maud Land, Antarctica. Modified based on Esri ArcMap data. (B) An overview map of the study area, Dronning Maud Mountains, East Antarctica. Red box: indicates where the samples were collected, Jutulsessen. Modified after Norsk Polarinstitutt, 2020. Downloaded from: https://geologi.npolar.no/Html5Geo/index.html?viewer=Geology_DML.

1.2 Previous research

The first geological studies carried out for central Dronning Maud Land were performed by the Norwegian–British–Swedish expedition in 1949–1952, which produced a simple geological map (Roots, 1953). Subsequently, in the 1960s, Russian geologists did research in the areas of Gjelsvikfjella and Mühlig–Hofmann–Gebirge and published the first geological maps, including structural, geochemical and petrological data (Ravich and Soloviev, 1966; Ravich and Kamenev, 1972; Kamenev et al., 1990). Later, Indian and German geologists have complemented with information from the area (Joshi et al., 1991; Bohrmann and Fritzsche, 1995). In more recent times, numerous publications from the central Dronning Maud Land using U–Pb zircon dating has revealed significant components of Grenville–age (~1100 Ma) basement rocks, which later were reworked during the Pan–African (~500 Ma) tectono-thermal event (e.g. Jacobs et al., 1998; Paulsson and Austrheim, 2003; Jacobs et al., 2003b; Jacobs et al., 2003c; Wang et al., 2020). The first major metamorphic event in the central Dronning Maud Land yields U–Pb ages of ca. 1080 Ma and is consistent with the formation of Rodinia (Jacobs et al., 1998; Bisnath et al., 2006). No further metamorphic or magmatic activity is recorded until the emplacement anorthosite and charnockite intrusions around 600 Ma within the Orvin–Wohlthat Mountains (Jacobs et al., 1998). Later, the basement rocks were reworked during the assembly of Gondwana, which formed the East African–Antarctic Orogen (EAAO). The geochronological investigation by Jacobs et al. (1998) suggests two different periods of metamorphism between ca. 570–550 Ma and ca. 530–515 Ma, reaching up to granulite facies conditions. Post–tectonic activity in central Dronning Maud Land is recognized by the emplacement of a metagranodiorite body, major charnockite intrusions, smaller granite and gabbro bodies, and voluminous granitoids bracketed between ca. 530 to 485 Ma (Mikhalsky et al., 1997; Jacobs et al., 1998; Bisnath et al., 2006; Jacobs et al., 2008a). Geochronological work examined in the study area, Jutulsessen nunataks, is limited. The first data presented was reported by Ohta et al. (1990) and Moyes (1993), where a charnockite intrusion was dated ca. 500 Ma with Rb/Sr whole–rock method, and a granite gneiss gave the age of ca. 1150 Ma based on Sm/Nd whole–rock age, respectively. Later work has reported Mesoproterozoic protolith ages with the oldest dated at 1163±6 Ma and the youngest at 1096±8 Ma (Jacobs et al., 2003b; Paulsson and Austrheim, 2003; Bisnath et al., 2006). Mesoproterozoic metamorphism is also reported from a migmatite gneiss (~1070 Ma) (Bisnath et al., 2006). The Pan–African event in the area has been reported by a post–tectonic intrusion (Stabben) at ca. 500 Ma (Paulsson and Austrheim, 2003). In addition, several of the Mesoproterozoic rocks indicate Pan–African

metamorphism and evidence of partial melting (Paulsson and Austrheim, 2003; Bisnath et al., 2006; Jacobs et al., 2008a).

1.3 Research objectives

The Grenville–age history of the Maud Belt is sparse in geochronological data. The limitation is highly related to the later well–documented orogenic event (EAAO) during Pan–African times, which led to a late Neoproterozoic–early Paleozoic high–grade metamorphic overprint of the Mesoproterozoic basement rocks. The Maud Belt needs further constraints to get a clear interpretation of its formation and evolution during Mesoproterozoic times. In addition, the Grenville–age history of Dronning Maud Land preserves crucial information regarding the assembly of Rodinia supercontinent. For this thesis, six samples were selected for further investigations to supplement geochronological data from a limited area, Jutulsessen, Gjelsvikfjella. The aim of the study is to record Grenville–age magmatism in the area of Jutulsessen in order to provide new precise geochronological data to this limited area. Furthermore, new U–Pb zircon data will help to better understand the Grenville–age magmatic history of the Maud Belt.

2 Geological background

2.1 Dronning Maud Land: geological domains

The geology of Dronning Maud Land (DML), East Antarctica, is separated into three main geological domains (Fig. 2.1). The geological domains are representing the Dronning Maud Land area from west to east:

(1) **The Grunehogna Craton**: represents a fragment of the Archaean Proto–Kalahari Craton, ca. 3.0 Ga granitic basement (Groenewald et al., 1995; Marschall et al., 2010).

(2) **The Maud Belt:** is a Grenville–age orogenic belt comprising of Heimefrontfjella, Kirwanveggen, H.U. Sverdrupfjella, Gjelsvikfjella, Mühlig–Hofmannfjella, and the Orvin–Wohlthat Mountains. Geological and geochronological information from these nunataks reveals intrusive and metasupracrustal rocks forming around 1170 to 1090 Ma (Arndt et al., 1991; Jacobs et al., 1998; Jacobs et al., 2003b; Jacobs et al., 2003c; Paulsson and Austrheim, 2003; Board et al., 2005; Bisnath et al., 2006; Grantham et al., 2011; Wang et al., 2020). Between ca. 1090–1050 Ma, voluminous granitic batholiths, plutons, and felsic sheets intruded the basement, accompanied by high–grade metamorphism up to granulite–facies. These features have been detected in various parts of western and central Dronning Maud Land (Arndt et al., 1991; Jacobs et al., 1998; Jacobs et al., 2003b; Jacobs et al., 2003c; Bauer et al., 2003b; Paulsson and Austrheim, 2003; Bisnath et al., 2006; Board et al., 2005; Grantham et al., 2011). In late Neoproterozoic–early Paleozoic times, the Mesoproterozoic crust again experienced intense high–grade tectono–thermal metamorphism related to the formation of the East African–Antarctic Orogen (~550 Ma) during the Gondwana assembly (Mikhalsky et al., 1997; Jacobs et al., 1998; Jacobs et al., 2003a; Bauer et al., 2003b; Paulsson and Austrheim, 2003; Jacobs and Thomas, 2004).

(3) **The Tonian Oceanic Arc Super Terrane (TOAST)**: is characterized by juvenile oceanic arcs that represent remnants from the Mozambique Ocean, ca. 1000–900 Ma. During the final amalgamation of Gondwana, the arcs were attached to western–eastern DML (eastern Kalahari) (Jacobs et al., 2015).

Domain (1) and (2) are related to Rodinia. In western DML, within domain (1) and (2), the Heimefront Shear Zone represents the boundary between the Natal Belt and the Maud Belt, in addition to being the western orogenic front of the East African–Antarctic Orogen during the formation of Gondwana, around 550 Ma (Stern, 1994; Jacobs et al., 1996; Jacobs et al., 2003c). Domain (2) and (3) are separated by the Forster Magnetic Anomaly (Riedel et al., 2013),

interpreted to represent the collision suture of the eastern Kalahari margin and the TOAST (Jacobs et al., 2015). The geological domains constitute an area of complex evolution history, involving both amalgamation and fragmentation of different supercontinents. The following sections will describe the geological evolution of Dronning Maud Land, and the final section will summarize the regional geology reported for western, central, and eastern Dronning Maud Land.

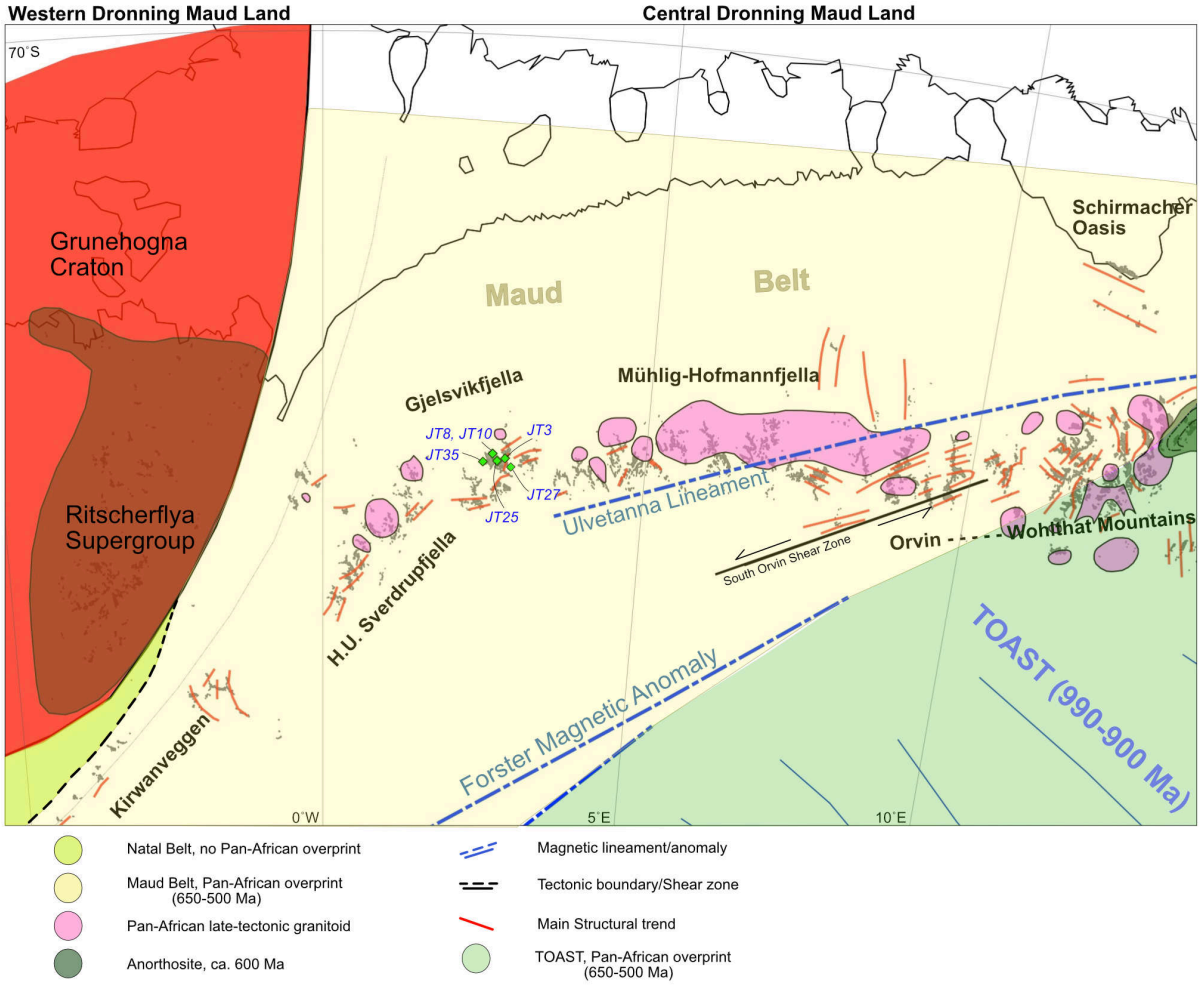

Figure 2.1: An overview map of Dronning Maud Land separated into three main geological domains; Grunehogna Craton, Maud Belt, and Tonian Oceanic Arc Super Terrane (TOAST). The study area is located within the Gjelsvikfjella, central Dronning Maud Land, where the sample localities, with corresponding sample number, are marked by green squares.

2.2 Amalgamation of the Kalahari Craton

The Proto–Kalahari Craton is referred to as an Archean–Paleoproterozoic nucleus, including the Kaapvaal, Zimbabwe, and Grunehogna cratons. During the Mesoproterozoic, the Proto–Kalahari Craton experienced substantial growth, forming into the Kalahari Craton (Jacobs et al., 2008b). Today, the Kalahari Craton is exposed as a fragment within Dronning Maud Land, representing the Grunehogna Craton and the Maud Belt. The major crustal growth of the Proto–Kalahari Craton was mainly generated by island arcs developing outside the margins of the craton that later accreted onto the craton during the final Rodinia assembly (Fig. 2.2) (Jacobs et al., 2008b). The basement of west and central Dronning Maud Land is suggested to have formed through continental arc magmatism along the eastern margin of Proto–Kalahari (Bisnath et al., 2006; Wang et al., 2020). Along the southern margin, accretion of oceanic arcs formed the basement rock of the Namaqua–Natal Belt, which became attached to the Proto–Kalahari during the amalgamation of Rodinia and the following continent–continent collision with Laurentia around 1100–1000 Ma (Jacobs et al., 2003b).

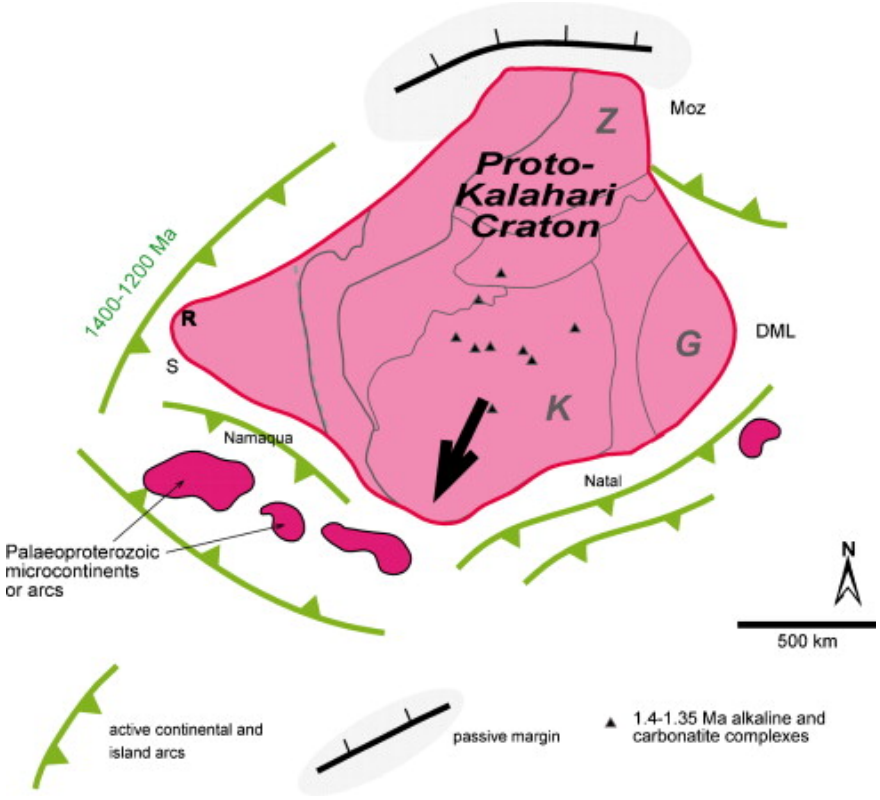

Figure 2.2: Illustration of Proto–Kalahari (pink), ca. 1200 Ma, showing the active southwest and south–southeast margins. Arc terranes (dark pink) are starting to develop outside the margins. Abbreviations: Z – Zimbabwe Craton; Moz – northern Mozambique; R – Rehoboth; G – Grunehogna Craton; DML – Dronning Maud Land; S – Sinclair; K – Kaapvaal Craton. From Jacobs et al. (2008b).

2.2.1 The formation of the Maud Belt (west and central Dronning Maud Land)

Reconstructions of Rodinia and Gondwana commonly position the Maud Belt juxtaposed to the eastern margin of the Proto–Kalahari, while the entire southern margin is rimmed by the Namaqua–Natal Belt (Groenewald et al., 1995; Jacobs and Thomas, 2004; Jacobs et al., 2008b). The Namaqua–Natal Belt, together with the Maud Belt, was initially interpreted as a continuous orogen, formed by island arc accretion processes along the Proto–Kalahari margin (Jacobs et al., 1993; Groenewald et al., 1995; Jacobs et al., 2008b). The Natal Belt is considered to be formed by juvenile oceanic arcs, as evidenced by geochemical signatures and typical OIB–patterns (Arima et al., 2001), with subduction polarity outboard of the Proto–Kalahari margin and toward the arcs (Jacobs and Thomas, 1994). The pre–tectonic Mesoproterozoic basement rocks from Heimefrontfjella to central Dronning Maud Land comprises of paragneisses and bimodal metavolcanic rocks (~1170–1140 Ma) and intrusive meta–tonalitic rocks (~1140–1130 Ma) indicating similar ages as found in the Natal Belt (Arndt et al., 1991; Jacobs et al., 1998; Paulsson and Austrheim, 2003; Board et al., 2005). Earlier studies mainly report an overall calc–alkaline signature and relatively juvenile source character with Mesoproterozoic to late Paleoproterozoic model ages for the Maud Belt, consistent with the interpretation of a Rodinia–distant island volcanic arc terrane (Arndt et al., 1991; Moyes, 1993; Jacobs et al., 1998; Bauer et al., 2003b). However, recent studies verify independent tectonic evolutions of the two belts and question the previously suggested geodynamic model. The two belts record distinct differences related to their Grenville–age magmatic history, subduction polarity and tectonic regime (Fig. 2.3) (Bisnath et al., 2006; Grosch et al., 2007; Grantham et al., 2011; Mendonidis et al., 2015; Wang et al., 2020). The Natal Belt comprises of supracrustal gneisses, granitoids, and intrusive rocks, recording arc magmatism from ca. 1200 Ma (McCourt et al., 2006). In contrast, the Maud Belt does not record any magmatism before ca. 1170 Ma and typically shows igneous crystallization ages of ca. 1100 Ma, indicating two independent magmatic timings for the belts. Any form of contiguity between the two belts was probably not established before the end of Mesoproterozoic. High–grade metamorphism dated at ca. 1090–1030 Ma is estimated as the continent–continent collision event between Proto–Kalahari Craton and possibly Laurentia and strongly affected both belts (Bisnath and Frimmel, 2005; Bisnath et al., 2006). Mendonidis et al. (2015) report a correlating evolution history after their juxtaposition by widespread emplacement of voluminous granitoids and charnockites at ca. 1035 Ma (e.g. in Kirwanveggen and Oribi Gorge Suit in Natal). The tectonic boundary between the Natal Belt and Maud Belt is interpreted to be located between the Vardeklettane (west) and the Sivorg (east) Terrane in Heimefrontfjella, called the Heimefront Shear Zone (Jacobs et al., 1996). This

structure forms a dextral shear zone which separates basement rocks that are affected by late Neoproterozoic–early Paleozoic crustal reworking, related to the assembly of Gondwana, in the east (Maud Belt) from crust unaffected by the late Neoproterozoic–early Paleozoic overprinting in the west (Natal Belt) (Jacobs and Thomas, 2004; Golynsky and Jacobs, 2001). The Vardeklettane Terrane shares geological similarities with the Margate Terrane within the Natal Belt and is interpreted as a counterpart of the Natal Sector in Gondwana reconstructions (Bauer et al., 2003c; Mendonidis et al., 2015).

The Maud Belt is juxtaposed to the Archean Grunehogna Craton in the west. The craton is overlain by volcano–sedimentary rocks of Mesoproterozoic components, called the Ritscherflya Supergroup (Marschall et al., 2010). The Ritscherflya Supergroup is interpreted as a possibly back–arc basin between the Grunehogna Craton and the volcanic Maud arc (Grosch et al., 2007). Tuff layers found in the Ritscherflya Supergroup (Ahlmannryggen ~1130 Ma) (Frimmel, 2004) are synchronous with the igneous activity at ca. 1100 Ma in adjacent areas of the Maud Belt (Arndt et al., 1991; Jacobs et al., 1998; Jacobs et al., 2003b; Jacobs et al., 2003c; Paulsson and Austrheim, 2003; Board et al., 2005; Bisnath et al., 2006; Grantham et al., 2011). The Ritscherflya Supergroup was intruded by the Borgmassivet Suit sills (~1107 Ma), which are mafic–ultramafic in composition (reviewed by Hanson et al., 2006). High–grade metamorphism is detected within areas close to the Grunehogna Craton, e.g. in Heimefrontfjella (~1104 Ma) (Arndt et al., 1991), and was probably affected by the igneous events within the Proto–Kalahari Craton. The Borgmassivet Suits were emplaced at the syn–diagenesis stage and experienced subsequent metamorphic overprint reaching up to greenschist–facies, synchronous with amphibole and granulite–facies conditions recorded in the Maud Belt (~1080 Ma) (Jacobs et al., 1998; Jacobs et al., 2003b). Recent investigations of the detrital zircon age spectra of the sedimentary rocks demonstrates a large population with crystallization ages (~1130 Ma) close to the deposition age (~1130–1107 Ma) with input of older detritus (~3445 Ma) (Marschall et al., 2013). According to tectonic regime models demonstrated by Cawood et al. (2012), the detrital zircon age spectrum recorded within the Ritscherflya Supergroup reflects a convergent marginal setting. This supports an inward subduction model at the eastern margin of the Proto–Kalahari (Fig. 2.3), as previously suggested by e.g. Bisnath et al. (2006) and Grosch et al. (2007), where the Maud Belt generates as a continental or island volcanic arc. These interpretations are contradictory to e.g. Jacobs et al. (2008b) suggesting a passive margin with outward subduction, favoring a similar geodynamic setting for the Maud Belt as for the Namaqua–Natal Belt. Several studies with tectonic models favoring inboard subduction

underneath the Proto–Kalahari Craton consider the emplacement of the Borgmassivet Suits (~1107 Ma), within the Ritscherflya Supergroup, as a result of an extensional setting caused by subduction activity underneath the Proto–Kalahari Craton (Grosch et al., 2015). Other workers correlate the Borgmassivet Suits with coeval intrusions found within the Umkondo Group of southern Africa based on geochemical, paleomagnetic and geochronological data. The intrusions are considered to be the result of intraplate magmatism forming a large igneous provinces (LIPs) between 1112 to 1106 Ma within the Proto–Kalahari Craton (Hanson et al., 2004).

As mentioned above, contrasting models have been suggested to explain the tectonic regime of the Maud Belt. Whether the Maud Belt was formed from an island volcanic arc or continental volcanic arc has not come to an agreement. Previous work, e.g. Jacobs et al. (1998), interpreted the Maud Belt as juvenile without any significant contributions of older crustal components and thus proposed the Maud arc to stem from an island arc volcanic setting. However, as more research has been conducted in the Maud Belt, the result reveals older inherited and detrital zircons, ranging from ca. 2100–1200 Ma and Nd model ages up to Archean ages are constrained from various metamorphic and metasedimentary rocks within the Heimefrontfjella (Arndt et al., 1991; Ksienzyk and Jacobs, 2015), H.U. Sverdrupfjella (Grosch et al., 2007), Gjelsvikfjella (Bisnath et al., 2006), and the Orvin–Wohlthat Mountains (Wang et al., 2020). Bisnath et al. (2006) interpret the Maud arc to form adjacent to the Proto–Kalahari margin rather than as an oceanic island arc based on the presence of older inherited zircons and evidence of Archean Nd model ages detected throughout the Maud Belt in combination with evidence of synchronous sedimentation of the Ritscherflya Supergroup and volcanic activity of the Maud Belt. Grosch et al. (2007) investigated the trace elements and geochemical signatures of amphiboles from the Maud Belt (Heimefrontfjella, H.U. Sverdrupfjella, and Gjelsvikfjella). Their result is consistent with formation in a continental volcanic arc setting. In addition, newer publications propose that the involvement of older crustal components in Grenville–age magmas is of significantly larger amounts than previously assumed, favoring a tectonic setting involving a continental volcanic arc system. Furthermore, zircon Hf–O isotopic data performed by Wang et al. (2020) indicates that both reworked and juvenile input are involved within the Grenville–age magmatism from voluminous granitoids in Gjelsvikfjella and the Orvin–Wohlthat Mountains. In general, the Orvin–Wohlthat Mountains typically reveal juvenile magmas with Mesoproterozoic model ages, whereas the samples of Gjelsvikfjella indicate a significant involvement of older crust with Paleoproterozoic ages. However, the oldest sample of the

Orvin–Wohlthat Mountains shows both juvenile and older crustal input. The younger samples show an increasing trend of juvenile mantle–derived components, probably reflecting a continental margin that is experiencing continuous subduction processes. The overall findings from Wang et al. (2020) concludes with strong evidence for the involvement of recycled crust in central Dronning Maud Land, which supports a convergent continental arc system at the eastern margin of Proto–Kalahari, possibly as an Andean–type continental arc system. During this setting, the subduction underneath the craton is believed to experience tectonic switching (repeating advancing and retreating of the subduction zone trench) (Collins, 2002). In an advancing mode, the subduction zone typically shows evolved Hf values and indicates larger amounts of crustal involvement in the magma source. In contrast, more juvenile magmas are favored when the subduction zone is in retreating mode, causing crustal thinning of the overriding plate and allows magma migration (Boekhout et al., 2015). The latter setting is suggested to reflect the juvenile input and the lower amount of recycled crust, as demonstrated in the Orvin–Wohlthat Mountains (Wang et al., 2020).

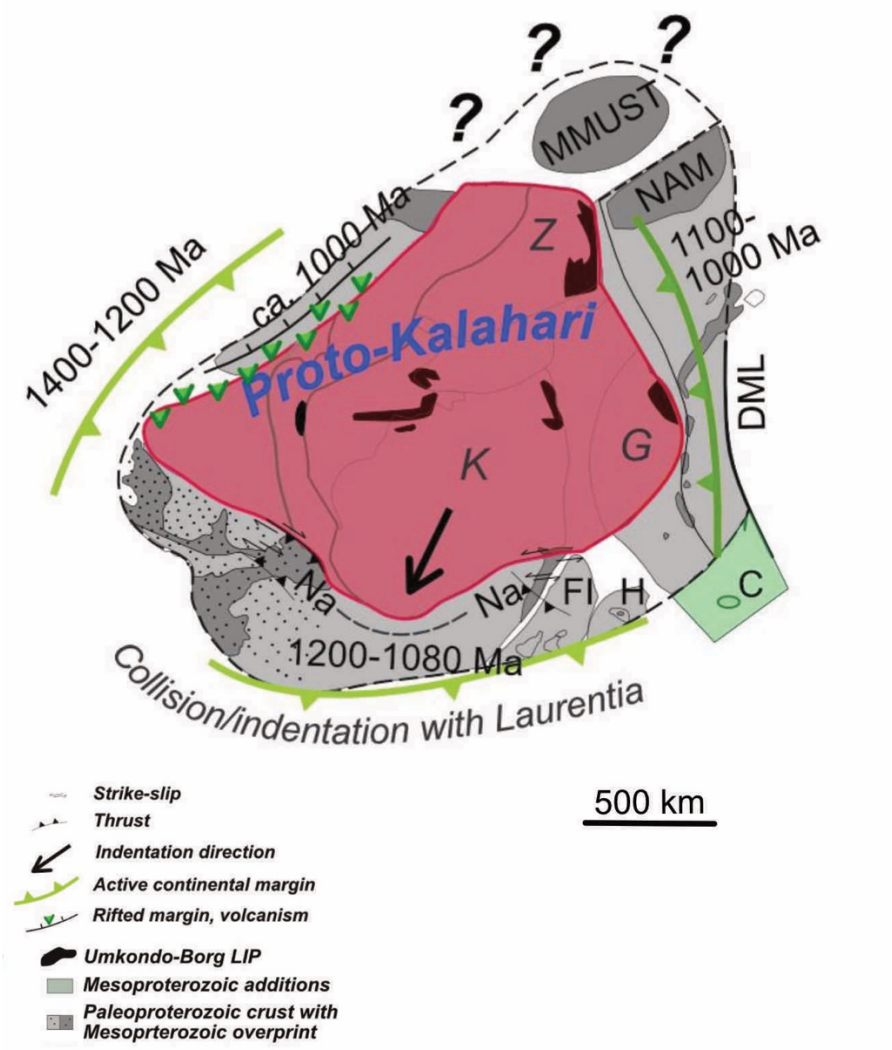

Figure 2.3: An illustration depicting the Proto–Kalahari Craton as it experiences crustal addition at ca. 1080 Ma with the Namaqua–Natal Belt (Na–Na) and Maud Belt along its margins. Initially, the Maud Belt was interpreted as a continuation of the Na–Na Belt. However, recent research points out distinct differences in ages, subduction polarities, and tectonic regimes. The eastern margin along the Maud Belt is representing an active continental margin with inboard subduction underneath the craton, whereas the southern margin along the Namaqua–Natal Belt shows outboard subduction with an accretion of arcs and microcontinents. Abbreviations: C – Coats Land block, DML – Dronning Maud Land, FI – Falk Islands, G – Grunehogna Craton, H – Haag Nunatak, K – Kaapvaal Craton, MMUST – Marup–Malawi–Unango south Tanzania Terrane, Na–Na – Namaqua–Natal Belt, Z – Zimbabwe Craton. Figure from Jacobs et al. (2020) (after Jacobs et al. (2008b)).

2.3 Kalahari Craton's position within supercontinent Rodinia

The assembly of the supercontinent Rodinia caused worldwide orogenic events from Mesoproterozoic to early Neoproterozoic times (~1300–900 Ma) (Li et al., 2008). The event gave birth to one of largest orogen throughout Earth's history – the Grenville Orogen. The Grenville Orogen is mainly exposed along the eastern margin of Laurentia and represents a Himalayan–type orogen. Reconstructions of Rodinia supercontinent differ widely. However,

the majority of reconstructions imply that Laurentia, Baltica, and Amazonia are closely assembled both before and during Rodinia (Li et al., 2008; Merdith et al., 2017). In addition, some models include Rio de la Plata (Gaucher et al., 2011) and the Kalahari Craton (Loewy et al., 2011; Dalziel et al., 2000; Jacobs et al., 2008b) as active collision counterparts to Laurentia. However, no consensus is made regarding the position of Kalahari within Rodinia (Moores, 1991; Dalziel et al., 2000; Fitzsimons, 2003; Pisarevsky et al., 2003; Jacobs et al., 2008b; Li et al., 2008; Merdith et al., 2017). In most reconstructions, e.g. in Li et al. (2008) and Merdith et al. (2017), the Kalahari Craton is placed along the (present–day) southern margin of Laurentia by the end of Mesoproterozoic, while other workers have suggested a more distant position of the Kalahari Craton in relation to Laurentia (Hanson et al., 2004). Several indications argue for a Kalahari Craton–Laurentia connection when combining paleomagnetic and geochronological data.

Paleomagnetic data from the ~1100 Ma Umkondo large igneous province (LIP) within the Kalahari Craton reveals two polarities, where the older emplacements have normal polarity, while the younger are reversed (Swanson-Hysell et al., 2015). The younger emplacements correspond with the reversed polarity of the Keweenawan Midcontinental Rift of Laurentia and support the Kalahari Craton to be conjoined with Laurentia in Rodinia. Subsequently, after the LIPs–event, the Namaqua–Natal Belt experienced high–grade metamorphism interpreted to be caused by a continent–continent collision with Laurentia (Jacobs et al., 2008b).

The Coats Land block (present–day East Antarctica) is inferred as a former Laurentia affinity, which was detached when the Kalahari Craton and Laurentia were separated (Loewy et al., 2011). The Coats Land block remained a part of the Maud Belt until the breakup of Gondwana (Pan–African times) and is today a remote part of East Antarctica. Compilation of paleomagnetic, geochronological, and Pb isotopic data imply that the Coats Land block was a piece of Laurentia at ca. 1100 Ma, which was separated from Kalahari at this time (Hanson et al., 2004; Loewy et al., 2011). Around ca. 1050 Ma Laurentia collided with the Kalahari Craton and the Coats Land block was sutured to the Maud Belt. Loewy et al. (2011) considered the Namaqua–Natal Belt and Maud Belt as an extension of the Grenville Orogeny as a consequence of the Kalahari–Laurentia collision.

Controversially, other workers suggest Rodinia models where the Kalahari Craton is placed adjacent to Western Australia (Fitzsimons, 2003; Pisarevsky et al., 2003). This correlation is

based on paleomagnetic data and similar age spectra from a sparse geochronological–data set. Ksienzyk and Jacobs (2015) compared detrital zircon ages from metasedimentary rocks detected in the Maud Belt and the Northampton Complex (western Australia) to test if they originated from the same sedimentary sequence. Their result revealed significantly different detrital age spectrums and argued for the Western Australia–Kalahari connection to be unlikely.

Figure 2.4 illustrates one possible position of the Kalahari Craton during the assembly of Rodinia.

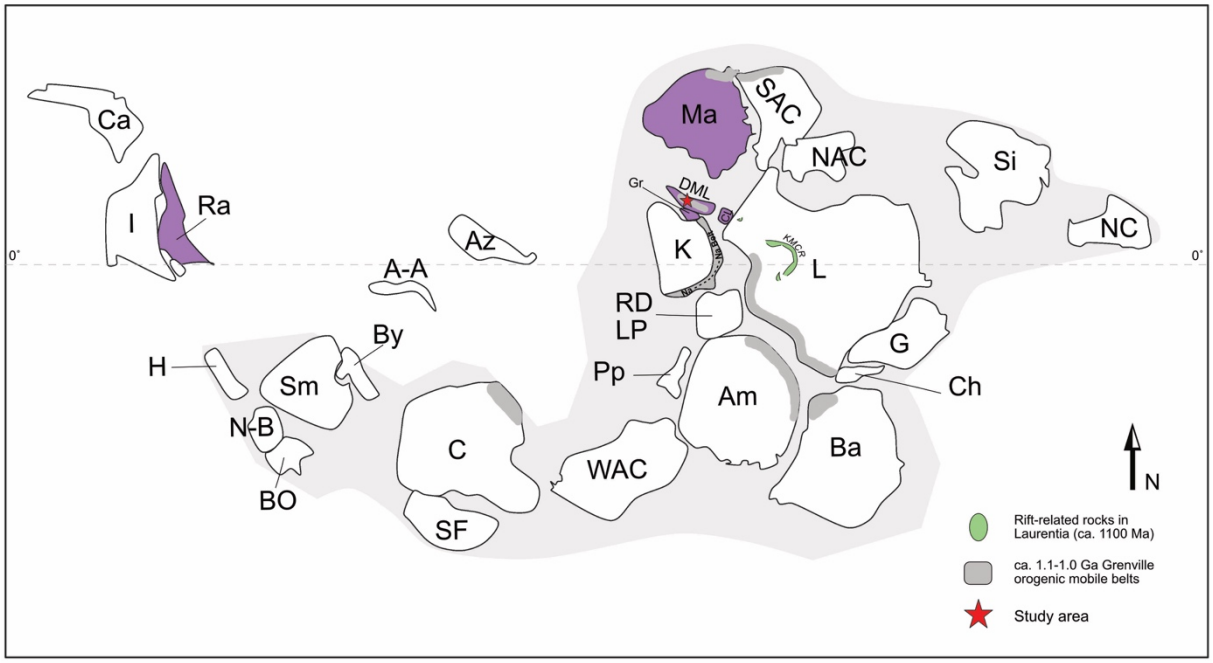

Figure 2.4: One possible Rodinia configuration at ca. 1000 Ma, modified after Merdith et al. (2017). The Kalahari Craton is juxtaposed to Laurentia. Purple–colored cratonic blocks represent parts of present–day Antarctica. The light grey shaded area is indicating the extent of Rodinia. The dark grey color marked on the cratonic blocks indicates Grenville orogenic belts and their location is simplified after Li et al. (2008). The position of the Coats Land block is based on the work of Loewy et al. (2011), indicating that the crustal entity stems from Laurentia. The location of the KMCR is based on Dalziel et al. (2000). Abbreviations: Ca – Cathaysia (South China), I – India, Ra – Rayner (Antarctica), H – Hoggar, N–B –Nigeria–Benin, BO – Borborema, Sm – Sahara Metacraton, By – Bayuda, A–A – Afif–Abas Terrane, Az – Azania, C – Congo, SF – São Francisco, WAC – West African Craton, Ma – Mawson, SAC – South Australian Craton, NAC – North Australian Craton, DML – Dronning Maud Land, Gr – Grunehogna Craton, K – Kalahari, Na–Na – Namaqua–Natal Belt, CL – Coats Land block, L – Laurentia, G – Greenland, RDLP – Rio de la Plata, Pp – Paranapanema, Am – Amazonia, Ba – Baltica, Ch – Chortis, Si – Siberia, NC – North China, KMCR – Keweenawan Mid continental rift system.

2.4 Break–up of Rodinia and the following formation of supercontinent Gondwana

2.4.1 Formation of the Tonian Oceanic Arc Super Terrane (TOAST)

During the Tonian period, extensive juvenile oceanic arcs with remnants from the Mozambique Ocean started to generate outboard of the Kalahari Craton, called the Tonian Oceanic Arc Super Terrane (TOAST) (Jacobs et al., 2015) (Fig. 2.5). Now, the oceanic arc terranes terminate at the Forster Magnetic Anomaly suture zone in the west (the margin of eastern Kalahari Craton) and stretches further into the SW–Terrane of the Sør Rondane Mountains, which represent the eastern part of Dronning Maud Land. U–Pb zircon analyses from samples of the TOAST show crystallization ages between ca. 1000–900 Ma, later affected by metamorphic overprinting in late Neoproterozoic–early Paleozoic accompanied by magmatic granitoids and migmatites (Jacobs et al., 2015).

During the Kalahari–Laurentia collision in Rodinia, the former active convergence along the eastern margin of Kalahari experienced a period of quiescence. As the breakup of Rodinia initiated (ca. 825–740 Ma) (Li et al., 2008), the passive margin of eastern Kalahari converted to an active margin with renewed subduction underneath Kalahari (Jacobs et al., 2020) (Fig. 2.5). Granitoids detected from the Schirmacher Oasis are dated ca. 785–760 Ma, and is interpreted to be a result of the active continental margin (Jacobs et al., 2020). Their geochemistry suggests that they evolved in the transition from a continental–margin arc setting to a back–arc setting caused by steeping subduction. Ultra–high–T (UHT) metamorphism and isobaric cooling retrogression are detected from granulites and gneisses within the Schirmacher Hills. The timing of the UHT metamorphism is dated to ca. 650 Ma (Baba et al., 2010). Baba et al. (2010) suggest the UHT metamorphism to be a result of a subduction roll–back setting accompanied by asthenosphere mantle upwelling, causing a back–arc extensional setting in the region around 650–600 Ma. Anorthosite and charnockite intrusions with ages of ca. 600 Ma, are detected within the Orvin–Wohlthat mountains, located south of the Schirmacher Oasis (Jacobs et al., 1998). These syn–tectonic intrusions were possibly emplaced by the upwelling asthenosphere mantle (Jacobs et al., 2020). The late Tonian active margin of eastern Kalahari led to convergence of the Mozambique Ocean and the TOAST converged towards the Kalahari Craton and became an integral part of the Craton as it collided with the margin of the Maud Belt (Fig. 2.5). U–Pb zircon metamorphic ages recorded from the TOAST area indicates long–term metamorphism between ca. 630–500 Ma (Jacobs et al., 2015). The late Neoproterozoic–

early Paleozoic metamorphic overprinting show a younging trend from west to east. Jacobs et al. (2015) interpreted the trend to reflect the collision pattern. The TOAST probably collided first with eastern Kalahari and subsequently with Indo–Antarctica (east Gondwana) during the final amalgamation of Gondwana. In addition, post–orogenic A–type granitoids dated between ca. 530–485 Ma, which are extensive within central Dronning Maud Land (Jacobs et al., 2003a; Jacobs et al., 2008a), are also found in the TOAST domain (Jacobs et al., 2015).

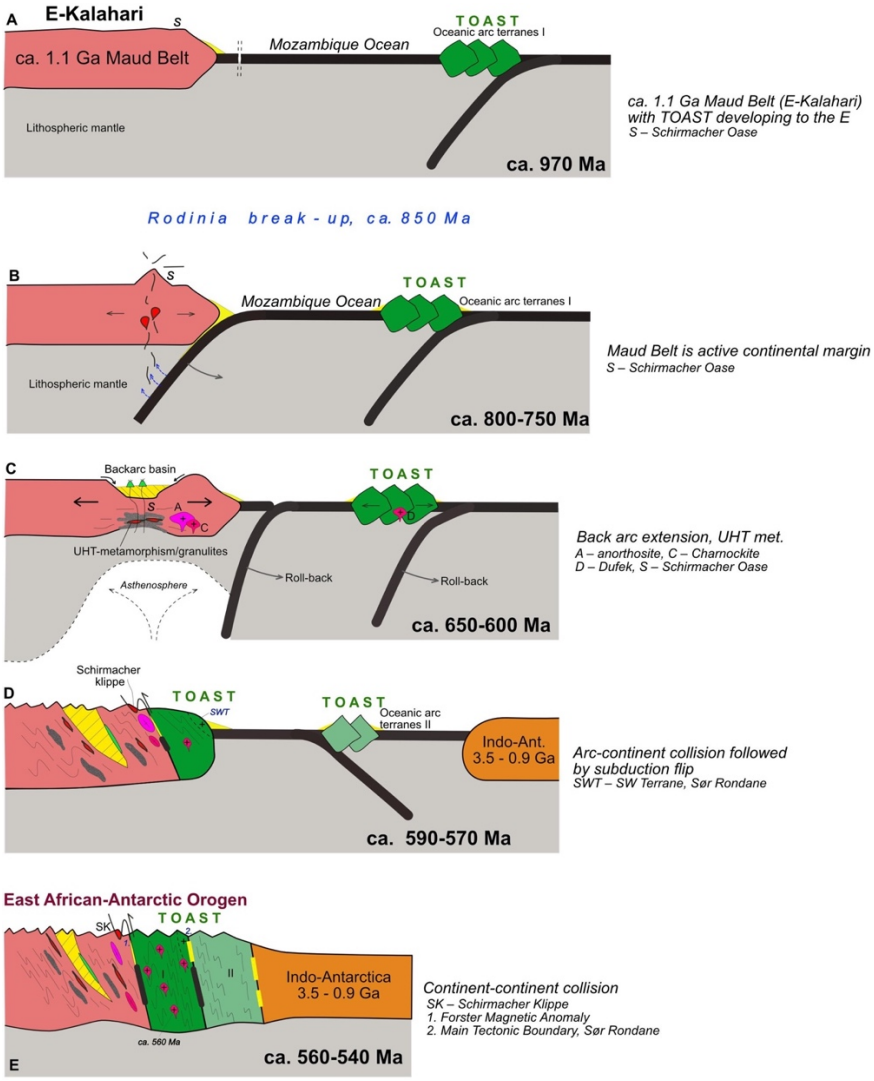

Figure 2.5: Cartoon illustrating the evolution of the Tonian Oceanic Arc Super Terrane from Tonian times until Pan–African times. (A) In Tonian the TOAST is evolving in the Mozambique Ocean. (B) During the breakup of Rodinia, the eastern margin of Kalahari is turning into an active continental margin. Granitoids are emplaced within the Schirmacher Oasis area as a result of subduction activity. (C) A subduction roll–back setting leads to an upwelling of the asthenosphere, which creates a back–arc extensional setting and UHT metamorphism at the eastern margin of Kalahari. (D) The TOAST collides with the western margin of Kalahari and is attached to the Maud Belt. The Schirmacher Klippe escapes much of the deformation. (E) In late Neoproterozoic–early Paleozoic the western Gondwana and eastern Gondwana collides to form the extensive East African–Antarctic Orogen. Post–tectonic A–type granitoids are emplaced. Figure from Jacobs et al. (2020).

2.5 The Pan–African orogenic event

2.5.1 The East African–Antarctic Orogen

The supercontinent Gondwana is formed by the assembly of different parts of West Gondwana and East Gondwana at ca. 650–500 Ma (Stern, 1994). West Gondwana represents the suture of South America, Amazonia Craton, and Africa, while East Gondwana has a more complex amalgamation history comprising of Proto–India, Madagascar, Sri Lanka, Seychelles and significant parts of East Antarctica and Australia (Grunow et al., 1996; Meert, 2003).
The collision of West and East Gondwana led to a closure of the Mozambique Ocean which resulted in an extensive ~ 8000 km orogeny, the East African–Antarctic Orogen (EAAO) (~550 Ma) (Jacobs and Thomas, 2004) (Fig. 2.6). The EAAO formed in a N–S–direction and stretches from the Arabian–Nubian Shield, characterized by gentle accretion processes in the north, to the Mozambique Belt, affected by continent–continent collision, in the south (Stern, 1994; Jacobs et al., 1998). The type of orogen is recognized as a Tibetan–style collision with crustal thickening in the south. The orogen is affected by oblique collision based on reported NW–SE–directed strike–slip faults (Berhe, 1990).

In the southern part of the EAAO, exposed nunataks within the DML region reveal late Neoproterozoic–early Paleozoic rocks with geological and structural orogenic information. In western Dronning Maud Land the Heimefrontfjella, Kirwanveggen and Sverdrupfjella indicate the western orogenic front of the EAAO. The boundary is exposed as the Heimefront Shear Zone, between the Vardeklattene and Sivorg Terrane, where typical unaffected Grenville–age rocks to the west are separated from the Mesoproterozoic crust with Pan–African overprint (~500 Ma) to the east (Golynsky and Jacobs, 2001; Jacobs and Thomas, 2002). The Pan–African overprinting increase eastwards from the Heimefront Shear Zone (Jacobs et al., 1998). According to Jacobs and Thomas (2004) the Heimefront transpression zone is interpreted as a major dextral transpression zone, whereas the EAAO represents a sinistral transpression setting. The southern termination of the orogen comprises of extruded blocks and a crustal entity (Coats Land block) representing older crust, where all are devoid from Pan–African metamorphic overprints (Fig. 2.6). This argues for a south–directed escape. Jacobs and Thomas (2004) suggest a Himalayan–type lateral–escape tectonics model to represent the late tectonic history of the southern part of East African–Antarctic Orogen.

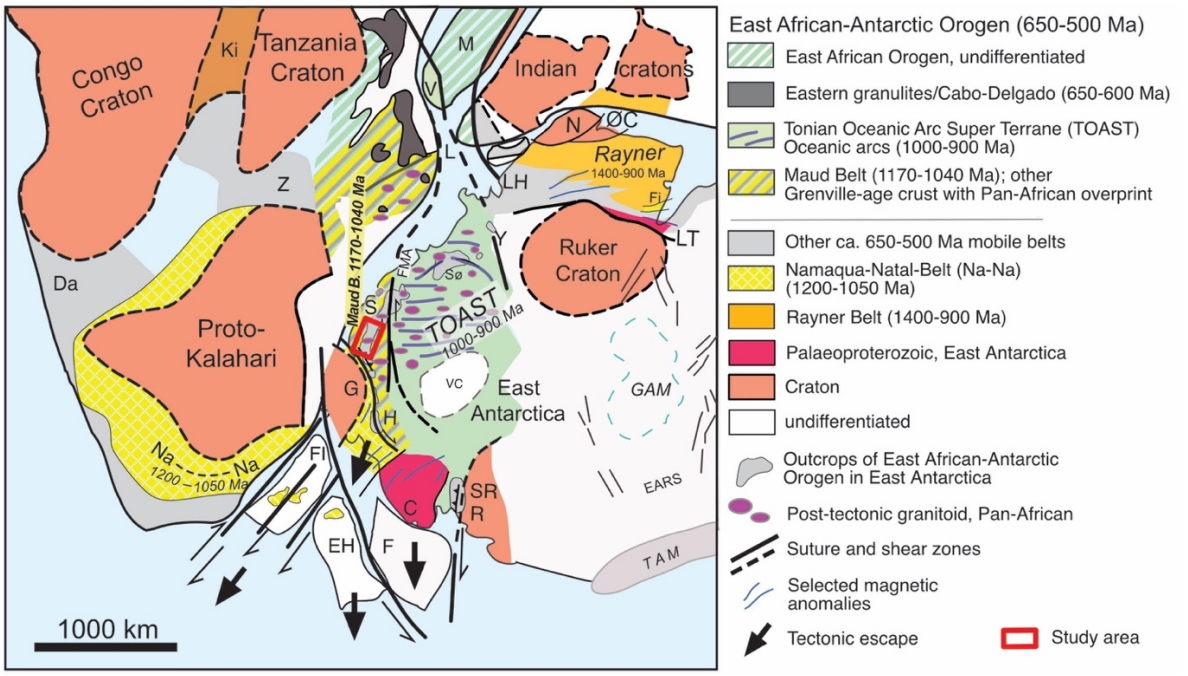

Figure 2.6: Reconstruction of Gondwana resulting in the extensive East African–Antarctic Orogen. The study area is marked by a red square. The southern terminal of the orogen show extruded blocks which lacks Pan–African overprint, probably as a result of a south–directed escape. Post–tectonic granitoids are detected within the Maud Belt and further north into the Mozambique Belt. Abbreviations: Ki – Kibran, V – Vohibori, M – Madagascar, Z – Zambesi belt, LH – Lützow–Holm, N – Napier Complex, ØC – Øygarden Complex, Da – Damara belt, L – Lurio Belt, Fi – Fisher Terrane, S – Schirmacher Oasis, Sø – Sør Rondane, FMA – Foster Magnetic Anomaly, LT – Lambert Terrane, Na–Na – Namaqua–Natal Belt, G – Grunehogna Craton, H – Heimefrontfjella, VC – Valkyrie Craton, cryptic, GAM – Gamburtsev, FI – Falkland Islands, EH – Ellsworth–Haag, F – Filchner block, C – Coats Land, R – Read Block, SR – Shackleton Range, TAM – Transantarctic Mts. Modified from Jacobs and Thomas (2004) and Jacobs et al. (2015).

2.5.2 The northern and southern part of the EAAO

In Gondwana reconstructions, the EAAO extends from the Arabian–Nubian Shield (ANS) to the northern section to the Mozambique Belt in the south (Stern, 1994; Jacobs and Thomas, 2002; Merdith et al., 2017). The Arabian–Nubian Shield shows strong evidence for a Wilson orogenic cycle as the shield is dominated by lithologies suggesting passive margin rift–related processes, Neoproterozoic juvenile island arcs formed in the Mozambique Ocean, deposits from volcano–sedimentary rocks and old ophiolites (Stern, 1994). The succession of the area is recognized by mild accretion at medium metamorphic grade (lower amphibolite facies) (Stern, 1994; Stern et al., 2004). In contrast, the southern extension of the EAAO, the Mozambique Belt is characterized continent–continent collision where pervasive highly reworked rocks underwent polyphase deformation up to granulite facies during the Pan–African event. The reworked rocks have Mesoproterozoic protolith ages but are sparse in evidence related to juvenile Neoproterozoic island–arc accretions (Stern, 1994; Muhongo and Lenoir, 1994; Jacobs et al., 1998; Jacobs and Thomas, 2004).

The southern continuation of the Mozambique Belt has earlier been up for discussion. Stern (1994) suggested the continuation to be situated southeastwards into Antarctica, while later research, carried out from geochronological and petrological information of rocks from East Antarctica, provides actual evidence for the orogen to extend into Antarctica (Shiraishi et al., 1994; Jacobs et al., 1998; Jacobs and Thomas, 2002; Jacobs et al., 2008a). In the reconstructions of Gondwana, Sri Lanka (part of the Mozambique Belt) is positioned close to Dronning Maud Land (Kriegsman, 1995). Shiraishi et al. (1994) correlated rocks from the Lützow–Holm Bay region (DML) with rocks from Sri Lanka and their result revealed both geochronological and lithological relations. The high–grade rocks yield late Pan–African ages and support the interpretation of the Mozambique Belt to extend into Dronning Maud Land within Gondwana. The interpretation is further supported by recorded relations between late Neoproterozoic–early Paleozoic metamorphic overprints, as well as anorthosites and A_2–type granitoids of late to post–tectonic Pan–African ages, found in both central DML and further north in the Lurio Belt in northern Mozambique (Fig. 2.6) (Jacobs et al., 1998; Jacobs et al., 2003a; Engvik et al., 2007; Jacobs et al., 2008a).

2.6 Post–Pan–African event

2.6.1 Evidences for orogenic collapse

During the period from ca. 530–485 Ma, the southern part of EAAO experienced lateral extension and intrusions of late–tectonic igneous rocks (Engvik and Elvevold, 2004; Jacobs et al., 2008a). The late–tectonic magmatic province is prominent in central DRonnning Maud Land and decreases northwards to the Nampula Complex, where it terminates at the Lurio Belt, NE Mozambique. Within central Dronning Maud Land the magmatism terminates at the western front of the EAAO. In total, the magmatic province covers an area of around 15 000 km^2 (Jacobs et al., 2008a). The area is characterized by voluminous A_2–type granitoids probably crystallized at mid–crust levels (Roland, 2002; Jacobs et al., 2003a; Jacobs et al., 2008a), which according to Jacobs et al. (2003a) is a consequence of delamination of the lithospheric root during orogenic collapse and subsequent extension (Fig. 2.7). The delamination of the mantle lithosphere is further supported by the evidence of partial melting, provoked by high temperature and rapid exhumation found in e.g. Mühlig–Hofmannfjella and Filchnerfjella, central Dronning Maud Land (Engvik and Elvevold, 2004). In addition to A_2–

type granitoids and evidence for near–isothermal decompression, indications of an orogenic collapse are reported by extensional structures located in central Dronning Maud Land (Jacobs et al., 2003d). In the work of Jacobs et al. (2008a) a major extensional structure was dated and compared with the ages detected from granitoids within the magmatic province and confirmed the ages to be concurrent. The overall findings support the late–post tectonic history of the Pan–African Orogen in the south to be affected by orogenic collapse.

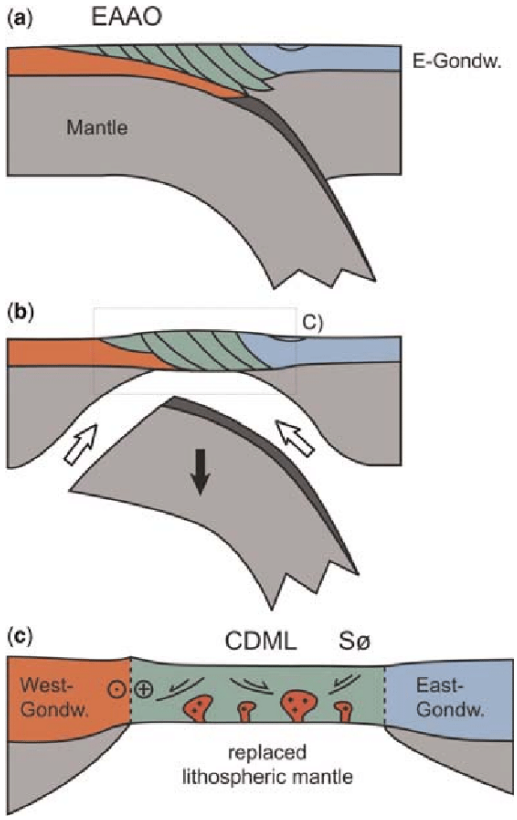

Figure 2.7: A cartoon depicting the delamination of the mantle lithosphere (orogenic root) during the orogenic collapse. Subsequent extension was caused by decompression and uplift, which led to partial melting and emplacement of voluminous granitoids within central Dronning Maud Land. From Jacobs et al. (2008a).

2.7 Summary of the regional geology in west, central, and east Dronning Maud Land

2.7.1 Western and central Dronning Maud Land

Western Dronning Maud Land comprises of the Grunehogna Craton (~3.0 Ga) (Groenewald et al., 1995; Marschall et al., 2010), in the north, with the Maud Belt juxtaposed to the Archean Craton. The south–western part is represented by the Heimefrontfjella, which is subdivided into three discontinuity–bounded Mesoproterozoic terranes; Kottas, Sivorg, and Vardeklettane

(Jacobs et al., 1996). As previously addressed, the Heimefront Shear Zone is located between the Vardeklettane Terrane (west) and Sivorg Terrane (east), caused by an oblique collision at ca. 1080 (Jacobs et al., 1993; Jacobs and Thomas, 1994). During Pan–African times, the Heimefront Shear Zone is interpreted as the western orogenic front of the East African–Antarctic Orogen (Jacobs et al., 1999). The basement rock of the terranes show Grenville–ages between ca. 1170–1030 Ma, which later has been overlain by sediments originated from Perm–Carboniferous time and by Jurassic basaltic rocks (Arndt et al., 1991; Jacobs et al., 1999; Jacobs et al., 1996; Bauer et al., 2003b; Jacobs et al., 2003c; Jacobs et al., 2009). The Vardeklettane Terrane is recognized by granulite facies rocks, mainly consisting of metaigneous rocks, typically charnockites (Jacobs et al., 1996). Both the Sivorg and Kottas Terrane comprises of amphibole-facies rocks. The former comprises of a bimodal metavolcanic sequence intruded by voluminous granitoids, whereas the latter consists of calk–alkaline granitoids and tonalites (Jacobs et al., 1996). Further north–east, exposed nunataks of the Kirwanveggen and H.U Sverdrupfjella represents the remaining western part of Dronning Maud Land. The basement rocks are dominated by migmatitic gneisses, granitic intrusions, and orthogneisses (Jackson, 1999; Grantham et al., 1995). Their ages reveal similar Grenville–ages as the Heimefrontfjella, culminating at ca. 1100 Ma (Harris et al., 1995; Harris, 1999; Jackson, 1999). Ages between 994–986 Ma are found in Kirwanveggen (Jackson, 1999), an age group uncommon for the rest of the Maud Belt.

Central Dronning Maud Land consists of Gjelsvikfjella (west–central), Mühlig–Hofmannfjella, and the Orvin–Wohlthat Mountain (east–central). Similar geological components as for western Dronning Maud Land is also reported here, mainly composing of granitic gneisses of various mineral assemblage compositions. This part of the Maud Belt is distinguished from western Dronning Maud Land by the abundance of late Cambrian post–tectonic intrusions (Jacobs et al., 2008a). In contrast to the western part, the U–Pb zircon ages from central Dronning Maud Land show a slightly narrower range in Greenville–age ages compared to the west–southern nunataks. Most common protolith ages range between ca. 1170–1075 Ma (Jacobs et al., 1998; Jacobs et al., 2003b; Jacobs et al., 2003a; Paulsson and Austrheim, 2003; Board et al., 2005; Bisnath et al., 2006; Jacobs et al., 2008a; Grantham et al., 2011; Baba et al., 2015; Hokada et al., 2019; Wang et al., 2020).

Almost immediately after crust formation, the Maud Belt experienced high–grade Greenville–age metamorphism accompanied by granitic magmatism. This event is obtained from zircon

rim overgrowths and zircon core ages from intrusions between 1090–1030 Ma found throughout the Maud Belt (Jacobs et al., 1998; Jackson, 1999; Jacobs et al., 2003c; Paulsson and Austrheim, 2003; Board et al., 2005). Previously, this event was explained by the Maud arc being an island arc system which accreted onto the Proto–Kalahari Craton (Bauer et al., 2003b). Recent studies however suggest that this event was partly caused by an advancing setting of the inboard subduction under the Proto–Kalahari Craton (Wang et al., 2020).

After the Mesoproterozoic high–grade metamorphic event, there is little evidence of tectonic activity between 1030 Ma and 650 Ma before the late Neoproterozoic–early Paleozoic collisional event occurred. The only exception is the Schirmacher Oasis region, located north of the Orvin–Wohlthat Mountains, where late Tonian granitoid intrusions of ca. 807 Ma and 785–760 Ma have been reported (Baba et al., 2010; Jacobs et al., 2020). The area was subsequently influenced by UHT metamorphism at ca. 640–600 Ma, generated by back–arc extension related to subduction slab–roll back (Baba et al., 2010). The metamorphic timing is in contrast to the southern Orvin–Wohlthat Mountains and the remaining Maud Belt, which lacks this metamorphic age component. The first evidence of late Neoproterozoic–early Paleozoic collisional history within the Maud Belt is associated with ca. 600 anorthosite and charnockite intrusions within the Orvin–Wohlthat Mountains (Jacobs et al., 1998). Subsequently, widespread medium–high grade metamorphism is bracketed from metamorphic zircon rims revealing two metamorphic pulses at ca. 580–550 Ma and 530–500 Ma (Jacobs et al., 1998; Bisnath and Frimmel, 2005). During this period, the Mesoproterozoic rocks were reworked due to the Pan–African collision of West and East Gondwana. The collision produced tight isocline, upright folds trending E–W and ESE–WNW. In addition, a major sinistral shear zone at the southern margin of Orvinfjella and transpressive structures in Wohlthatmassivet were formed during the collision (Bauer et al., 2003c). Central Dronning Maud Land shows a stronger Pan–African thermal overprint than the western region, which decreases towards the Heimefront Shear Zone. The latter metamorphic pulse (~530–500 Ma) reached granulite conditions and is accompanied by widespread post–tectonic intrusions as a consequence of an orogenic collapse and south–directed crustal extrusion (Engvik and Elvevold, 2004; Jacobs and Thomas, 2004; Jacobs et al., 2008a). The orogenic collapse resulted in near–isothermal decompression, which triggered partial melting of the Mesoproterozoic rocks as detected within Jutulsessen, Gjelsvikfjella (Paulsson and Austrheim, 2003). In addition, younger post–tectonic intrusions such as Stabben syenite (500±8 Ma) and aplitic dykes (~500 Ma) intruded after the migmatization event, as they are neither deformed nor migmatitic (Paulsson and Austrheim,

2003). A similar geological setting as suggested for Jutulsessen is recorded both west and east of the area. The post–tectonic intrusions form an extensive magmatic suite that mainly consists of charnockites and A_2–type granitoids (Jacobs et al., 2003a). They are largely confined within central Dronning Maud Land and decreases gradually in volume westwards. No post–tectonic magmatism has been detected east of H.U. Sverdrupfjella. The latest post–orogenic intrusion reported stems from a granitic intrusion (~480 Ma) in H. U Sverdrupfjella (Board et al., 2005). A summary of the regional evolution of west and central Dronning Maud Land is presented in following table (2.1).

Table 2.1: Summary of the typical lithology and the main tectono-thermal evolution of the Maud Belt (western and central Dronning Maud Land).

	Heimefrontfjella (Arndt et al., 1991; Jacobs et al., 1996)	**Kirwanveggen** (Harris, 1999)	**H.U. Sverdrupfjella** (Board et al., 2005)	**Gjelsvik–Mühligfjella** (Paulsson and Austrheim, 2003; Bisnath and Frimmel, 2005)	**Orvin–Wohlthat Mountains** (Jacobs et al., 1998)
Lithology	Bimodal metavolcanic rocks	Migmatitic gneisses Metacrystic orthogneisses	Migmatitic gneisses, granitic gneisses, orthogneisses	Migmatitic gneisses, granitic gneisses, amphibolites	Granitic orthogneisses, banded gneisses
Evolution	Volcanic arc magmatism (1190–1040 Ma)				
	M_1: First metamorphic event within the Maud Belt (peak ca. 1090–1030 Ma) reaching amphibolite – granulite–conditions				
	M_2: Second metamorphic event affecting the Maud Belt Pan–African collision (ca 550 Ma) 1. phase reaching amphibole–facies (590–530 Ma) 2. phase reaching granulite–facies (530–480 Ma) (Orogenic collapse) Pan–African intrusions ca. 510 Ma e.g. Stabben Retrograde metamorphism 500±8 Ma Migmatization Latest post–tectonic granite intrusion ca. 480 Ma				Anorthosite ca. 600 Ma
	Gondwana break–up (Jurassic times)				

2.7.2 Eastern Dronning Maud Land

The Foster Magmatic Anomaly (Riedel et al., 2013) marks the boundary between central and eastern Dronning Maud Land, and represents the previous margin of eastern Kalahari. The eastern part comprises of arc terranes which accreted onto the margin of central Dronning Maud Land, represented by the TOAST domain and the Sør Rondane Mountains. The geological evolution for this part of Dronning Maud Land is fundamentally different from the Maud arc in relation to their igneous activity and tectonic regime. The TOAST represents an extensive juvenile oceanic arc developing outside of Kalahari in the Mozambique Ocean (~990–900 Ma) (Jacobs et al., 2015). Geochronological and geochemical data reported from the TOAST show a strong correlation to the Southwest (SW) Terrane of Sør Rondane, suggesting that the terranes have formed from the same oceanic arc domain (Elburg et al., 2015; Jacobs et al., 2015). The Southwest (SW) Terrane, together with the Northeast (NE) Terrane, represents the Sør Rondane Mountains. A suture zone is separating the terranes, the Main Tectonic Boundary (MTB) (Osanai et al., 2013). The basement of the SW–Terrane is dominated by greenschist–facies to granulite–facies rocks, whereas amphibole–facies and granulite–facies rocks underlain the NE–Terrane. Detrital zircon ages from the NE–Terrane reveal Paleoproterozoic and Archean components (up to ~3.3 Ga), an age component missing within the SW–Terrane (Shiraishi et al., 2008; Osanai et al., 2013). Isotopic signatures from the older igneous history (~1000–975 Ma) of the SW–Terrane indicates a tonalitic signature formed in a juvenile oceanic setting. Younger magmatism (~960–920 Ma and 772 Ma) comprise of a calc–alkaline adiakites and may reflect a post–subduction scenario caused by a slab–break off (Kamei et al., 2013; Osanai et al., 2013; Elburg et al., 2015). The different provenance of detrital zircons and early metamorphic evolution emphasize a separate development before a contemporaneously high–grade metamorphic event at 650–600 Ma, indicating the timing of their collision (Osanai et al., 2013; Shiraishi et al., 2008). P–T–*t* investigations exhibit a counter–clockwise path for the SW–Terrane and a clockwise path for the NE–Terrane (Osanai et al., 2013). Contrasting PT–paths on either side of the MTB have led to the interpretation that the NE–Terrane probably thrusted over the SW–Terrane (Osanai et al., 2013). The final detected magmatic and metamorphic events range from ca. 580 to 500 Ma, related to the progressive amalgamation of the Gondwana (Elburg et al., 2016). No igneous ages younger than 500 Ma are recorded (Elburg et al., 2016), in contrast to central Dronning Maud Land where igneous ages of 490–480 Ma can be found (Jacobs et al., 2003a; Paulsson and Austrheim, 2003; Board et al., 2005).

3 Fundamentals of U–Pb zircon dating

3.1 U–Th–Pb system in zircons

Zircon ($ZrSiO_4$) is an orthosilicate mineral with a tetragonal crystal system and is often an abundant mineral in magmatic and metamorphic rocks. Within the mineral, isolated SiO_4 are connected with distorted ZrO_8 dodecahedra (Harley and Kelly, 2007). The ZrO_8 dodecahedra form zigzag–chains along the b–axis, whereas the edges that aligned along the c–axis are shared with alternating chains of ZrO_8 and SiO_4 polyhedra. The crystal structure is relatively open with voids and channels incorporated within the unoccupied space between the chains. In pure zircon crystals, the voids contain trace amounts of Rare Earth Elements: Y, P, Hf, Th, and U due to simple or coupled substitution mechanisms (Hoskin and Schaltegger, 2003). As a result of the overall structure, the zircon has a moderately high density of 4.66 gcm^{-3} and a hardness of 7.5 (Harley and Kelly, 2007). The zircon is a robust mineral, both chemical and mechanically, and has a high closure temperature (ca. > 900ºC) (Faure and Mensing, 2005). The robustness gives the zircon the ability to survive magmatic and metamorphic processes and reflect the mineral's geological history (Corfu et al., 2003). These characteristics make the zircon suitable for isotopic age determination. The high concentration of U, an average of 1350 ppm, within a zircon can be attributed to the substitution of U^{4+} (ionic radius 1.05 Å) for Zr^{4+} (0.87 Å), while the low initial ^{204}Pb (non–radiogenic) concentrations in zircon can be explained by Pb having a lower charge (2^+) and a lager ionic radius (1.32 Å), hence, excluding Pb from the crystal lattice (Faure and Mensing, 2005). Too high U content can cause radiation damage to the zircon. Damaged grains are called metamict zircons and are not ideal for age determination as they tend to lose radiogenic lead (Corfu et al., 2003). Metamict domains can be recognized by analysing the zircon morphology with a scanning electron microscope (SEM).

The zircon's ability to incorporate U and exclude Pb from the crystal lattice enhance its suitability as a geochronometer. At the time of formation, the zircon will contain little to no Pb, which means that the Pb measured will be a result of U decay.

The U–Th–Pb system separates into three independent decay series where ^{238}U and ^{235}U transform into their stable daughter products ^{206}Pb and ^{207}Pb, respectively, whereas ^{232}Th decays into Pb^{208} (Schoene, 2014). The half–life of these three series varies: $^{238}U \rightarrow {}^{206}Pb$ = half–life of 4.5 Ga, $^{235}U \rightarrow {}^{207}Pb$ = half–life of 0.7 Ga, and $^{232}Th \rightarrow {}^{208}Pb$ = half–life of 14 Ga (Schoene, 2014). The strength of this system is the two individual decay series of U–Pb used for age determination. The interesting feature of these isotopic systems is that both parents and

daughters have identical chemical behavior and the same diffusion rate, but each has an individual radiometric system (Cherniak and Watson, 2003). Thus, two individual radiometric ages can be calculated by measuring the Pb/U content for both isotopic system within the zircon (equation 1&2). Furthermore, the $^{207}Pb/^{206}Pb$ age is possible to calculate with the known modern ratio of $^{238}U/^{235}U = 137.818$ (equation 3) (Hiess et al., 2012).

1. $^{207}Pb = {}^{235}U\ (e^{\lambda 235t} - 1)$

2. $^{206}Pb = {}^{238}U\ (e^{\lambda 238t} - 1)$

3. $$\frac{^{207}Pb}{^{206}Pb} = \frac{(e^{\lambda 235t} - 1)}{137.818(e^{\lambda 238t} - 1)}$$

3.1.1 Concordia ages

A graphical representation of U–Pb ages was first carried out by Ahrens (1955) and further developed by Wetherill (1956). The Wetherill Concordia diagram is based on plotting calculations from the two individual decay schemes of U ($^{206}Pb/^{238}U$ versus $^{207}Pb/^{235}U$) against each other. A reference curve, the concordia line, will represent the difference in ratios based on the two systems over time. If the system has remained undisturbed since the time of crystallization, the values for time will plot on the concordia line. This indicates that both systems yield equivalent ages, such ages are called concordia ages. The time value represents a concordant age, implicating the crystallization age of the zircon (White, 2015).

3.1.2 Discordia ages

The concordia diagram can also provide age determinations from a system that has not remained entirely closed. Ratios that plot outside the concordia line indicate a disagreement between the $^{206}Pb/^{238}U$ and $^{207}Pb/^{235}U$ ages, called discordia ages (Harley and Kelly, 2007). Discordia ages can indicate an open–system behavior of the zircon allowing fluctuation of isotopes in and out of the system. In a concordia diagram, the upper interception between the concordia and discordia corresponds to the crystallization age of the zircon, while the lower intersections are commonly a result of a later thermal disturbance or mixing of zircon phases (Wetherill, 1956; Cherniak and Watson, 2001). The interpretation of the lower intersect implies that the zircon has experienced Pb–loss due to Pb being a more mobile element than U (Mezger and Krogstad, 1997). Pb–loss is most likely a consequence of alteration or thermal factors and

recrystallization. Such factors will reset the clock once the system is reclosed. As a result, the Pb depleted points will plot outside the concordia curve as discordia ages (Mezger and Krogstad, 1997; Harley and Kelly, 2007). Discordant age points can also appear due to the mixing of zircon phases (e.g. an older core and a younger rim). The diffusion of Pb in a zircon increases with the rate of increasing metamictization. Metamict zircons are more susceptible to alteration processes, which result in readily Pb–loss (Cherniak and Watson, 2001).

In a concordia diagram the radiogenic variants of Pb are plotted. In order to obtain the correct concordia and discordia ages the initial ^{204}Pb, ^{206}Pb, and ^{207}Pb composition, often referred to as common Pb, needs corrections. The measured amount of ^{204}Pb can be used to quantify ratios for $^{206}Pb/^{204}Pb$ and $^{207}Pb/^{204}Pb$ in a direct whole–rock analysis and estimate the initial composition of both ^{206}Pb and ^{207}Pb within the zircon and subtract the initial common Pb from the age–calculation (Dickin, 2018). In addition, common Pb can be subtracted with the help of known ratios of Pb–isotope based on a Pb evolution model (average crustal lead) (Stacey and Kramers, 1975; White, 2015).

3.1.3 Tera–Wasserburg concordia diagram

The Tera–Wasserburg concordia diagram is modified by Tera and Wasserburg (1972). In contrast to a Wetherill concordia diagram, the Tera–Wasserburg concordia diagram uses $^{238}U/^{206}Pb$ and $^{207}Pb/^{206}Pb$ on the x– and y– axis, respectively. In a Wetherill concordia diagram, the initial Pb is already subtracted prior to the calculations determining the plot–coordinates, whereas when plotting in a Tera–Wasserburg concordia diagram no initial Pb corrections are made and plots directly as measured (Wendt, 1984) (Fig. 3.1). When plotting the variable proportions of the radiogenic Pb and the common Pb projects a straight line intersecting the concordia curve at the true age, and on the $^{207}Pb/^{206}Pb$ (y–axis) axis, giving the initial composition of common $^{207}Pb/^{206}Pb$ at the time of crystallization. Discordant data will plot outside the line (Schoene, 2014). Advantages of using the Tera–Wasserburg concordia diagram over the Wetherill concordia diagram is: (1) the visual presentation of the concordia curve shows a stronger curvature making it easier to distinguish the residuals of the point measured from the concordia (e.g. when interpreting the discordant data as ancient Pb–loss or recent Pb–loss) and (2) much fewer error correlations, however, uses correlations due to common Pb corrections (Wendt, 1984; Ludwig, 2012). A disadvantage of the Tera–Wasserburg concordia diagram is the difficulty of showing data plots when the U/Pb ages are wide in range (e.g. a range of about 3000 Ma) (Ludwig, 2012).

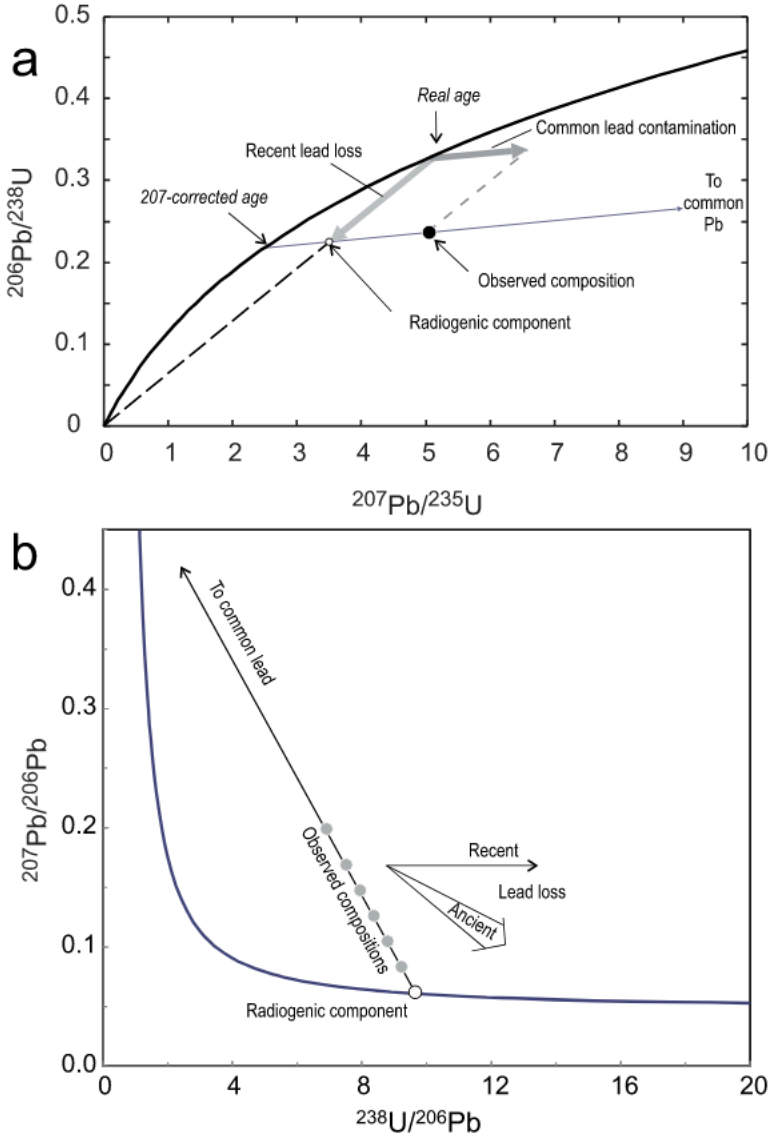

Figure 3.1: (a) Wetherill concordia diagram: The black line illustrates a concordia curve. A discordant point is plotted as a black dot in order to illustrate how common Pb corrections are necessary in order to get real age value. The discordant point with common Pb correction is illustrated as a white dot. (b) Tera–Wasserburg concordia diagram: The blue curved line represents the concordia line where both components ($^{207}Pb/^{206}Pb$ and $^{238}U/^{206}Pb$) yield equal ages to give concordant age(s). The initial $^{207}Pb/^{206}Pb$ ratio can be found where the illustrated line will intercept with the y–axis (to common lead). Discordant ages will plot outside the illustrated line with a horizontal line if the Pb–loss is recent or more vertical if the Pb–loss is ancient. Figure from Andersen et al. (2019).

3.2 Secondary Ion Mass Spectrometry (SIMS) geochronology

SIMS (secondary ion mass spectrometry) is an analytical technique suitable for minerals with complex thermal histories. The two ion microscope instruments used to perform a SIMS analysis are SHRIMP or Cameca IMS1270/1280. The advantage of using SIMS are high precision of measured ages (~1%), minimal damage to the samples, and good spatial resolution regarding depth profiling (Ireland and Williams, 2003; Kröner et al., 2014). SIMS combined with cathodoluminescence imaging or backscattered electron imaging make up a powerful tool that allows to investigate the geological history of both the core and rims of a single zircon grain by dating the different phases individually (Ireland and Williams, 2003).

SIMS is designed to perform an in–situ analysis based on the detection of secondary ions generated by a sputtering process. The sputtering process consists of a finely focused beam of light ions (e.g. O_2^+ or O_2^-) that are projected onto a polished Au–coated surface of the sample (Fig. 3.2) (Dickin, 2018). The light ion beams create an impact crater on the surface commonly focused to approximately 10–30 µm diameter wide and 5 µm depth (Ireland and Williams, 2003). The sputtering process provokes ionized ions (secondary ions) from the surface, which subsequently accelerates into a double–focused mass spectrometry. Within the mass spectrometry, the aim is to analyse the secondary ions and measuring the intensity of the ions using the function: $\frac{M}{Z}$ (mass per electric charge) in order to separate and detect the ions (Dickin, 2018; Mathieu and Leonard, 1998). Finally, the detector will measure the abundance of the ions.

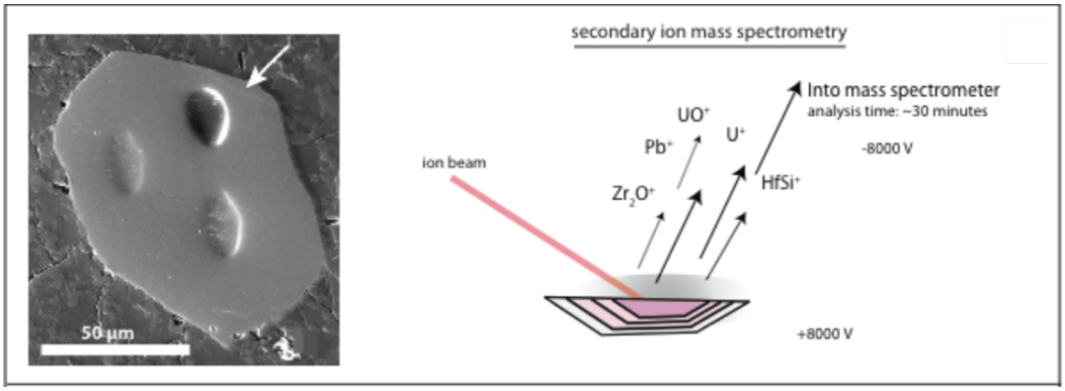

Figure 3.2: A cartoon illustrating the basics of SIMS analysis, where ion beams are projected onto the mineral surface. Figure from Schoene (2014).

A major challenge regarding the analytical data from SIMS is U/Pb fractionation. U/Pb fractionation can occur as a result of the elements changing their efficiencies and properties when becoming secondary ions during the sputtering process. The measured Pb^+/U^+ ratios (secondary ions) can vary up to 10% from their interelement ratios (Pb/U), which is critical for the geochronology analysis (Ireland, 2014). In order to correct for this, the Pb^+/U^+ must be calibrated to a standard. The standard is based on homogenous zircon grains with well–known compositions (Ireland, 2014). Compston et al. (1984) noticed a consistency between the Pb/U and OU^+/U^+ ratios. A correlation between Pb^+/U^+ and OU^+/U^+ could be used to reduce the analytical variability to better than 1% (Ireland, 2014). By using the standard (representing a calibration line), the measured OU^+/U^+ ratios of the unknown zircon can be plotted against the Pb^+/U^+ in order to correct for the Pb/U value and determine the age relative to the known standard age (Ireland and Williams, 2003).

4 Methodology

4.1 Samples

The samples reserved for this study are from the NARE geology 2017–2018 expedition to East Antarctica collected by Prof. J. Jacobs. Six samples (JT3, JT8, JT10, JT25, JT27, and JT35) were chosen for further investigation, involving zircon analysis and petrographic analysis. All samples were collected around Jutulsessen near the Norwegian Troll research station in central Dronning Maud Land. The following figure shows the sampling localities (Fig. 4.1). An overview of the samples is given in table 4.1 including lithology, location, and GPS–coordinates. The selected samples have been analysed at laborites at the University of Bergen and the Nordsim facility in Stockholm by using a range of analytical techniques to allow detailed geochronologic and petrographic information. All preparations and analyses were done under controlled conditions. The different analytical techniques used are described in the following section.

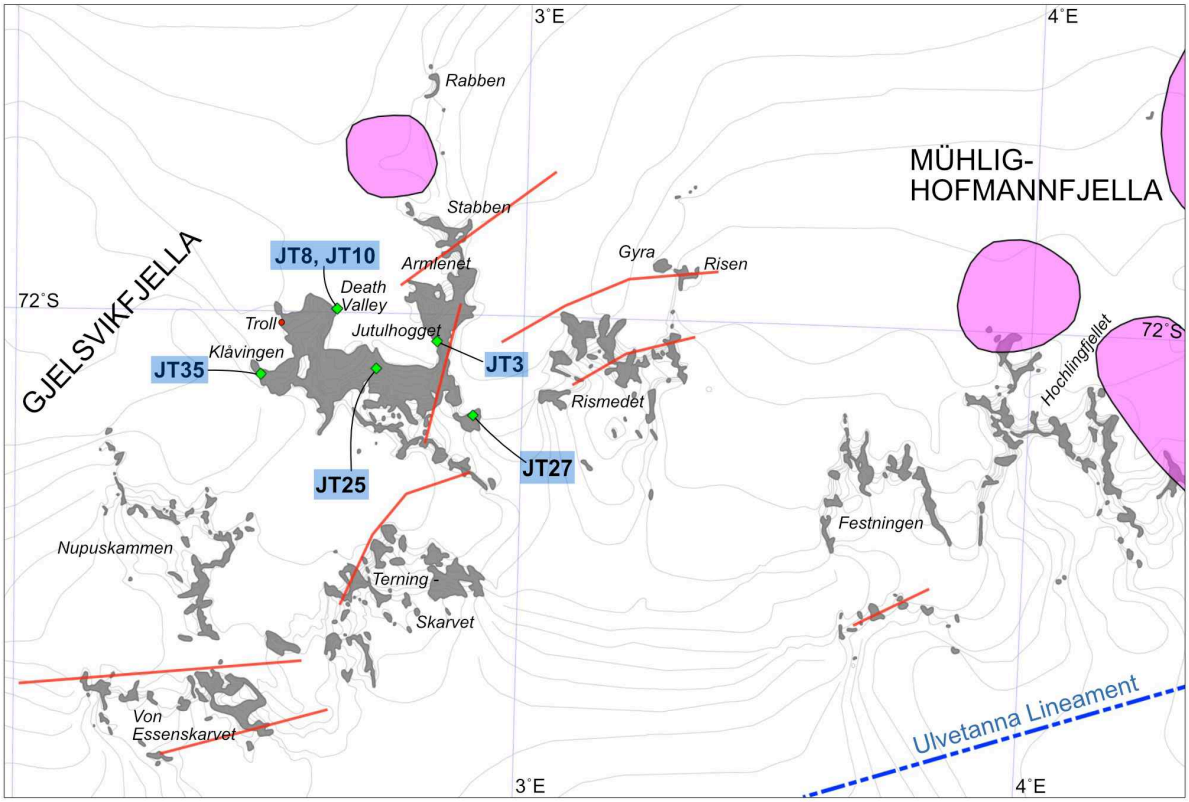

Figure 4.1: An overview of the sample locations (green squares) from Jutulsessen nunataks. The red circle illustrates the location of the research station, Troll. The purple–colored spots are representing Pan–African late–tectonic granitoids. The red lines are illustrating the main structural trend.

Table 4.1: Sample name, lithology, location, and GPS coordinates for all analysed samples.

Sample	**Lithology**	**Location**	**GPS–coordinates**
JT3	Granitic gneiss	Jutulhogget–W	72°0'59.22"S 2º49'42.276"E
JT8	Granulitic granodioritic gneiss	Death Valley	71º59'51.936"S 2º37'49.872"E
JT10	Granulitic granodioritic gneiss	Death Valley	71º59'51.936"S 2º37'49.872"E
JT25	Granitic granodioritic gneiss, migmatite	Sesseggen	72º2'1.32"S 2º42'35.172"E
JT27	Granitic gneiss	Jutulhogget–SE	72º3'39.6"S 2º54'8.676"E
JT35	Grey migmatite gneiss	Klåvingen	72º2'17.808"S 2º28'55.488"E

4.2 Sample preparations

4.2.1 Mineral separation

Both crushing and mineral separation was carried out at the University of Bergen. The six samples were first crushed into pebbles with sizes of ca. 3 cm by using a sledgehammer. Thereafter, the samples were pulverized into size finer than 315 μm with a Fritch Pulverisette 13 discmill (Fig. 4.2a). Larger particles were separated by using sieves. Sample material with grain size finer than 315 μm was separated with the help of a Holman–Wilfley shaking table, collecting the heavier fractions in a separate container from the lighter fractions (Fig. 4.2b). This procedure was done to reduce the sample size and to get sample material with a high concentration of heavier fractions for further processing. The heavy fraction was dried and followed by magnetic separation. The magnetic separation was conducted by a Franz Ferromagnetic Separator and was completed in three stages. The current of the Ferromagnetic Separator during the stages was set to 0.5 mA, 0.7 mA, and 1.0 mA, respectively. During all three stages, the forward and sideway tilt was applied to 15º. The magnetic separation procedure was done to remove weakly ferromagnetic minerals such as hematite from zircon and apatite.

Finally, the non–magnetic samples were further separated with the heavy liquid diiodomethane (DIM) with a density of 3.3 g/cm^3 (Fig. 4.2c). Both fresh and recovered DIM was used. The heavy liquid sodium heteropolytungstates was not necessary to conduct before the DIM due to the size of the samples after the magnetic separation. During the heavy liquid separation, the DIM separated zircons, with a density of 4.60–4.70 g/cm^3, from other heavy minerals with a lower density such as apatite (3.16–3.22 g/cm^3). The samples were rinsed subsequently with acetone to avoid the minerals clumping together. All the individual stages of sample preparations were done carefully to avoid contamination.

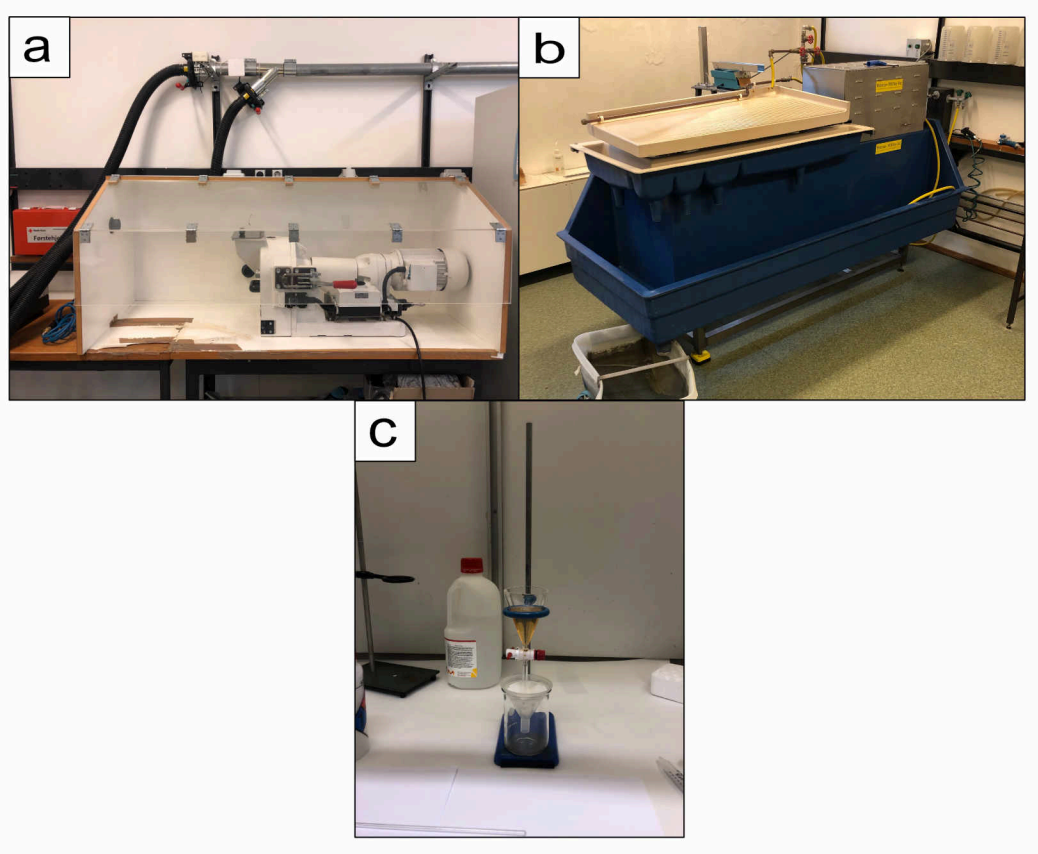

Figure 4.2: (a): Fritch Pulverisette 13 discmill. (b): Holman–Wilfley shaking table. (c): mineral separation examined by heavy liquid diiodomethane (DIM).

4.2.2 Mount preparations

All six samples were placed on the same mount. To prepare the mount, a tweezer was used to transfer the zircons directly onto a glass plate with double–sided tape. The process was done under a Zeiss Microscope with a cross–polarized light (Fig. 4.3a). On average, 50–60 grains were picked for each sample. Clearly metamict zircons were avoided. Finally, the mount was sent to the Nordsim facility in Stockholm for further preparations.

4.2.3 Cathodoluminescence imaging

After the preparations were examined at the Nordsim facility (Stockholm), a circular gold–coated mount was sent back for imaging at the University of Bergen. Firstly, both transmitted light and reflective light images were taken in order to reveal fractured and inclusion within the zircon grains. The images were photographed by an Olympus BX51 microscope.

The cathodoluminescence (CL) imaging was operated in the scanning electron microscope laboratory by a Zeiss Supra 55VP Scanning Electron Microscope (Fig. 4.3b). Before placing the mount within the microscope, the mount was coated with carbon and placed in a sample holder. Further, the mount was placed onto a stage in the microscope chamber, which was under a vacuum. The CL images provided detailed information about the zonation patterns within the grains. In combination with transmitted light– and reflective light images, it was possible to get a clearer overview of the zircons internal textures in order to select individual spots for analysis. On average, 20–30 spots were selected for dating analysis. The mount, together with the images, was sent back to the Nordsim facility in Stockholm to complete the SIMS analysis.

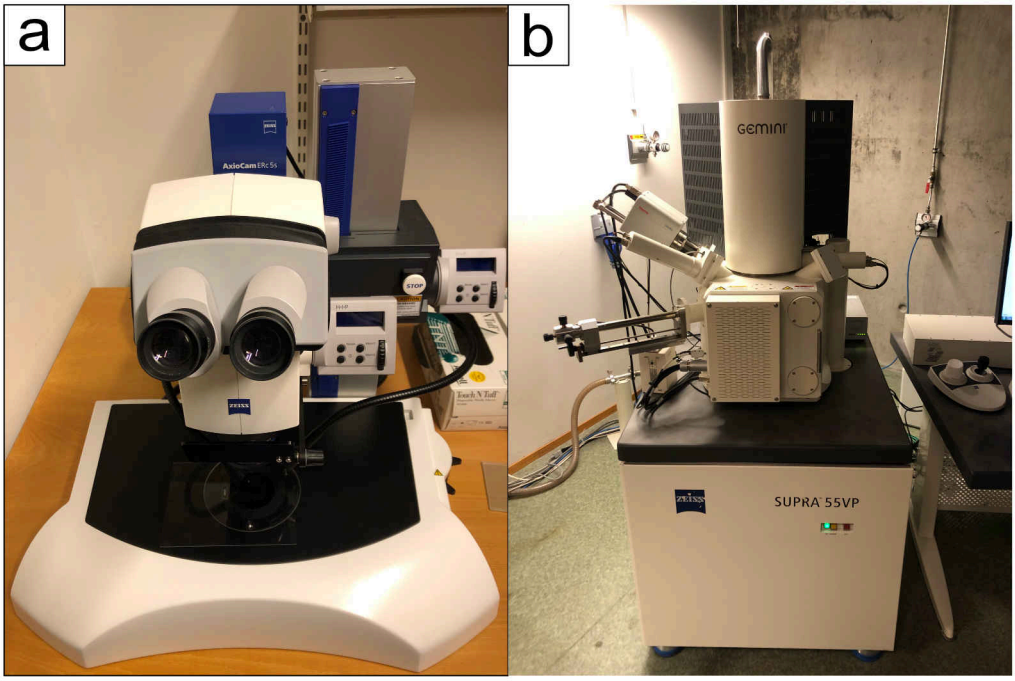

Figure 4.3: (a): a Zeiss Microscope with a cross–polarized light used to pick the zircons and place them on the mount. (b): the Zeiss Supra 55VP Scanning Electron Microscope was used to take both CL–imaging to find the locations for the spot analyses and for post–CL–imaging.

4.3 SIMS analysis

The Nordsim facility (Stockholm) operates a Cameca IMS1280 ion microprobe to perform a U–Th–Pb analyses of zircons (Fig. 4.4). The analytical methods follow the protocol outline of Whitehouse et al. (1999) and Whitehouse and Kamber (2005). The reported SIMS data can be found in the appendix.

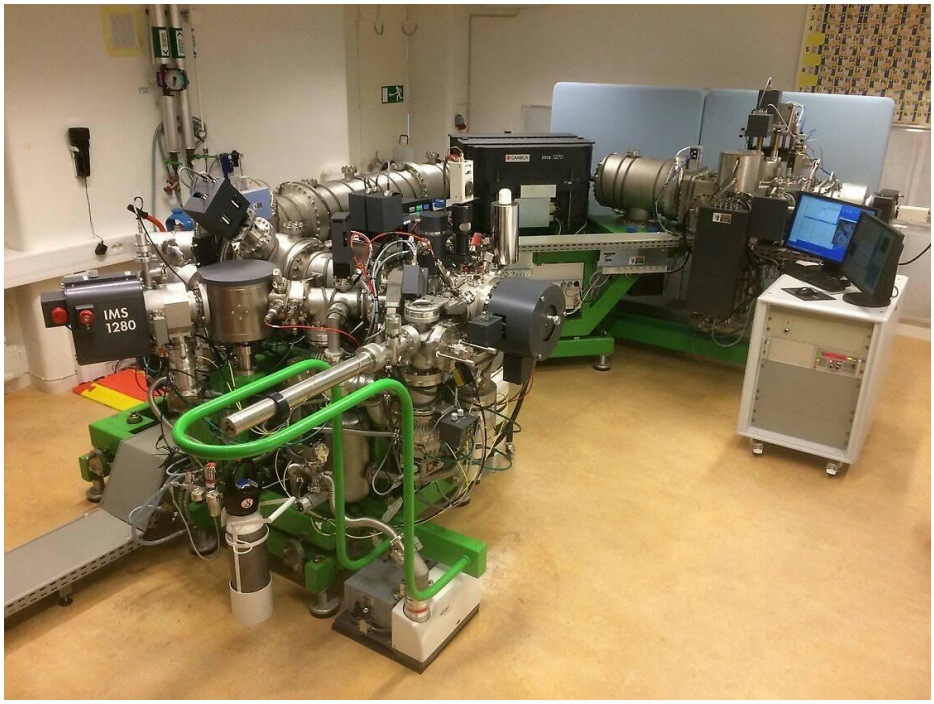

Figure 4.4: CAMECA IMS1280 ion microprobe used to generate U–Th–Pb analysis for the picked zircons. Nordsim facility in Stockholm. Photo: Cheng–Cheng Wang.

4.4 Data processing

Isoplot version 4.15 was used to calculate concordia and discordia ages, with guidance from the Isoplot manual from Ludwig (2012). For all samples, only the common ^{204}Pb–corrected ages were used for the datasets. Whenever possible, a common concordia age was calculated for the analyses using Isoplot. Alternatively, a weighted mean age was calculated for the concordant analyses given at the 95% confidence level. Concordia ages were plotted with the 1σ error ellipse, whereas the age uncertainties are plotted with a decay constant of 2σ. The mean square of weighted deviates (MSWD) for concordia ages are based on the combined concordance and equivalence (Ludwig, 1998). Some ages were calculated from an upper and lower intercept. The estimated composition of common Pb was corrected for by using the two–stage model by Stacey and Kramers (1975). The model is developed from estimations made by terrestrial Pb isotopes defining the composition of average crustal lead. In order to correct for the initial Pb, the calculation needs to contain the amount of ^{204}Pb measured within the analysis and the model by Stacey and Kramers (1975) for standards.

Some samples had analyses with large age errors. Analyses with more than 5% reverse discordance are considered as unreliable data and are thus excluded from any further calculations. Analyses with more than 10% reverse discordance are omitted from the concordia plots. These analyses are marked as grey in the appendix.

5 Results

5.1 Petrology

Figure 5.1 show selected filed photographs from different sample locations in Jutulsessen, Gjelsvikfjella.

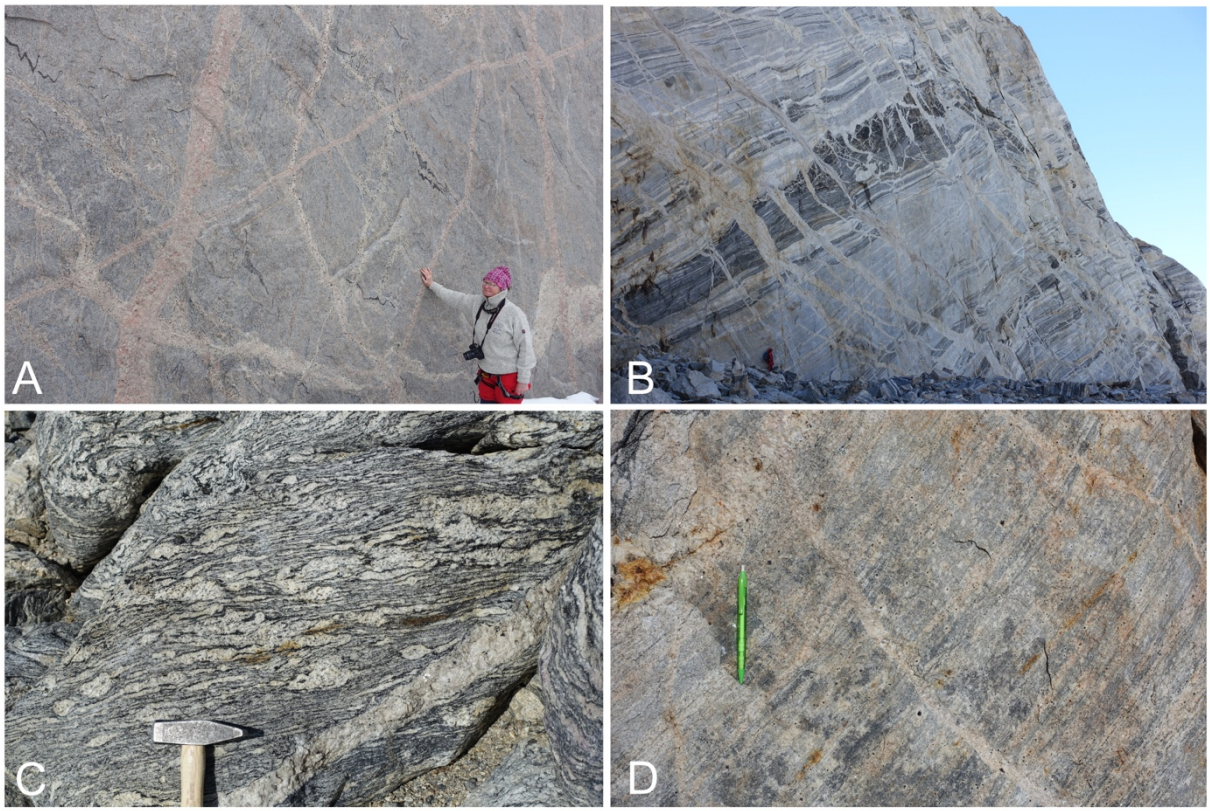

Figure 5.1: Field photographs from Jutulsessen at the sample localities. (A) Pink dikes cut the older felsic intrusions and basement rock at Jutulhogget, JT3. (B) A larger mafic sill intrusion is cutting the basement rock. Later Pan–African melt intrusions cuts the outcrop at Death Valley, JT8 and JT10. Scale: geologist at the left corner of the picture. (C) Migmatite gneiss with augen texture at Klåvingen, JT35. (D) Photograph of sample location of JT27, Jutulhogget–SE.

5.1.1 Sample JT3, granitic gneiss, Jutulhogget–W

The granitic gneiss is equigranular with phaneritic texture and randomly distributed minerals (Fig. 5.2A). The rock consists mainly of quartz, plagioclase, K–feldspar, and biotite. Zircon, apatite, titanite, opaques, rutile, and secondary muscovite are typical accessory minerals. The plagioclase minerals show distinctive albite polysynthetic twinning. Some plagioclase grains show antiperthite unmixing of K–feldspar. The K–feldspar show cross–hatched twinning indicating the feldspar to be microcline. A few microclines have perthitic texture, often concentrated in the center of the mineral (Fig. 5.2C). The occurrence of perthitic and

antiperthitic unmixing gives indications of high–temperature feldspar (Barker, 2013). Myrmekitic texture is present in quartz and can be commonly be observed at the boundary towards plagioclase. Titanites are only found in contact with biotite, and it is often in reaction with an opaque mineral. The thin section reveals a granoblastic texture, typical of metamorphic rocks. Quartz show polygonal to bulged grain boundaries, and undolose extinction are common. Plagioclase and microcline show moderate sericitization. Sericite is an alternation mineral related to hydrothermal processes (Barker, 2013). Several biotite grains have been retrogressed to chlorite or partly chloritized. Some biotite minerals are partly replaced by a symplectic intergrowth of quartz at the edges (Fig. 5.2B).

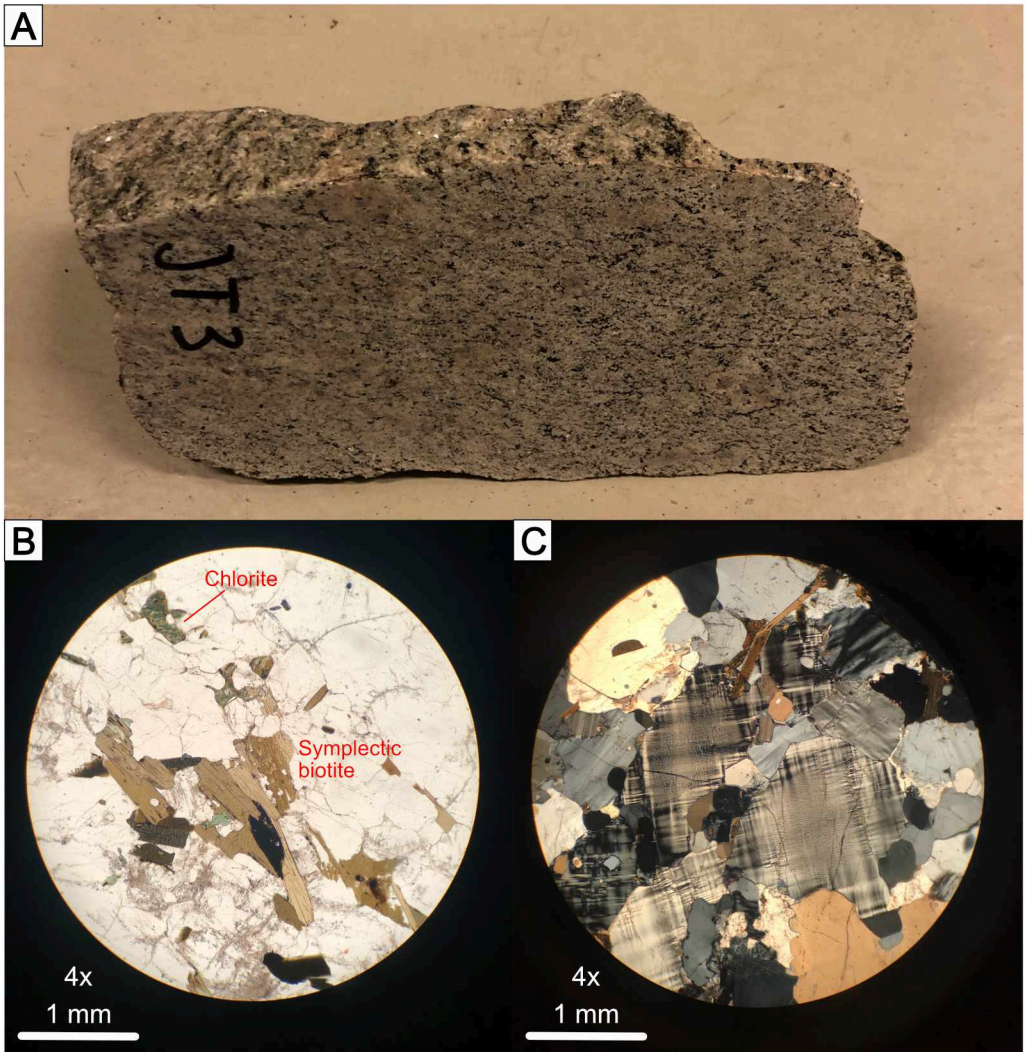

Figure 5.2: (A) Sample JT3, length ca. 8 cm. (B) Symplectic texture in biotite (biotite and quartz) and biotite altered by chlorite, PPL. (C) Perthitic texture in the center of microcline, XPL.

5.1.2 Sample JT8, granodioritic gneiss, Death Valley

This granodioritic gneiss is equigranular with phaneritic texture and randomly distributed minerals (Fig. 5.3A). The rock consists largely of K–feldspar, quartz and plagioclase, with minor components of brown and yellow biotite. Accessory minerals are zircons, apatite, allanite, rutile, and opaques. The K–feldspar grains are characterized by cross–hatched twinning and perthitic unmixing in the center (Fig. 5.3C). Plagioclase minerals show albite twinning, and some also have antiperthitic textures. Myrmekitic texture is found at the boundary of quartz and microcline minerals. The allanite grains, which are relatively large (~1 mm), have inclusions of rutile minerals and are rimmed by a reaction zone affecting the adjacent plagioclase and feldspar minerals (Fig. 5.3B). The reaction zone, most likely sericite, is probably a result of radioactive damage caused by high amounts of U and Th in the allanite. Typical metamorphic reactions present are recrystallized quartz with bulged grain boundaries, and undulose extinction. Plagioclase and K–feldspar grains are slightly sericitized.

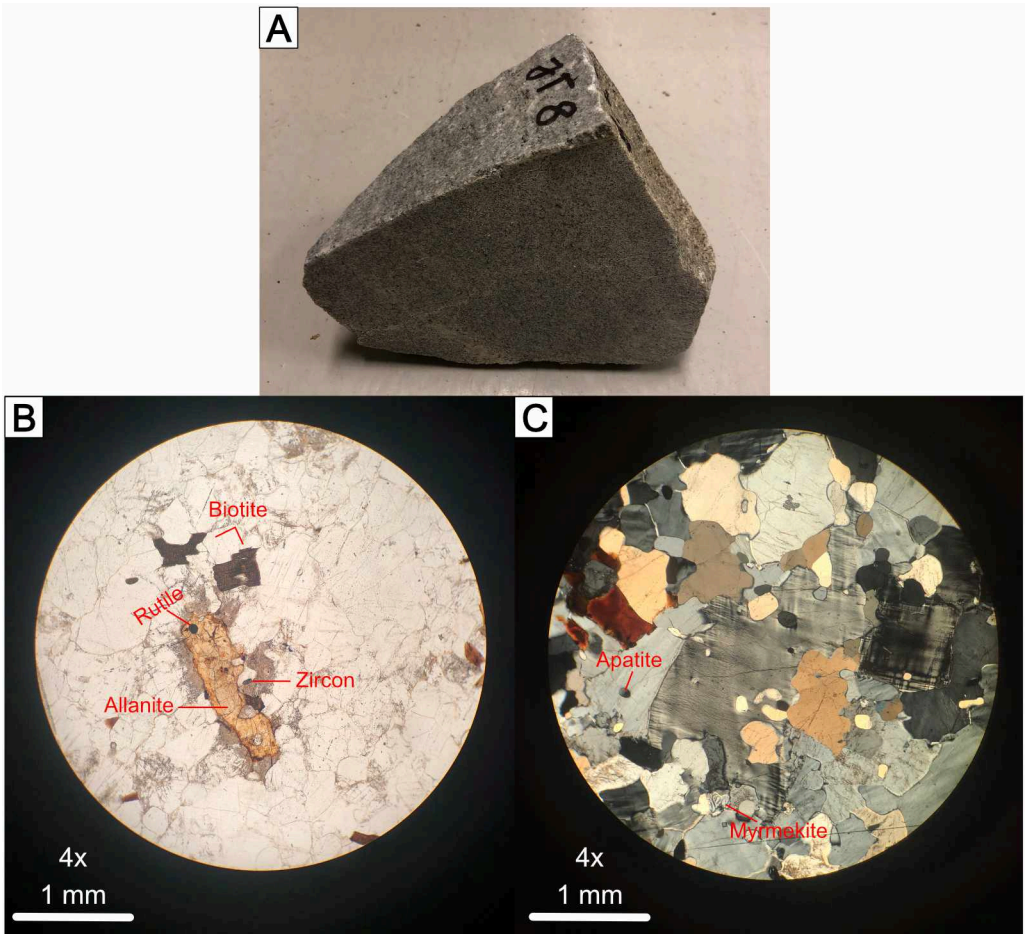

Figure 5.3: (A) Sample JT8 ca. 10 cm. (B) An allanite grain with a reaction rim (sericite) probably caused by radioactive damage, PPL. (C) Perthitic unmixing in microcline. Quartz display bulged grain boundaries indicating boundary migration, XPL.

5.1.3 Sample JT10, granodioritic gneiss, Death Valley

The hand–specimen of JT10 is equigranular with phaneritic texture. The rock shows a weak foliation, comprising of areas with a more felsic or mafic composition (Fig. 5.4A). The typical mineral assemblage is quartz, plagioclase, K–feldspar, yellow–green–brown biotite, and pyroxene. Zircon, apatite, allanite, and rutile are present as accessory minerals. Plagioclase has albite twinning, and some grains have fractures filled with biotite. This feature is also observed in feldspars (Fig. 5.4C). Myrmekitic texture is typically observed at the boundaries of quartz and plagioclase grains. Quartz is recrystallized and show undulose extinction, and in some cases, grains with lobate boundaries are visible (Fig. 5.4E). Lobate grain boundaries indicate recrystallization in high-temperature (500-700˚C) deformation resulting in grain boundary migration (GBM) (Passchier and Trouw, 2005). Retrogression of pyroxenes to chlorite is common, as well as biotite–quartz symplectic textures (Fig. 5.4B, C, D).

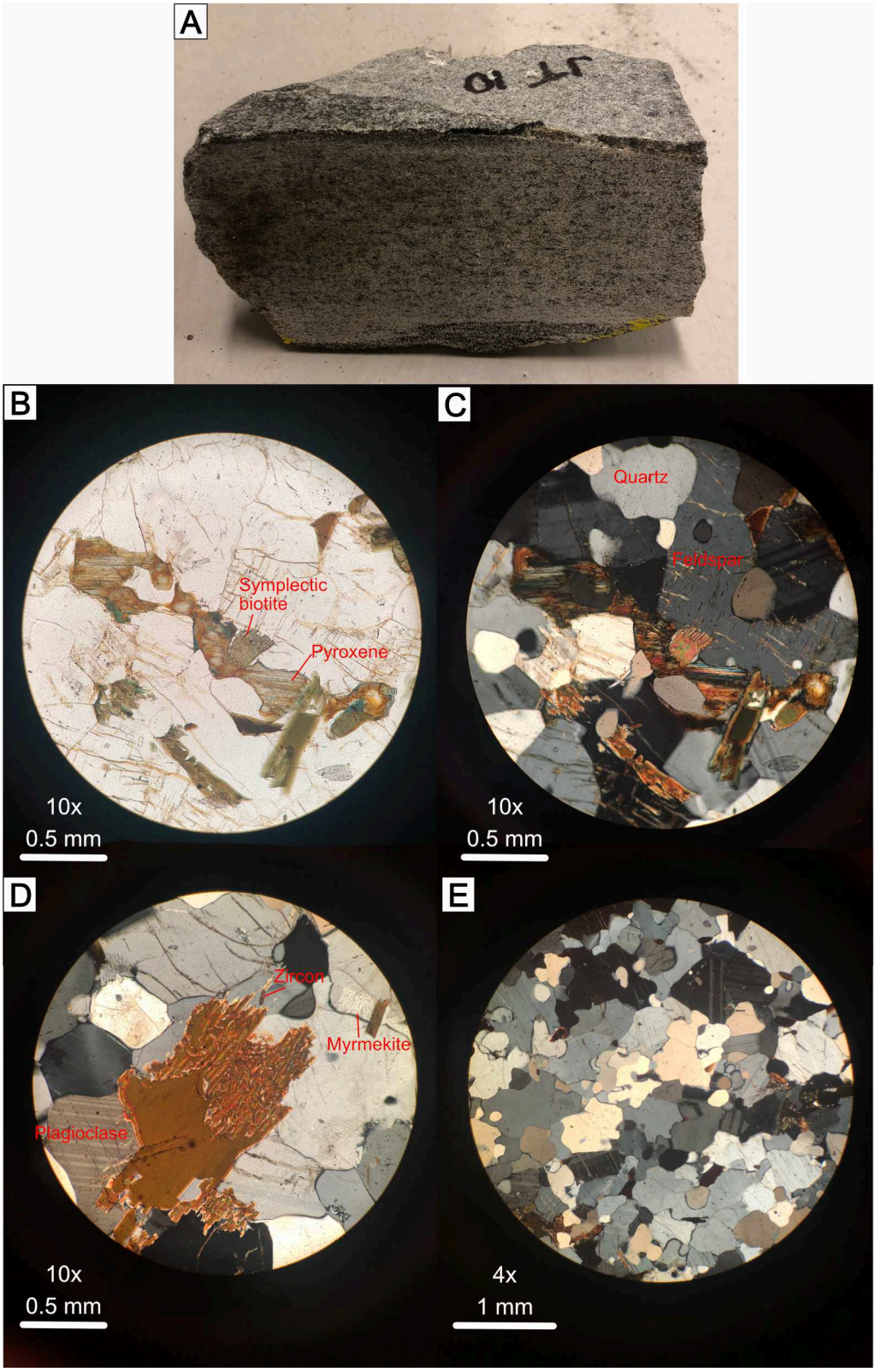

Figure 5.4: (A) Sample JT10 ca. 10 cm. (B) Symplectic texture in biotite. Pyroxene altered by chlorite, PPL. (C) Same image in XPL. Fractures in feldspar are filled with biotite. (D) Biotite forming symplectic intergrowths with quartz, XPL. E: Lobate grain boundaries within quartz grains, XPL.

5.1.4 Sample JT25, granitic–granodioritic gneiss, Sesseggen

This granodioritic gneiss has an equigranular, phaneritic texture. The rock shows foliation fabric that represents an S–tectonite (Fig. 5.5A). The thin section shows clear bands of light and dark minerals. The felsic minerals mainly consist of plagioclase (largest proportion), quartz, and a minor amount of K–feldspars, whereas the mafic minerals represent amphibole (hornblende) and biotite (Fig. 5.5B, C). Calcite and muscovite are present as minor constituents. Accessory minerals are titanite, zircon, apatite, allanite, and opaques. Titanite is found at the boundary of hornblende, or as inclusions. The K–feldspars show cross–hatched twinning and perthitic unmixing. Plagioclases have albite twinning. Quartz is recrystallized and shows both lobate and straight boundaries. Larger quartz grains typically form quartz ribbons with bulged boundaries, which often show undulose extinction (Fig. 5.5D). Ribbon quartz is common in high–grade rocks with temperatures above 700˚C (Passchier and Trouw, 2005). Several biotite minerals have partly been chloritized. Plagioclase is undergoing a reaction to sericite (Fig. 5.5E). The presence of secondary calcite minerals indicates a retrogression of the rock in a hydrothermal environment.

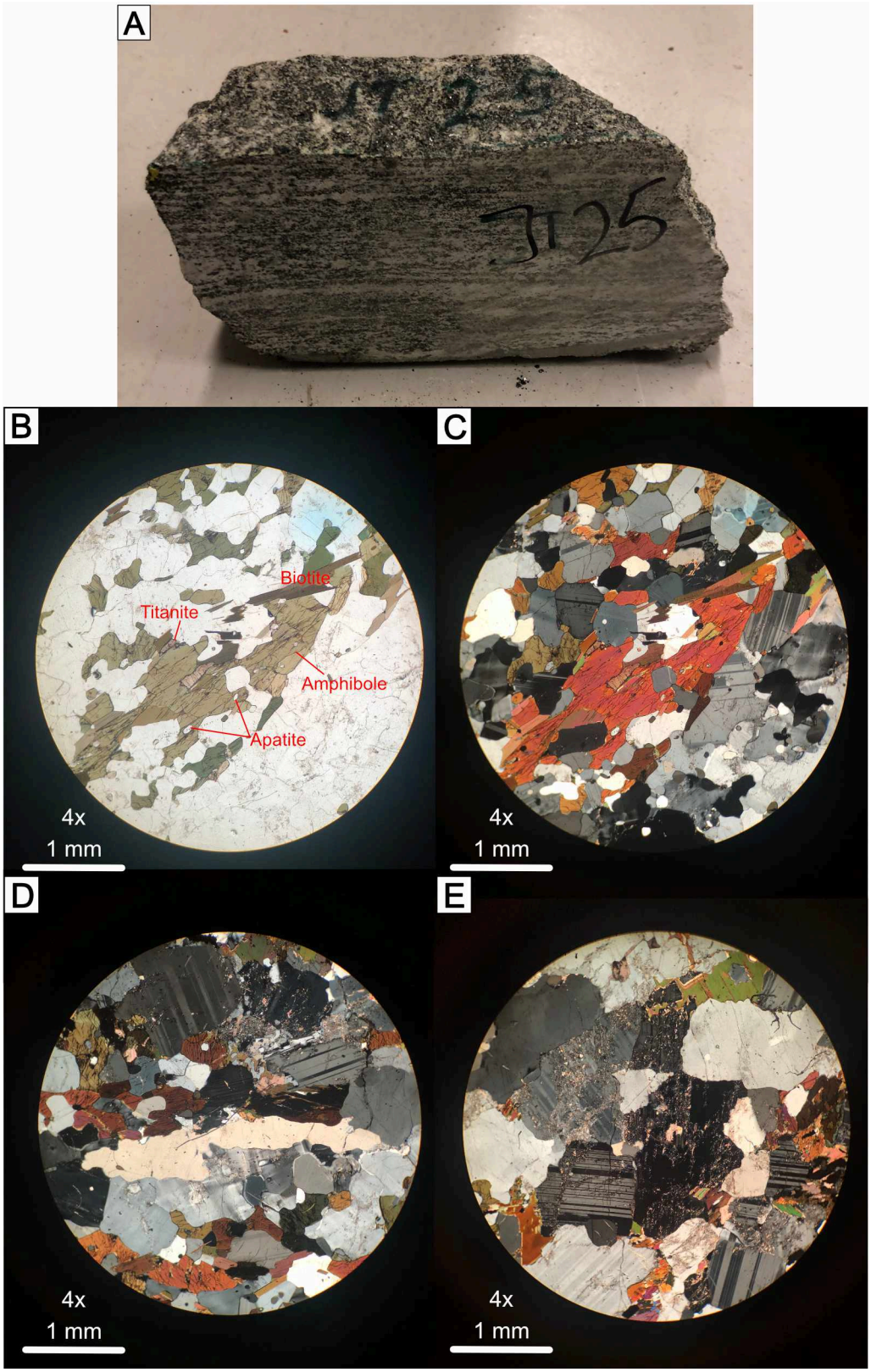

Figure 5.5: (A) Sample JT25, ca 12 cm. (B) Abundant amphibole minerals. Biotite and titanite commonly occur in contact with amphibole. The colorless minerals are quartz, plagioclase, and microcline, PPL. (C) Same image in XPL. (D) Ribbon quartz with bulged grain boundary, XPL. (E) Typical sericitized plagioclase found within this sample, XPL.

5.1.5 Sample JT27, granitic gneiss, Jutulhogget–SE

This granitic gneiss forms a porphyritic texture. The matrix has a phaneritic texture of both dark and light minerals, with dark phenocrysts embedded into the matrix. The phenocrysts are surrounded by a reaction rim of pink minerals (Fig. 5.6A). The phenocrysts may be magnetite with a reaction rim of K–feldspar. Under the microscope, the mineral assemblage is characterized by K–feldspar (microcline), quartz, plagioclase, and biotite. Allanite, opaques, apatite, and zircon occur as accessories. Minor components of muscovite and calcite are present (Fig. 5.6C). Both straight and lobate grain boundaries of quartz are observed. Retrogression is evident by highly sericitized plagioclase minerals and larger crystals of secondary muscovite in fractures (Fig. 5.6B). The alteration of plagioclase and K–feldspar is often concentrated at the center of the crystal, while the outlines are often unaffected (Fig. 5.6C, D). The main proportion of biotite is altered into chlorite (Fig. 5.6C, D).

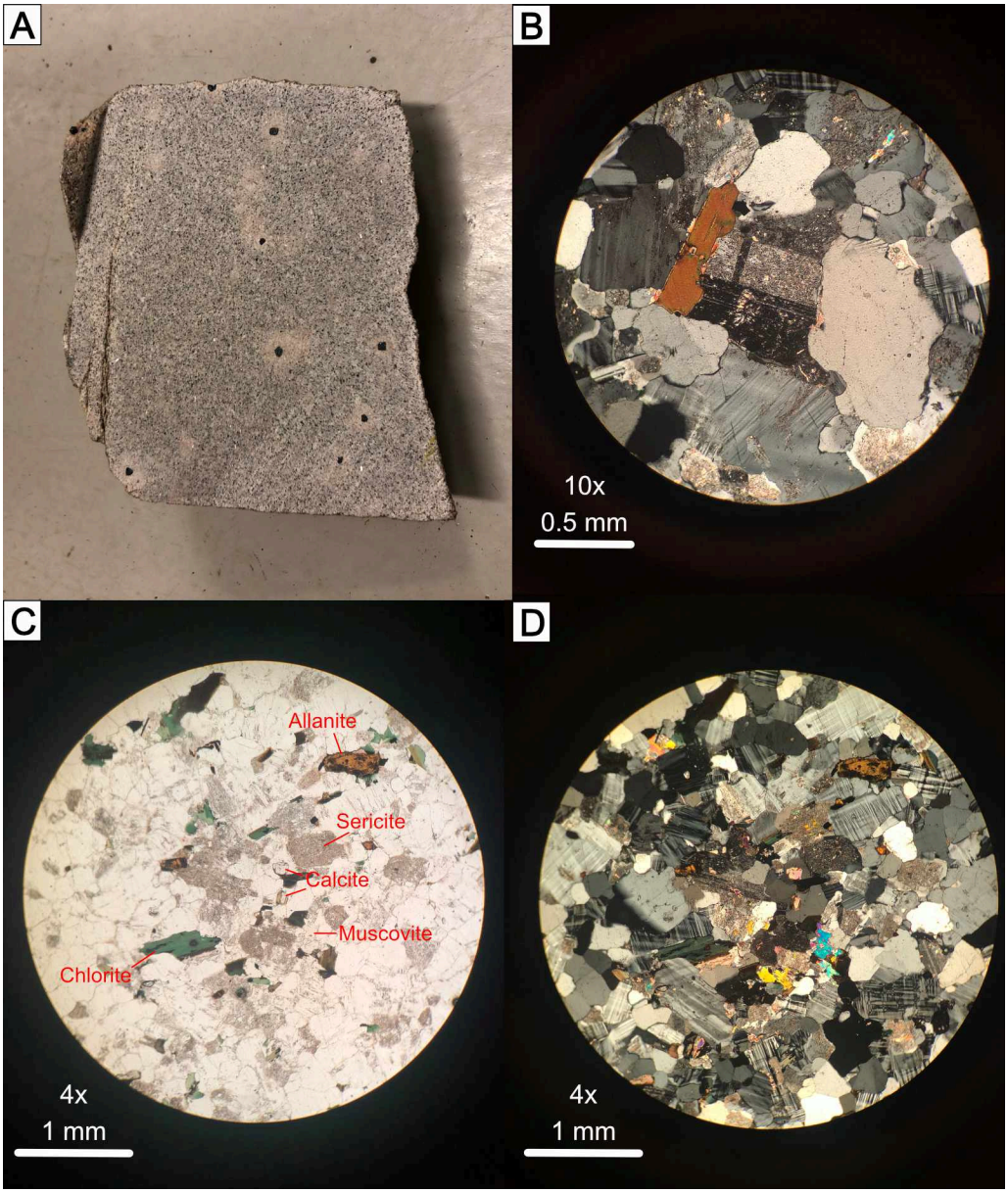

Figure 5.6: (A) Sample JT27, ca 7 cm. (B) Typical highly altered plagioclase. Biotite grain on the left side, XPL. (C) Overview image of the different minerals observed in the thin section. Biotite altered by chlorite. Larger secondary crystals of muscovite and calcite, PPL. (D) Same image in XPL. Microcline is very abundant in this sample.

5.1.6 Sample JT35, migmatitic gneiss, Klåvingen

The sample of JT35 has a migmatitic texture (Fig. 5.7A). The mineral assemblage is represented by plagioclase, quartz, K–feldspar (microcline), and biotite. Accessory minerals compose of zircon, apatite, and opaques. A few small garnets are also present (Fig. 5.7D, E). Myrmekite is commonly found at the boundaries of quartz and plagioclase minerals. Plagioclase typically shows albite twinning and forms the largest grains within the thin section. The larger plagioclase grains reveal antiperthite unmixing of K–feldspar (Fig. 5.7B). Antiperthite texture

indicates high temperatures under high–grade conditions followed by slow cooling (Best, 2002). Quartz is highly recrystallized, and the larger quartz grains typically reveal undulose extinction (Fig. 5.7C).

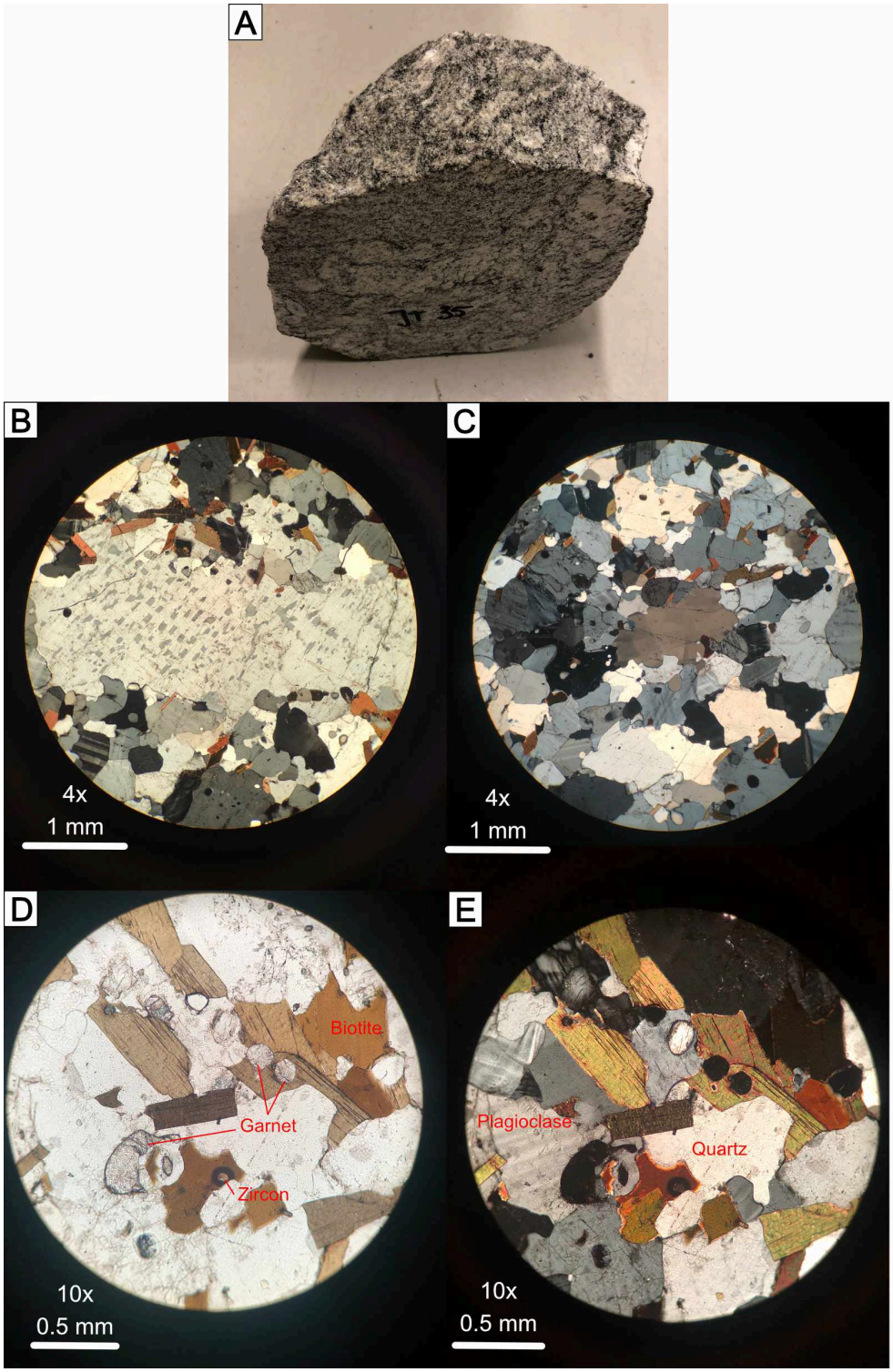

Figure 5.7: (A) Sample JT35, ca 8 cm. (B) A large plagioclase grain with antiperthitic unmixing of K–feldspar, XPL. (C) Typical bulged grain boundaries of quartz. The quartz grain in the center show undulose extinction, XPL. (D) Small garnet crystals within the sample, PPL. D: Same image in XPL.

5.2 Geochronological results

The following section will present the geochronological results for the six samples constrained by SIMS U–Pb zircon data. Description of the different features within the diagrams are illustrated in figure 5.8. The terminology used to describe morphology and internal textures within zircons are based on (Corfu et al., 2003). The interpretation of Th/U ratios is based on (Hoskin and Schaltegger, 2003), where relatively >0.5 indicate an igneous origin, and <0.5 reflects a metamorphic origin. The interpreted ages are ordered from old to young.

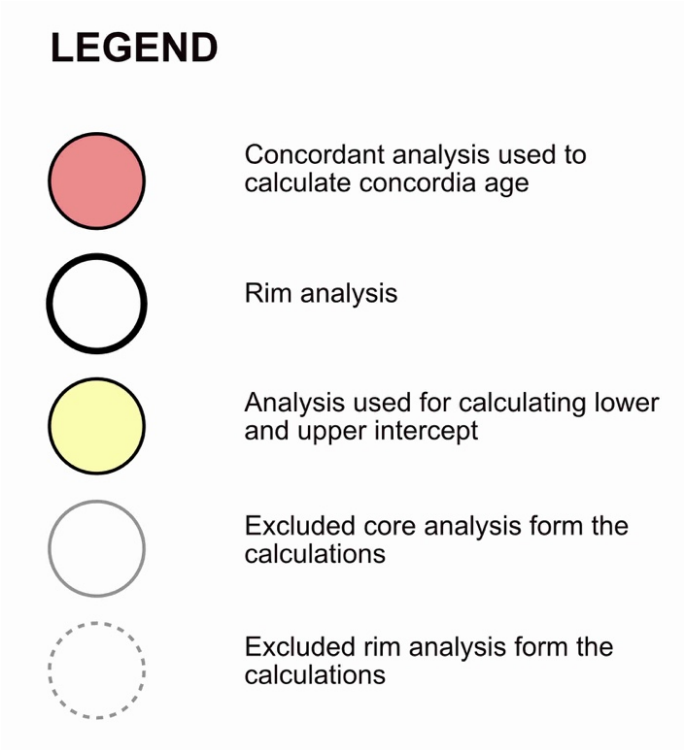

Figure 5.8: Legend illustration used for the geochronological data presented in the Tera–Wasserburg diagrams.

5.2.1 Sample JT3, Granitic gneiss, Jutulhogget–W

The sample contains mostly of rounded, anhedral to subhedral zircon grains. Most grains are between 100 – 150 μm in length, with a length/width up to 3. The crystals are mainly translucent and colorless. Inclusions are common, and a few grains show fractures. On CL–images, the grains show predominant magmatic texture characterized by core–rim structure of medium–dark oscillatory zoned cores surrounded by thin and structureless rims (Fig. 5.9C). Both low luminescence (dark) and high luminescence (bright) rims with homogenous texture are present. Fifteen spots were analysed on 14 different grains, targeting 13 cores and 2 rims. The U concentrations for the oscillatory cores are moderate, ranging from 368 ppm to 923 ppm (average = 589 ppm) (Appendix) The Th/U ratio ranges from 0.51 – 1.05 (average = 0.63), typical of magmatic zircons. The rims have U concentrations of 3797 ppm (Th/U = 0.06) and 364 ppm (Th/U = 0.6). The ten most concordant cores yield a concordia age of 1179±6 Ma (MSWD = 1.6) (Fig. 5.9A) and they have a weighted mean $^{207}Pb/^{206}Pb$ age of 1169±6 Ma (MSWD = 0.45, probability = 0.91) (Fig. 5.9B). The remaining three core analyses were excluded from the concordia calculation due to either recent Pb loss or significant reverse discordance (>5%). The concordia age is considered as the crystallization age of the igneous protolith. The two analysed rims were not considered further for any calculations due to either high reverse discordance (>5%) or clear evidence of recent Pb loss.

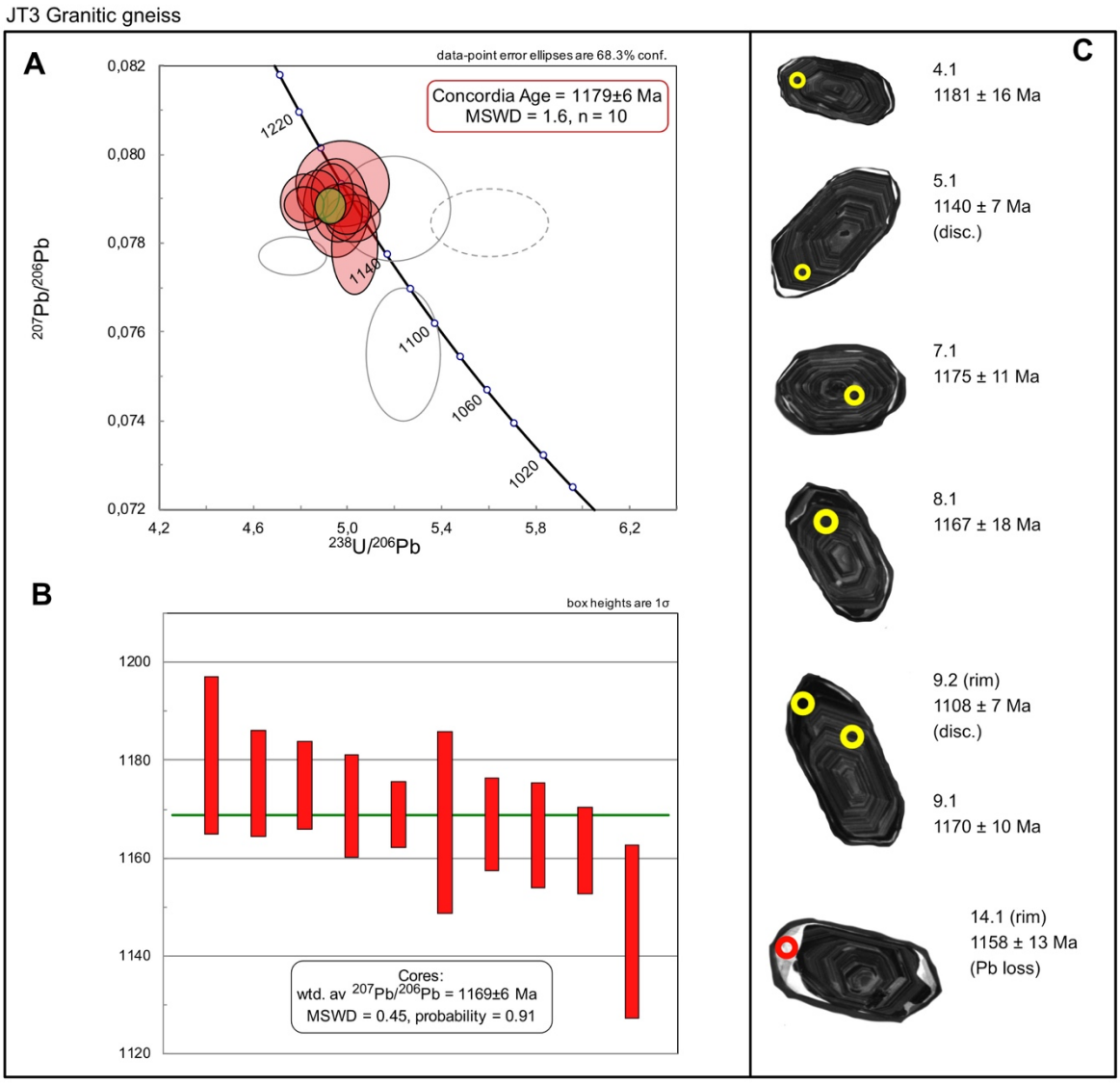

Figure 5.9: Results JT3: (A) Tera–Wasserburg plot of all analyses. All analyses are corrected data and error ellipses are plotted at the 1σ level. The concordia age (red) are given with 2σ–errors. (B) Weighted mean $^{207}Pb/^{206}Pb$ ages of the concordant ages (n = 10). Box heights are 1σ. (C) Representative CL–images with $^{207}Pb/^{206}Pb$ ages of analysed zircon grains. Analyses without description represent concordant analyses. Yellow/red circles mark the analysed spots with a diameter of ca. 25 µm for scale.

5.2.2 Sample JT10, granodioritic gneiss, Death Valley

Zircons from this sample are anhedral to subhedral, mostly rounded in shape with some more elongated crystals. The grains size ranges from 100 – 250 µm, with one grain exceeding up to 400 µm in length. The aspect ratio is ranging from 1 – 4. The grains appear translucent to dark brown in color with few inclusions. Fractures occur in some grains and are common in dark brown zircons. On CL–images, the internal textures of grains differ from weakly oscillatory zoned cores to structureless domains of low luminescence (dark) or high luminescence (bright). Two grains, spot 15–1 and 17–1, are weakly sector zoned. The rims are typically CL–dark and structureless and vary in thickness (Fig. 5.10B).

Nineteen analyses were performed on 16 different grains, placed on 8 zoned domains, 8 CL–dark and structureless domains, and 3 rims. The U concentrations for zoned domains and structureless domains range from 185 ppm to 7700 ppm (average =1503) (Appendix). In general, the structureless domains show higher U ppm values. Th/U ratios are spread from 0.30–2.44 (average = 0.83), implying magmatic origin. The rim analyses show U–enriched concentrations of 1073 ppm, 2635 ppm, and 1600 ppm, with Th/U ratios of 0.09, 0.12, and 0.37, respectively.

Many analyses are highly discordant, and the sample shows a complex age distribution. The oldest core age plotted (spot 11–1) reveals weakly oscillatory zoning, significant high U and Th content, and a high Th/U ratio (0.92). All the evidence leads to the conclusion that it is a magmatic inherited zircon implying an early stage of magmatism.

The weighted mean of $^{206}Pb/^{207}Pb$ ages for the four oldest analyses (apart from the inherited zircon), yield an age of 1170±11 Ma (MSWD = 1.02, probability = 0.38) (Fig. 5.10A). The two most concordant analyses of these give a concordia age of 1173±11 (MSWD = 0.37). The remaining zoned and unzoned analyses show significant Pb loss (ancient) or high reverse discordance. Two rims yield a concordia age of 1105±8 Ma (MSWD = 1.5). Spot 7–1 plots close to the rims. This spot could possibly be reinterpreted as core–rim mix, confirmed by the location of spot–analysis and similar high U content as the existing rims and a low Th/U ratio (0.35). The oldest rim (spot 16.2) is slightly reversely discordant and has a $^{206}Pb/^{207}Pb$ age of 1128±5 Ma. The age of 1170±11 Ma is interpreted as being close to the crystallization age of the igneous protolith. The older rim (spot 16.2) is interpreted to may reflect a subsequent metamorphic event, while the concordia age of the two other rims at 1105±8 Ma is interpreted to date a slightly younger metamorphic overprint.

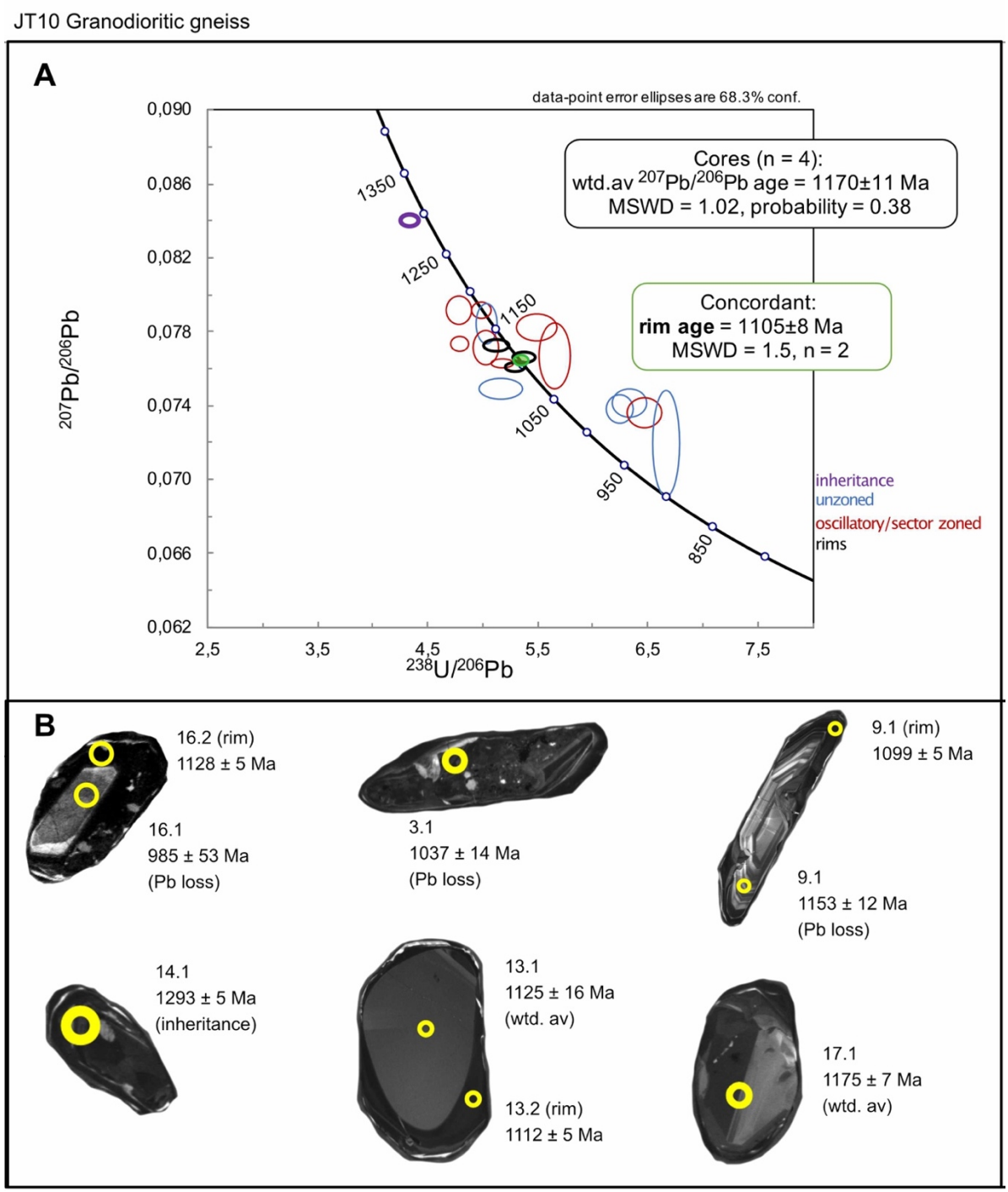

Figure 5.10: Result JT10: (A) Tera–Wasserburg plot of all analyses. All analyses are corrected data and error ellipses are plotted at the 1σ level. (B) Representative CL–images with $^{207}Pb/^{206}Pb$ ages of analysed zircon. Analyses without description represent concordant analyses. Yellow circles mark the analysed spots with a diameter of ca. 25 µm for scale.

5.2.3 Sample JT25, granitic–granodioritic migmatite gneiss, Sesseggen

The zircon grains of this sample are elongated, subhedral to anhedral, where several grains have rounded terminations. They are usually 200 µm long, with some grains exceeding up to 300 µm, with aspect ratios up to 5. In transmitted light, the grains are transparent with a tint of brown. The main proportion of the crystals have few, small inclusion and fractures, and some are fragmented. On CL–imaging, all zircon cores show CL–moderate–dark response and mainly appear zoned parallel to the c–axis, except a couple of grains that are homogenous and structureless (Fig. 5.11C). A few grains show weakly oscillatory zoned cores. The zircons are generally overprinted by CL–dark or CL–bright thin and structureless rims. Only a few grains have thick enough rims to be analysed. Their parallel zoning texture imply a magmatic origin.

A total of sixteen analyses were examined on fifteen different grains, most of which targeted parallel zoned cores and 2 rims. Average U concentration for the zircons range from 117 ppm – 549 ppm (average = 384 ppm), with one outlier having U concentration of 1487 ppm (spot 10–1) (Appendix). The Th/U ratio for the cores is mainly around 1, whereas those for rims are 0.21 and 0.79.

Four analyses, one rim and three unzoned cores, were extracted from further calculations due to high reverse discordance (>5%). The rim analysis of spot 12–2, appears as a mix of dark and bright mantle. This spot is reinterpreted to represent a concordant core analysis based on no significant deviations regarding U– or Th content and a Th/U ratio of 0.79, implying an igneous origin. In total, twelve core analyses define a concordia age of 1145±6 Ma (MSWD = 1.10) (Fig. 5.11A), and their weighted mean $^{207}Pb/^{206}Pb$ age is 1136±6 Ma (MSWD = 0.38, probability = 0.96) (Fig. 5.11B). The concordia age is considered as the igneous crystallization age of the igneous protolith.

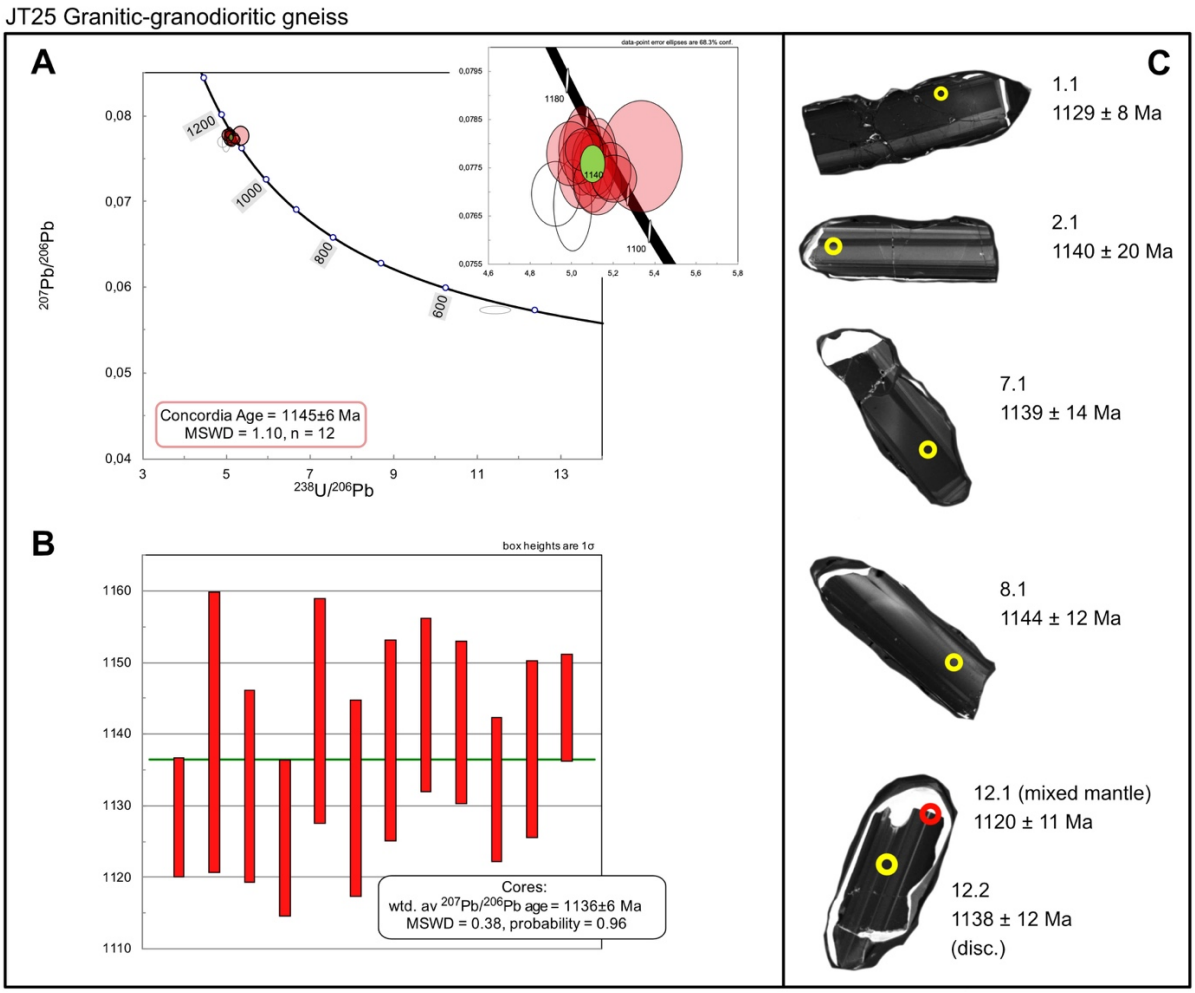

Figure 5.11: Result JT25: (A) Tera–Wasserburg plot of all analyses. All analyses are corrected data and error ellipses are plotted at the 1σ level. The concordia age (red) are given with 2σ–errors. (B) Weighted mean $^{207}Pb/^{206}Pb$ ages of the concordant ages (n = 12). Box heights are 1σ. (C) Representative CL–images with $^{207}Pb/^{206}Pb$ ages of analysed zircon. Analyses without description represent concordant analyses. Yellow/red circles mark the analysed spots with a diameter of ca. 25 µm for scale.

5.2.4 Sample JT8, granodioritic gneiss, Death Valley

Zircons separated from this granulitic granodioritic gneiss are elongated, subhedral to euhedral with slightly rounded terminations. The grain size varies from 150 – 250 µm in length, with an aspect ratio of 2 – 4. The zircons are light to dark brown in color. Both fractures and inclusion occur in some grains. On CL–images, the majority of zircons display weak oscillatory zoning texture (Fig. 5.12C). Oscillatory zoned core textures are common in magmatic zircons. Several grains are structureless due to CL–dark response. Dark homogenous, unzoned rims of variable thickness are common, but in general, slightly thicker at the grain terminations.

A total of seventeen spots were analysed from 16 different grains, including 9 weakly oscillatory zoned cores, 6 CL–dark and structureless domains, and 2 rims. The U concentration for the cores range from 403 ppm to 1991 ppm (average = 1039 ppm), with Th/U ratios from 0.44 – 1.0 (average = 0.72), typical of a magmatic origin (Appendix). Both the structureless domains and the rims are highly enriched in U, with a concentration spread from 911 ppm to 5949 ppm (average = 2981 ppm), with one outlier of 10545 ppm. In general, there is a strong correlation between high U concentrations and discordance. The Th/U concentrations for the structureless domains range from 0.06 – 0.7, whereas the rims have Th/U ratio of 0.01 and 0.11. Such low Th/U ratios are typical of a metamorphic origin.

The plotted analyses show scatter due to significant Pb loss. The oldest group of zircons generally show oscillatory zoning, whilst the remaining younger analyses show CL–dark response. Four of nine analyses on cores yield a concordia age of 1131±9 Ma (MSWD = 1.7) (Fig. 5.12A). The concordant analyses define a weighted mean $^{207}Pb/^{206}Pb$ age of 1134±23 Ma (MSWD = 2.1, probability = 0.1) (Fig. 5.12C). The remaining core and structureless analyses show significant Pb loss and/or high analytical errors.

The rim analyses, spot 5–1 and 2–1, yield $^{206}Pb/^{238}U$ ages of 560±6 Ma and 530±9 Ma, respectively. When the rim analyses are plotted for common ^{204}Pb–corrected data, the rims tend to plot as overcorrected, whereas plotted with uncorrected data, the rim analyses lie closer to the concordia line. The overcorrection tends to only affect the Pan–African ages. Based on this observation, the rim ages are probably more concordant than illustrated in the Pb common corrected diagram. One unzoned domain analysis, spot 14–1, has a significantly younger $^{206}Pb/^{238}U$ age of 546±6 Ma. This spot has high U and Th content together with a low Th/U value (0.06) probably represent a mixed age and is reinterpreted as a rim. The weighted mean $^{206}Pb/^{238}U$ age of the three rims are 549±33 Ma (MSWD = 4.2, probability = 0.015). The age of ca. 1131 Ma is considered as the crystallization age of the protolith of the granodioritic

gneiss. The representative rim ages are considered to represent the approximate age of metamorphism during a later Pan–African tectono–thermal event.

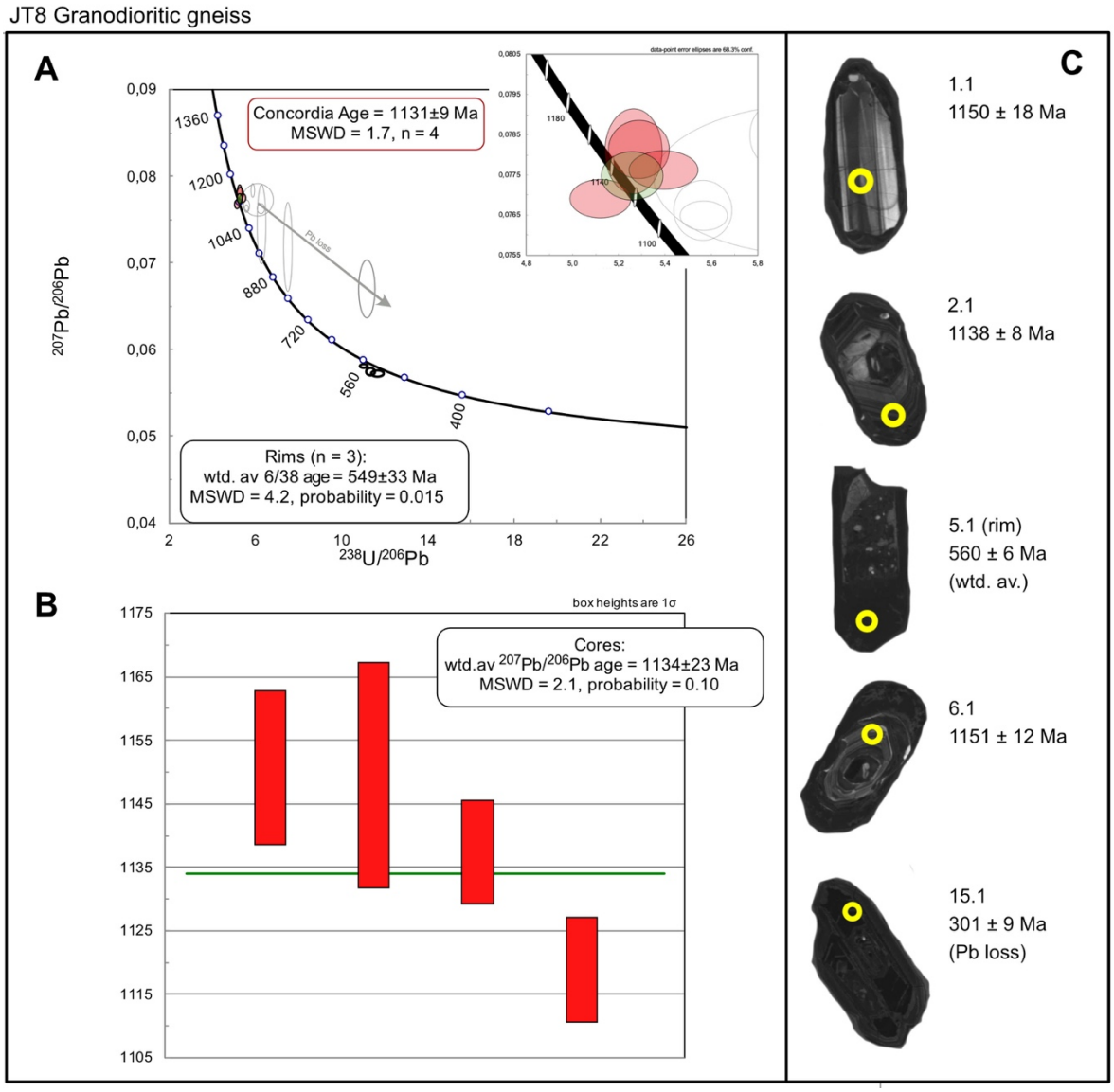

Figure 5.12: Result JT8: (A) Tera–Wasserburg plot of all analyses, expect two analyses (13.1 and 15.1) which were excluded because of large analytical errors. All analyses are corrected data and error ellipses are plotted at the 1σ level. The concordia age (red) are given with 2σ–errors. (B) Weighted mean $^{207}Pb/^{206}Pb$ ages of the concordant ages (n = 4). Box heights are 1σ. (C) Representative CL–images with $^{207}Pb/^{206}Pb$ ages of analysed zircon cores and $^{206}Pb/^{238}Pb$ ages from the rim and spot 15.1. Analyses without description represent concordant analyses. Yellow circles mark the analysed spots with a diameter of ca. 25 µm for scale.

5.2.5 Sample JT35, migmatitic gneiss, Klåvingen

The zircons separated from this sample are elongated, subhedral with rounded terminations. The zircons are reaching up to 400 µm in length, with aspect ratios of 4. In transmitted light, the zircons are mostly dark brown making inclusions hard to identify, whereas, in the more clearer grains inclusions are common and can also be observed in reflected light and CL–images. On CL–images several grains reveal apatite inclusions. Fractures and fragmentation do also occur in several grains, and several grains are metamict. The observed internal texture implies that zircons are of a magmatic origin as the main proportion of zircons show CL–dark response and are characterized by weakly oscillatory zoned cores. The oscillatory zoning patterns in some cores are faded or almost homogenous, and a few grains appear structureless (Fig. 5.13C). Wider unzoned rims of low luminescence overgrow a few grains. However, the grains mainly have thin and structureless rims, making them unsuitable for analyses. Therefore, no rims were analysed for this sample.

Eighteen analyses were places on 18 grains were analysed, including 9 weakly oscillatory zoned cores, 5 unzoned cores, and 4 CL–dark and structureless domains. The U concentrations are wide in range from 156 ppm to 4945 ppm (average 1578 ppm) (Appendix). The structureless domains represent the highest U values (average = 3347 ppm). There is a strong correlation between high U content and Pb loss. Th/U ratios range from 0.002 to 0.92 (average = 0.31). The analyses are scattered due to significant Pb loss. Five analyses were omitted from any further calculations based on either high common Pb content, Pb loss or high reverse discordance (>5%). Four core analyses define a concordia age of 1061±9 Ma (MSWD = 1.5) and the weighted mean $^{206}Pb/^{207}Pb$ age of them is 1067±10 Ma (MSWD = 0.56, probability = 0.64) (Fig. 5.13A). The remaining discordant ages from both unzoned and oscillatory zoned domains were anchored at the concordia age in the upper intercept and defined a discordia line with a lower intercept at 496±9 Ma (MSWD = 1.18) (Fig. 5.13A). A discordia line without being anchored gives an upper intercept at 1081±19 Ma and a lower intercept at 509±31 Ma (MSWD = 0.82) (Fig. 5.13B). The former overlaps with the concordia age, and the latter overlaps the anchored lower intercept age. The concordia age is interpreted to represent the crystallization age of the igneous protolith, while the anchored lower intercept age is considered to date the Pan–African tectono–thermal reworking of the igneous protolith.

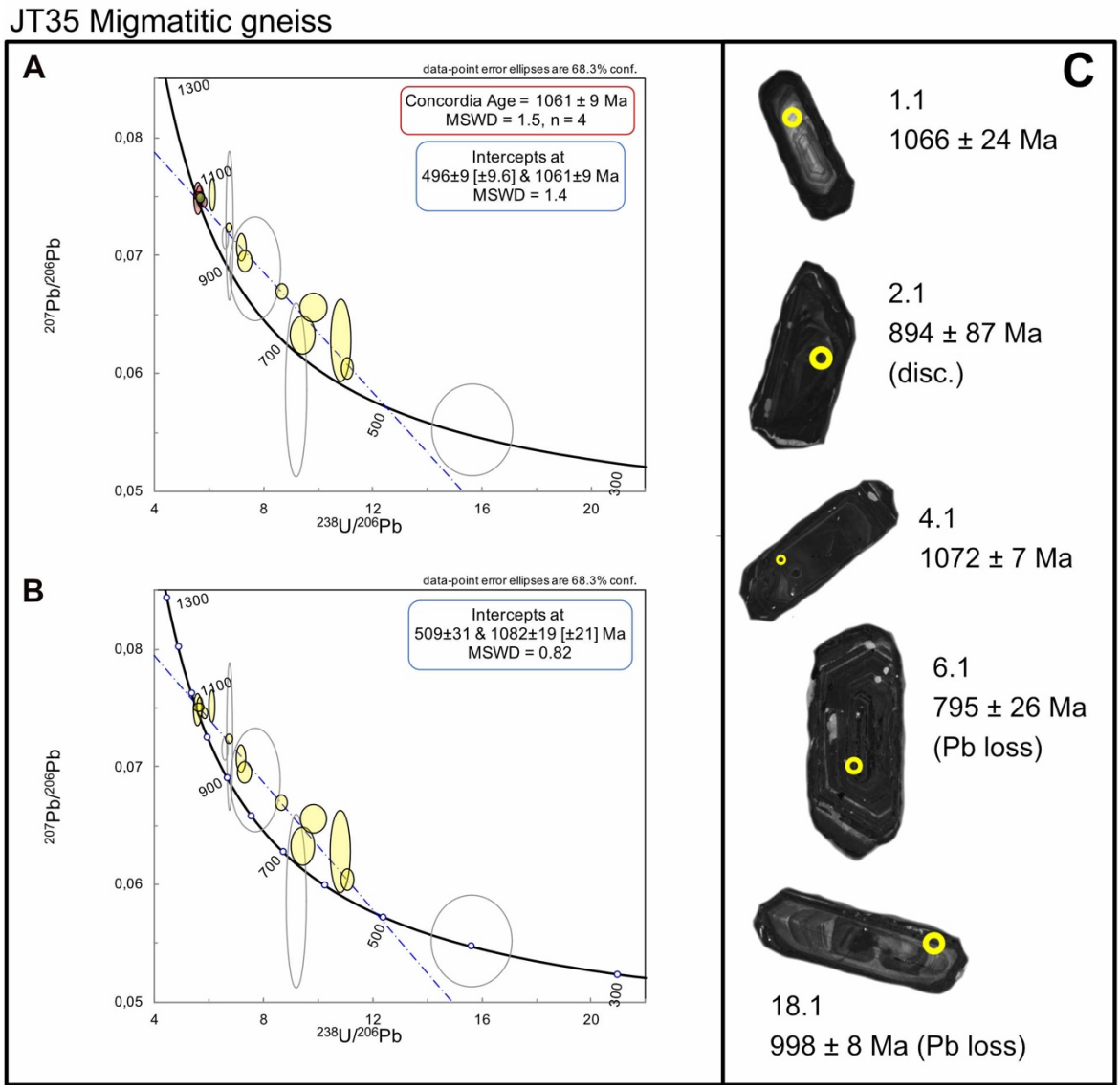

Figure 5.13: Result JT35: (A) Tera–Wasserburg plot of all analyses. All analyses are corrected data and error ellipses are plotted at the 1σ level. The concordia ages (red) are given with 2σ–errors. A discordia line is defined by nine discordant analyses (yellow), giving a lower intercept age at ca. 496 Ma. (B) The non–anchored discordia line defines an upper and lower intercept at ca. 1082 Ma and 509 Ma, respectively. (C) Representative CL–images with $^{207}Pb/^{206}Pb$ ages of analysed zircon. Analyses without description represent concordant analyses. Yellow circles mark the analysed spots with a diameter of ca. 25 µm for scale.

5.2.6 Sample JT27, granitic gneiss, Jutulhogget–SE

The zircons extracted from this sample are dominated by anhedral to subhedral prisms where most grains appear as equant to elongate. The size of the crystals is around 150 μm, with a length/width ratio of 3. Some grains exceed up to 200 μm and have a length–width ratio of 4 – 5. All crystals are dark brown in color. Fragmentation and fractures occur in some grains, and inclusions are common. In CL–images, all zircons show CL–dark response, and internal textures cannot be identified (Fig. 5.14C).

Seventeen spots were carried out on 17 different grains, all placed on CL–dark and structureless domains. The U concentrations are relatively high ranging from 685 ppm to 5116 ppm (average = 2620 ppm). The Th/U ratios vary from 0.03 – 1.14 (average = 0.53) (Appendix). One analysis (spot 6–1) appears as an outlier with the highest U ppm and Th ppm values of 6100 ppm and 6309 ppm, respectively, and show significant evidence of Pb loss. A total of nine analyses were omitted from the concordia calculation due to either high common Pb, Pb loss, or high reverse discordance (>5%). Two analyses (spot 13.1 and 15.1) have relatively high common Pb, which affects the $^{207}Pb/^{206}Pb$ ages when using corrected data resulting in large age errors. However, when plotted, the analyses are concordant and are therefore included in the concordia calculations. In total, eight analyses yield a concordia age of 497±4 Ma (MSWD = 0.83) (Fig. 5.14A). The weighted mean $^{206}Pb/^{238}U$ ages of these concordant spots give an age of 497±5 Ma (MSWD = 1.4, probability = 0.19) (Fig. 5.14B). The concordia age is interpreted as the igneous crystallization age for the granitic protolith and is consistent with the emplacement time of voluminous Pan–African intrusions.

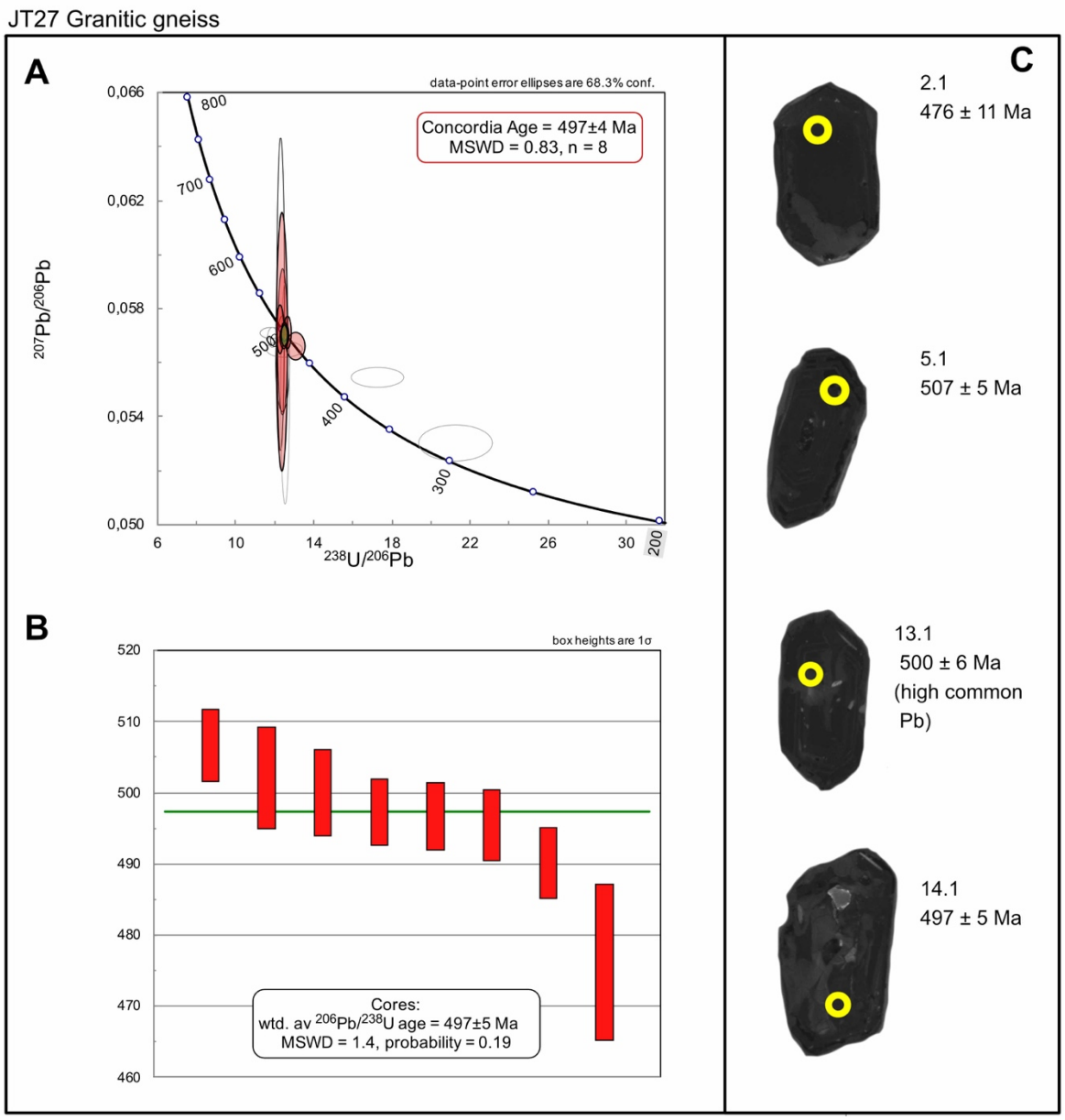

Figure 5.14: Result JT27: (A) Tera–Wasserburg plot of all analyses. All analyses are corrected data and error ellipses are plotted at the 1σ level. The concordia age (red) are given with 2σ–errors. (B) Weighted mean $^{206}Pb/^{238}Pb$ ages of the concordant ages (n = 8). Box heights are 1σ. (C) Representative CL–images with $^{206}Pb/^{238}Pb$ ages of analysed zircon. Analyses without description represent concordant analyses. Yellow circles mark the analysed spots with a diameter of ca. 25 µm for scale.

5.3 Age distribution from the different samples

The U–Pb geochronological results of the dated samples are summarized in fig. 5.15. Five out of six samples record Mesoproterozoic ages at ca. 1179 Ma, 1170 Ma, 1145 Ma, 1131 Ma, and 1061 Ma. One sample record a significantly younger age of ca. 497 Ma, strongly related to the Pan–African event. Mesoproterozoic metamorphism is recorded by sample JT10, this sample is the only to show zircon inheritance. Two of the samples with Mesoproterozoic protolith ages report Pan–African metamorphic overprint at ca. 549 Ma and ca. 496 Ma. Fig. 5.16 shows the geographical position of the samples along with their calculated crystallization age.

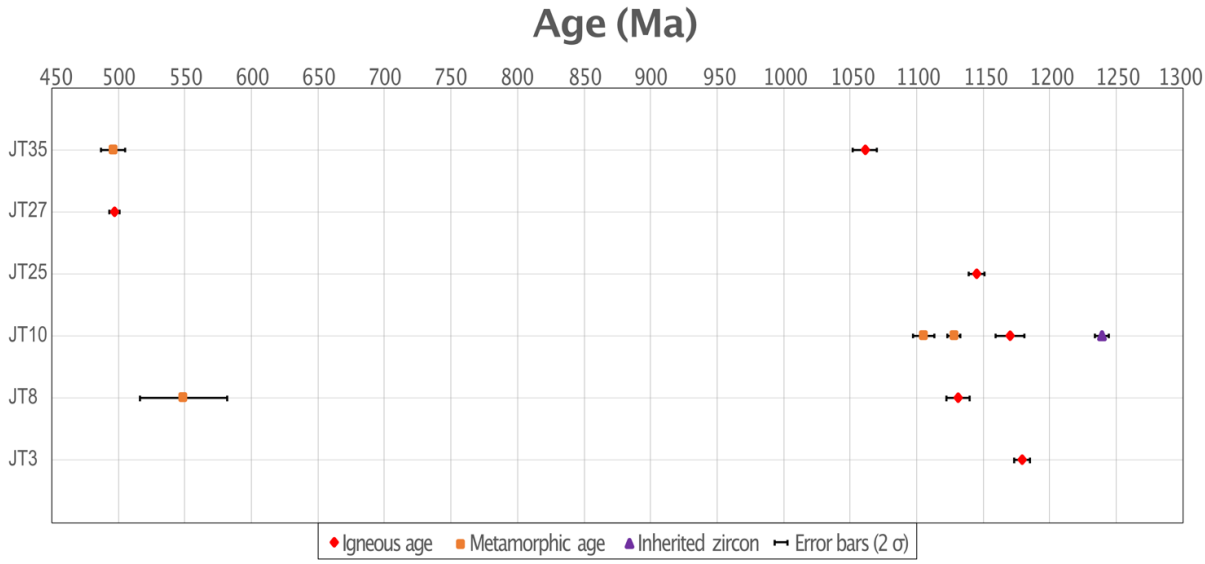

Sample	Igneous age (Ma)	Metamorphic age (Ma)	Inherited zircon (Ma)
JT35	1061±9	496±9 (lower intercept)	
JT27	497±4		
JT25	1145±6		
JT10	1170±11 (wtd. mean)	1128±5 (only one) 1105±8	1239±5
JT8	1131±9	549±33 (wtd.mean)	
JT3	1179±6		

Figure 5.15: Summary of geochronological data with corresponding table.

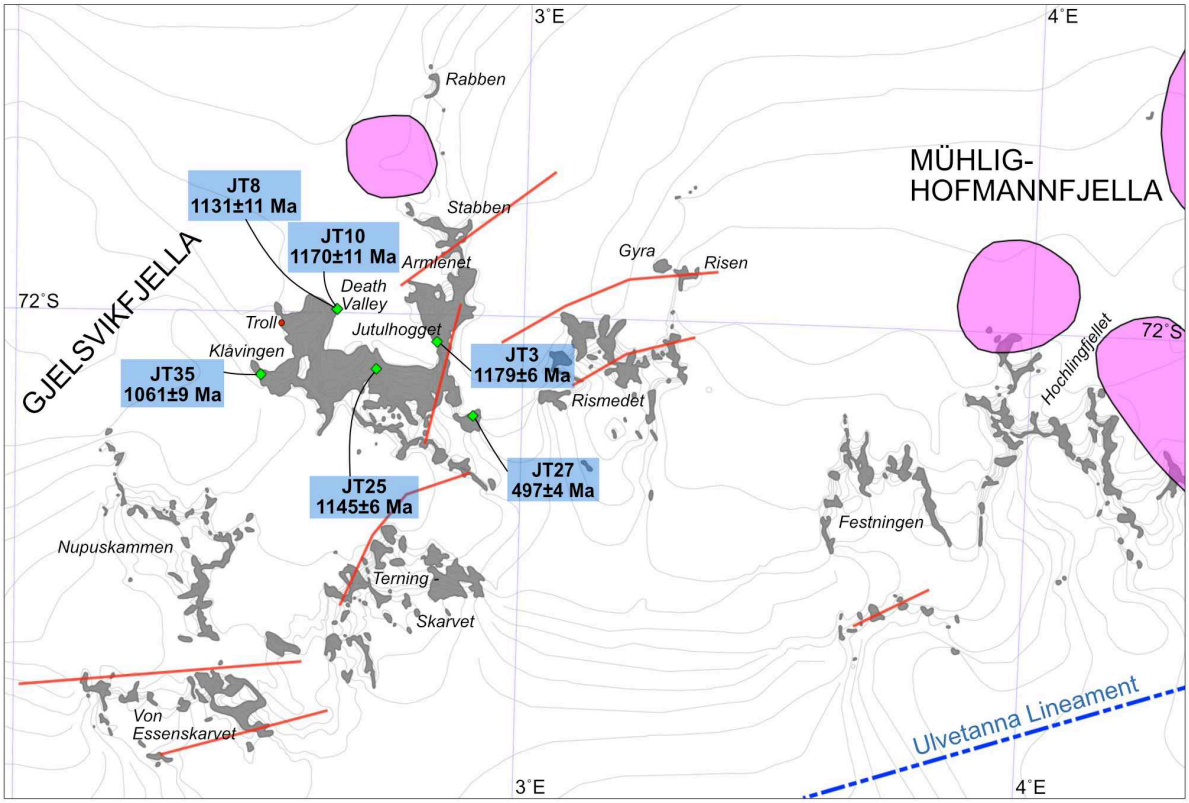

Figure 5.16: An overview of the sample localities with their representative crystallization age obtained from this study.

6 Discussion and interpretation

The following section compares the data from the result chapter. Here the magmatic and metamorphic features are presented, contributing to the understanding of their formation and evolution. Afterward, implications for the obtained ages will be further discussed in relation to the existing geochronological data constrained for the Maud Belt.

6.1 Interpretation of the geochronological and petrological results of the samples

The study aimed to investigate Grenville–age magmatism within Jutulsessen, Gjelsvikfjella. The constrained U–Pb zircon ages from this study show strong similarities with the existing literature of the Grenville–age magmatic event in Dronning Maud Land. Therefore, this study is thus confirming the occurrence of Grenville–age rocks in Gjelsvikfjella. The oldest age detected (JT10), interpreted as an inherited zircon, gave an age of ca. 1240 Ma. It supports previous findings in the area and adjacent areas that the basement rocks compose of Grenville–age crust with the involvement of older components (e.g. Wang et al., 2020; Bisnath et al., 2006; Baba et al., 2015). Grenville–age magmatism is reported by five samples (JT3, JT8, JT10, JT25, and JT35), and one sample (JT27) reveals a Pan–African crystallization age. The interpretation of these igneous protolith ages is based on the occurrence of typically igneous oscillatory zoned zircons, and higher Th/U ratios (> 0.5) (Corfu et al., 2003; Hoskin and Schaltegger, 2003). One sample records Mesoproterozoic metamorphism (JT10), and two of the Mesoproterozoic rocks (JT8 and JT35) indicate metamorphic overprint during Pan–African times. These metamorphic ages are recorded by single grains or rim overgrowths characterized by low Th/U ratios (< 0.5) and CL–dark response (Corfu et al., 2003; Hoskin and Schaltegger, 2003). Corrected data was used for all analyses.

Sample JT3, JT8, JT10, JT25, and JT35

The following samples, JT3, JT8, JT10, JT25, and JT35, are interpreted to form an age group reflecting Grenville–age magmatism. All these samples have igneous protolith ages between ca. 1179–1061 Ma and were formed within the same geological event in late Mesoproterozoic times. The crystallization ages are based on magmatic zircon textures and Th/U ratios typical of magmatic zircons (> 0.5).

The samples typically have high U concentrations, and a few samples have a significant amount of discordant analysis. This was typical of sample JT10, where the U–Pb age analysis showed zircons with high U concentrations and gave a high number of discordant analyses. The plotted analyses were scattered, which made the age interpretation complicated. The crystallization age was calculated from a weighted mean age based on the oldest concordant analysis. In addition to the obtained igneous age, one inherited zircon and two metamorphic ages from rim overgrowths was recorded. The inherited zircon suggests a magmatic origin based on weak oscillatory zoning and a high Th/U ratio (0.9), while the rims were structureless with low Th/U ratios (0.09–0.3), typical of a metamorphic origin.
The remaining analysed samples typically had a high number of concordant analyses which made them relatively straightforward to interpret.

In addition, two of the investigated samples (JT8 and JT35) indicate metamorphic overprinting between ca. 550–500 Ma, consistent with Pan–African metamorphism. The metamorphic age of JT8 is based on rim overgrowths and low Th/U ratios (< 0.1), typical of a metamorphic origin. For sample JT35, a lower intercept ages were defined by analyses of ancient Pb loss.

All samples show a granitic–granodioritic composition comprising of quartz, plagioclase, and K–feldspar (microcline) as the dominating minerals. Biotite occurs in all samples but in variable amounts. Plagioclase typically predominates over microcline, suggesting an average granodioritic composition of the protoliths. However, JT10 has small differences in its mineral assemblage compared to the other samples. No microcline is observed within JT10, which points to a more tonalitic composition. In general, a granodioritic composition is typical of an island arc and continental volcanic arc setting.

The mineral assemblage of quartz–felspar granitoids often provides limitation regarding their metamorphic conditions as typical index minerals implying different temperature and pressure conditions are rarely present. The samples are interpreted to have undergone medium to high–grade metamorphism. Although there are slight variations in metamorphic characteristics, the common metamorphic textures and microstructures point towards at least upper amphibole facies metamorphic conditions. Common for all samples are a granoblastic texture and highly recrystallized quartz grains, commonly with undulose extinction. In addition, sample JT25 is abundant in amphiboles, JT10 contains pyroxenes, and JT35 has a migmatitic texture and contains garnets. All these features are good indications of high–grade metamorphism

(amphibolite or higher metamorphic grades). Previous data propose that the Maud Belt has experienced polydeformation metamorphism, once in the late Mesoproterozoic and again in late Neoproterozoic–early Paleozoic times. High–grade rocks, reaching up to medium–high–P granulite–facies conditions, are reported throughout the Maud Belt (Engvik and Elvevold, 2004; Bisnath and Frimmel, 2005; Board et al., 2005). Most of the metamorphic mineral assemblage found are related to the Pan–African tectono–thermal event. Following the peak granulite–facies conditions, a near–isothermal decompression evolution is typically documented by migmatites, symplectic textures, and coronas surrounding garnets. The metamorphic reactions of the investigated quartz–feldspar granitoids within this study are indeed representative of a high–grade metamorphic terrane, as expected from previous descriptions of the basement rocks.

All samples, except JT35, show clear evidence of retrogressive metamorphism. Typically, plagioclase, and in some cases K-feldspar, are replaced by sericite, indicating hydrothermal alteration processes in the rock. This is further supported by the presence of larger secondary muscovite and calcite minerals. Biotite was often partly chloritized, and some of the samples indicate fully alternation of biotite to chlorite. Several samples have symplectic biotite.

Sample JT27

Contrary to the other investigated samples, sample JT27 yields a much younger age (Pan–African). This sample is interpreted to represent a granitic rock that crystallized at 497±4 Ma. The interpretation is based on zircon characteristics and Th/U ratios (~0.5) of igneous zircons. The zircons have an almost CL–dark response however post–CL images revealed weak oscillatory zoning. The mineralogical composition is similar to the Grenville–age rocks. However, microcline is more abundant in this sample. The sample shows a granoblastic texture and is interpreted to also have undergone high–grade metamorphism. Sericitized plagioclase and chloritized biotite are typical in this sample, indicating that hydrothermal fluids affected the rock. In addition, large secondary muscovite and calcite are observed, and their observed appearance implies a late–tectonic process (e.g. hydrothermal alteration).

6.2 Comparison of new dating data to reported ages in Gjelsvikfjella

The new U–Pb zircon data presented herein are comparable with the existing Mesoproterozoic magmatic ages reported from the study area and adjacent nunataks within Gjelsvikfjella–

Mühlig–Hofmannfjella (Fig. 6.1). From the six investigated felsic gneisses, five of them indicate Grenville–age magmatism: JT3, JT8, JT10, JT25, and JT35 (Fig. 5.15).

The two oldest samples, JT3 and JT10, gave crystallization ages of 1179±6 Ma and 1170±11 Ma, respectively. These ages are comparable to a Grenville-age reported by Paulsson and Austrheim (2003). From SIMS U–Pb zircon data they dated a migmatitic gneiss in the study area at 1163±6 Ma. Together, these older Mesoproterozoic ages imply the initial formation of the Grenville–age basement rocks, which typically comprise of felsic compositions.

Sample JT25, yields a slightly younger concordant age of 1145±6 Ma and do also report Grenville–age magmatism within Jutulsessen. Similar ages have been reported in Gjelsvikfjella by Jacobs et al. (2003b) and Bisnath et al. (2006). Both reported SHRIMP U–Pb zircon data from migmatitic gneisses at 1142±12 Ma and 1143±41 Ma, respectively.
Furthermore, these authors also reported crystallization ages which are indistinguishable from sample JT8 (1131±9 Ma) in this study. Two investigated migmatitic gneisses from Bisnath et al. (2006) constrain magmatic zircon ages of 1133±16 Ma and 1130±19 Ma. Also, the ca. 1133 Ma gneiss shows an inherited zircon of ca. 1200 Ma, similar to the inherited zircon from sample JT10 in this study. Furthermore, SHRIMP U–Pb zircon data from Jacobs et al. (2003b) reports a migmatitic gneiss with Mesoproterozoic zircon cores at 1137±14 Ma close to the Jutulsessen nunatak (Risemedet).

The concordia age of sample JT35 gave the youngest Grenville–age of the investigated samples, dated to 1061±9 Ma. The zircons are characterized by oscillatory zoned cores with moderate Th/U ratios (~0.4), indicating a magmatic origin. Compared against previous discoveries within Gjelsvik–Mühlig–Hofmannfjella, the presented age herein represents the so far youngest evidence of Grenville–age magmatism. Slightly older U–Pb zircon ages around 1090–1080 Ma have been reported by Jacobs et al. (2003a), Jacobs et al. (2003b), and Jacobs et al. (2008a) in the area. An upper intercept age was also calculated for sample JT35, giving an age of 1082±19 Ma, which is in good agreement with the previously reported ages.

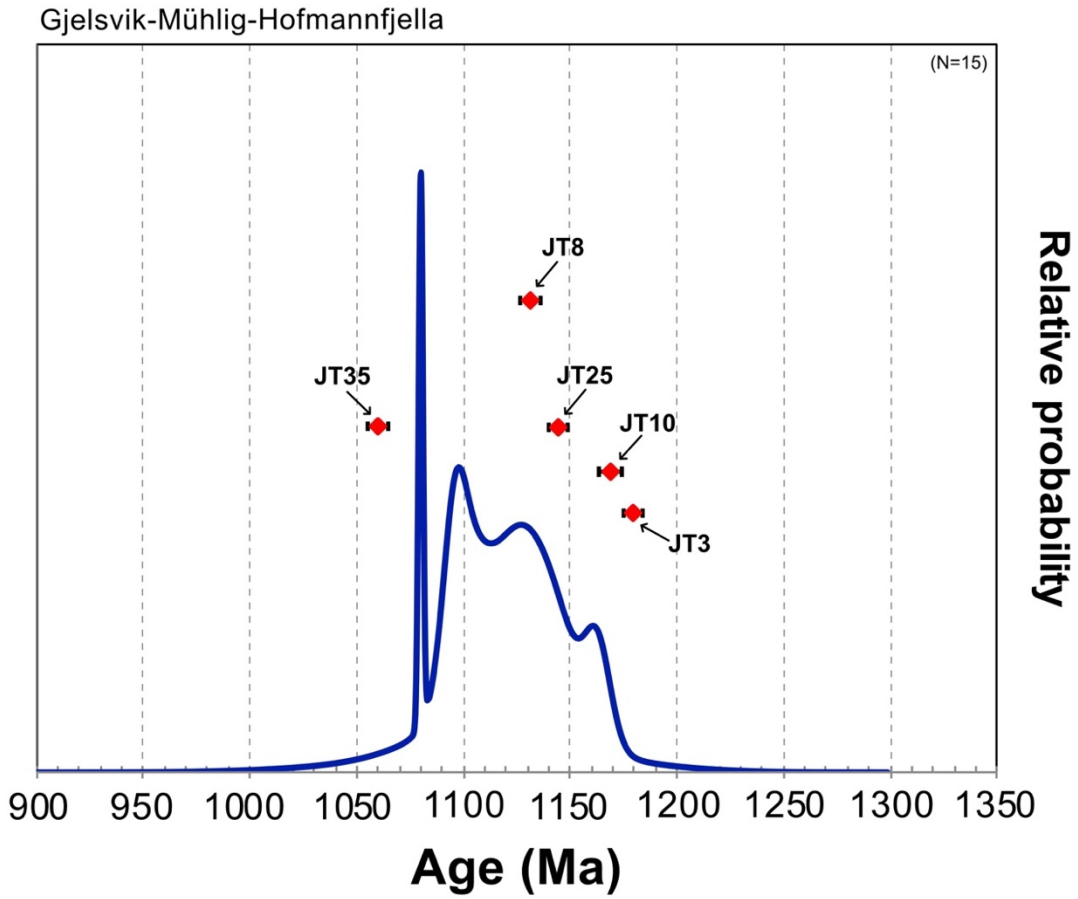

Figure 6.1: Summary of U–Pb zircon data constrained for Grenville–age magmatism within the Gjelsvik–Mühlig–Hofmannfjella together with new Grenville–ages obtained from this study. The ages presented in this study are plotted with their corresponding error bar. "N" represents the number of ages reflecting the curve. The U–Pb zircon ages are after Paulsson and Austrheim (2003), Jacobs et al. (2003b), Jacobs et al. (2003a), Bisnath et al. (2006), Jacobs et al. (2008a) and Baba et al. (2015).

6.3 Grenville–age magmatism in the Maud Belt

The Maud Belt stretches from Heimefrontfjella in the west to the Orvin–Wohlthat Mountains in the east, where the study area (Gjelsvikfjella) is located in the west–central part of the belt. The U–Pb zircon data in this study, together with the previously detected ages of Gjelsvikfjella–Mühlig–Hofmannfjella, is consistent with other Grenville–ages obtained from nunataks in east–central and western Dronning Maud Land (Fig. 6.2).

The oldest ages, ca. 1170 Ma and 1179 Ma (JT3 and JT10), revealed from this study coincide with the basement rocks in Heimefrontfjella and Kirwanveggen, which crops out in western Dronning Maud Land. Here, similar U–Pb zircon igneous ages from felsic metavolcanic rocks

include 1173±8 Ma (Arndt et al., 1991), 1171±25 Ma (Jacobs et al., 2003c), 1161±6 Ma (Bauer et al., 2003b), and 1157±10 Ma (Harris, 1999). Grenville–age magmatic activity at ca. 1170 Ma or older has not been commonly detected within the Orvin–Wohlthat Mountains (eastern DML). The oldest U–Pb zircon age reported here comes from a mafic gneiss dated at 1152±7 Ma (Wang et al., 2020).

The protolith age of sample JT8 (1131±9 Ma) and JT25 (1145±6 Ma) is comparable with a significant amount of earlier reported U–Pb zircon ages both east and west of the study area. Several felsic gneisses and orthogneisses from the Orvin–Wohlthat Mountains show magmatism around 1140–1130 Ma, and some of the detected ages overlap with the age of JT25 (Jacobs et al., 1998; Wang et al., 2020). U–Pb zircon ages reported from felsic rocks in H.U. Sverdrupfjella, Kirwanveggen, and Heimefrontfjella also indicate an age peak around 1140–1130 Ma (Arndt et al., 1991; Harris et al., 1995; Jackson, 1999; Board et al., 2005; Bauer et al., 2003b; Jacobs et al., 2003c; Grantham et al., 2011). Sample JT8 and JT25 are strongly consistent with the existing dataset, as a large proportion of the ages from the Maud Belt fall within ca. 1140–1130 Ma.

The ca. 1061 Ma (JT35) age obtained from this study was slightly younger than the previously detected ages within the study area. However, when comparing this age to the remaining Maud mountains, there is an age peak between ca. 1090–1050 Ma. In the west, earlier studies within the mountains record younger Grenville–age magmatism between ca. 1090–1030 Ma, in addition to ages of ca. 990 Ma reported in Kirwanveggen (e.g. Jackson, 1999; Jacobs et al., 2003c). The ca. 1061 Ma age is indistinguishable from earlier U–Pb zircon ages dating igneous activity at ca. 1060 within Heimefrontfjella, constrained from several rocks by zircon cores and upper intercept ages (Arndt et al., 1991).

To the east, in the Orvin–Wohlthat Mountains, the existing data show almost continuous magmatism from ca. 1160 Ma to 1080 Ma. The youngest Grenville–ages reported are from orthogneisses and felsic gneisses with ages at 1073±9 Ma, 1076±14 Ma (Jacobs et al., 1998), and 1079±8 Ma (Wang et al., 2020). The overall geochronological data so far compiled from the Maud Belt indicates that younger igneous Mesoproterozoic rocks are commonly found westwards.

Inherited zircons are not common in this study. However, one oscillatory zoned zircon core that was analysed from sample JT10 represents a potential inherited zircon (~1240 Ma). This age is nearly concordant and has a significantly older age than the remaining analysed zircon cores. Similar Mesoproterozoic and older Paleoproterozoic inherited and detrital zircons, although uncommon, have been discovered in e.g. Heimefrontfjella (~1200-2000 Ma, Arndt et al., 1991; up to ~2.9 Ga, Ksienzyk and Jacobs, 2015), Gjelsvikfjella (~1200 Ma, Bisnath et al., 2006), Mühlig–Hofmannfjella (up to ~1800 Ma, Baba et al., 2015), and the Orvin–Wohlthat Mountains (~1200-1700 Ma, Wang et al., 2020). The occurrence of Meso–Paleoproterozoic inherited zircons of older Mesoproterozoic ages and detrital zircons of Paleoproterozoic ages indicates the involvement of older crust during the formation of the Maud arc, most likely derived from the Proto–Kalahari Craton. In addition, detrital zircons from volcano–sedimentary rocks of Ritscherflya Supergroup within the Grunehogna Craton (bordering the Maud Belt) show Paleoproterozoic to Archean ages, which have been interpreted to be derived from the basements of the Kalahari–Grunehogna Craton along its eastern margin at the Maud Belt side (Marschall et al., 2013). The Paleoproterozoic and Archean zircons usually occurred as cores surrounded by oscillatory zoned rims that reveal a dominant age peak at ca. 1130 Ma. This age was interpreted as the sedimentation age, which is consistent with the peak of magmatic activities within the Maud Belt, and thus the Ritscherflya Supergroup rocks represent the erosional remnants from an active continental Maud arc that accumulated in a back–arc basin. The detrital zircons deposited here, therefore, could provide information on the crustal composition and evolution in the Maud Belt and highlight the importance of the older crustal component during the formation of Grenville–age Maud crust. As new data is complemented for the Maud Belt, such as old inherited and detrital zircons, and Hf–O isotopic compositions, it indicates an increased influence of crustal components than previously recognized. These findings argue that the Maud Belt would have developed upon the pre–existing crust of the eastern margin of the Proto–Kalahari Craton in a continental arc setting rather than as juvenile island arcs which accreted onto the Proto–Kalahari Craton (e.g. Grosch et al., 2007; Wang et al., 2020).

To summarize, the Maud Belt forms a continuous ca. 1100 Ma orogenic belt from western to eastern Dronning Maud Land. The U–Pb zircon ages presented in this study are strongly correlated to the previously published U–Pb zircon data within the Jutulsessen nunatak and the adjacent nunataks of Gjelsvikfjella–Mühlig–Hofmannfjella, as well as the Grenville–age magmatism reported in the eastern (Orvin–Wohlthat Mountains) and western (H.U.

Sverdrupfjella, Kirwanveggen, and Heimefrontfjella) Dronning Maud Land. Therefore, the crystallization age obtained from five felsic gneisses presented in this study thus confirm Grenville–age magmatism within the Maud Belt and supplement with reliable ages to the limited dataset. The four oldest ages, between ca. 1179–1131 Ma, are probably formed by continental arc magmatism at the eastern margin of Proto–Kalahari supported by their granodioritic compositions and evidence of inheritance. The ca. 1061 Ma age probably belongs to the subsequent magmatic period where rocks between ca. 1090–1050 Ma intruded the volcanic basement rocks.

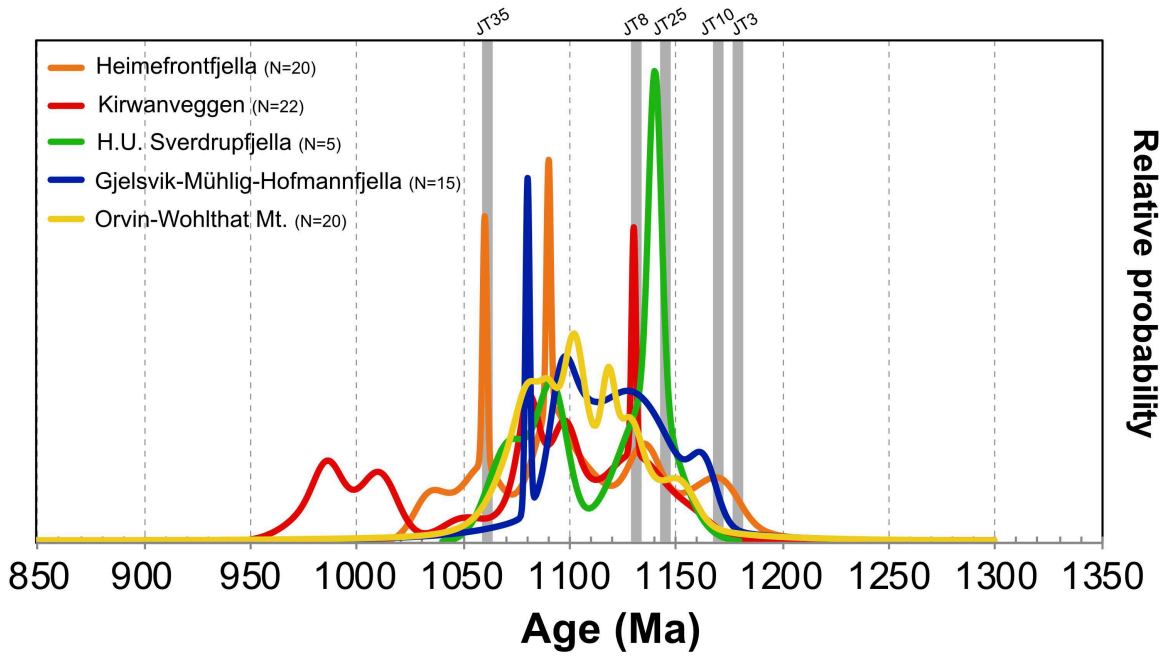

Figure 6.2: Summary of the existing igneous U–Pb zircon ages of the Grenville–age basement rocks within the Maud Belt, Dronning Maud Land. "N" represents the number of ages reflecting the curve. The ages obtained from this study are marked as grey bars (note that their age error is not included, and the bars represent the approximate age. Their age error can be found in Fig. 5.15. The U–Pb zircon ages revealed by this study coincide with the previously dated Grenville–age magmatic activity throughout the Maud Belt. The geochronological data are from the Heimefrontfjella (Arndt et al., 1991; Bauer et al., 2003a; Bauer et al., 2003b; Jacobs et al., 2003c), Kirwanveggen (Jackson, 1999; Harris et al., 1995; Harris, 1999), H.U. Sverdrupfjella (Board et al., 2005; Grantham et al., 2011; Hokada et al., 2019), Gjelsvik–Mühlig–Hofmannfjella (Paulsson and Austrheim, 2003; Jacobs et al., 2003a; Jacobs et al., 2003b; Bisnath et al., 2006; Jacobs et al., 2008a; Baba et al., 2015), and the Orvin–Wohlthat Mountains (Jacobs et al., 1998; Wang et al., 2020).

6.4 Indications of older Mesoproterozoic metamorphism

The first major metamorphic event affecting the Maud Belt is reported from zircon rim overgrowths from various Grenville–age basement rocks, mainly between 1090–1030 Ma. The U–Pb dataset for the samples herein does not show any evidence of this metamorphic event. However, similar findings are reported from earlier studies conducted in Gjelsvikfjella, except for a few gneisses investigated by Bisnath et al. (2006) dated at 1090–1070 Ma.

One zircon from sample JT10 indicates a metamorphic rim age of 1128±5 Ma. The rim is CL–dark and structureless with a moderate Th/U ratio of 0.3. The age is slightly reversely discordance and is only supported by this single analysis. The age is suspicious as no similar metamorphic age has been recorded in previous studies. However, as discussed in the sections above, the Maud Belt experienced a peak in magmatic activity around 1140–1130 Ma and this peak is also prominent in Gjelsvikfjella (study area). Thus, the metamorphic age could be a result of metamorphism related to the emplacement of igneous rocks. However, this age is not highly reliable as it is only supported by a single zircon analysis.

Sample JT10 also indicates metamorphism prior to the constrained Mesoproterozoic metamorphic event related to the collision of the Proto–Kalahari Craton during the Rodinia assembly. Two zircon rims yield a concordant age of 1105±8 Ma. The rims show low Th/U ratios of 0.09 and 0.1, indicating a metamorphic origin. U–Pb metamorphic zircon overgrowths of ca. 1100 Ma are rarely detected within the Maud Belt. However, a metaquartzite from Vardeklettane, Heimefrontfjella, is suggested to record granulite–facies metamorphism at 1104±5 Ma (Arndt et al., 1991). In addition, a metamorphic age of 1095±14 Ma is obtained by zircon rims from an adjacent area, Sivorgfjella (Heimefrontfjella) (Jacobs et al., 2003c). Furthermore, a magmatic pulse overlapping the ca 1105 Ma metamorphism is commonly reported within the Maud mountains, e.g. in Heimefrontfjella (1107±11 Ma, 1098±11 Ma), Kirwanveggen (1103±13 Ma), Gjelsvikfjella (1104±8 Ma), Orvinfjella (1107±8 Ma) (Jackson, 1999; Jacobs et al., 2003c; Bisnath et al., 2006; Wang et al., 2020).

The well–constrained magmatic activity around 1100 Ma within the Maud Belt and the poorly defined ca. 1105 Ma metamorphic event is intriguingly comparable with a large–scale intra–plate magmatic event (~1110 Ma) recognized across the Proto–Kalahari Craton (Fig. 6.3). This magmatic event was first detected from mafic sill intrusions representing the Umkondo LIP in Africa. However, later work discovered coeval intrusions throughout the Proto–Kalahari Craton, such as the Borgmassivet Suits (~1107 Ma) within the Grunehogna Province (western Dronning Maud Land) (reviewed by Hanson et al., 2006). This major anorogenic magmatic event was rapidly emplaced between ca. 1112–1106 Ma as a result of a plume center beneath the Kalahari Craton during the Rodinia assembly (Hanson et al., 1998; Hanson et al., 2004). Some authors (e.g. Grosch et al., 2007), suggest the older metamorphic imprints detected within the Maud Belt, such as ca. 1104 Ma (Arndt et al., 1991) and ca. 1095 Ma (Jacobs et al., 2003c) (comparable with this study), to possibly date this large–scale thermal Umkondo–Borgmassivet magmatic event. Furthermore, Grosch et al. (2007) presented geochemical data examined on Mesoproterozoic amphibolites from the western part of the Maud Belt (H.U. Sverdrupfjella–Gjelsvikfjella). Their Sm–Nd model age and εNd value revealed a similar signature as the Borgmassivet Sills, implying a possible relationship to the Umkondo–Borgmassivet thermal event. Another thermal imprint of the Umkondo–Borgmassivet Suits could be reflected by leucosome development in Kirwanveggen, dated at 1098±5 Ma (Harris, 1999).

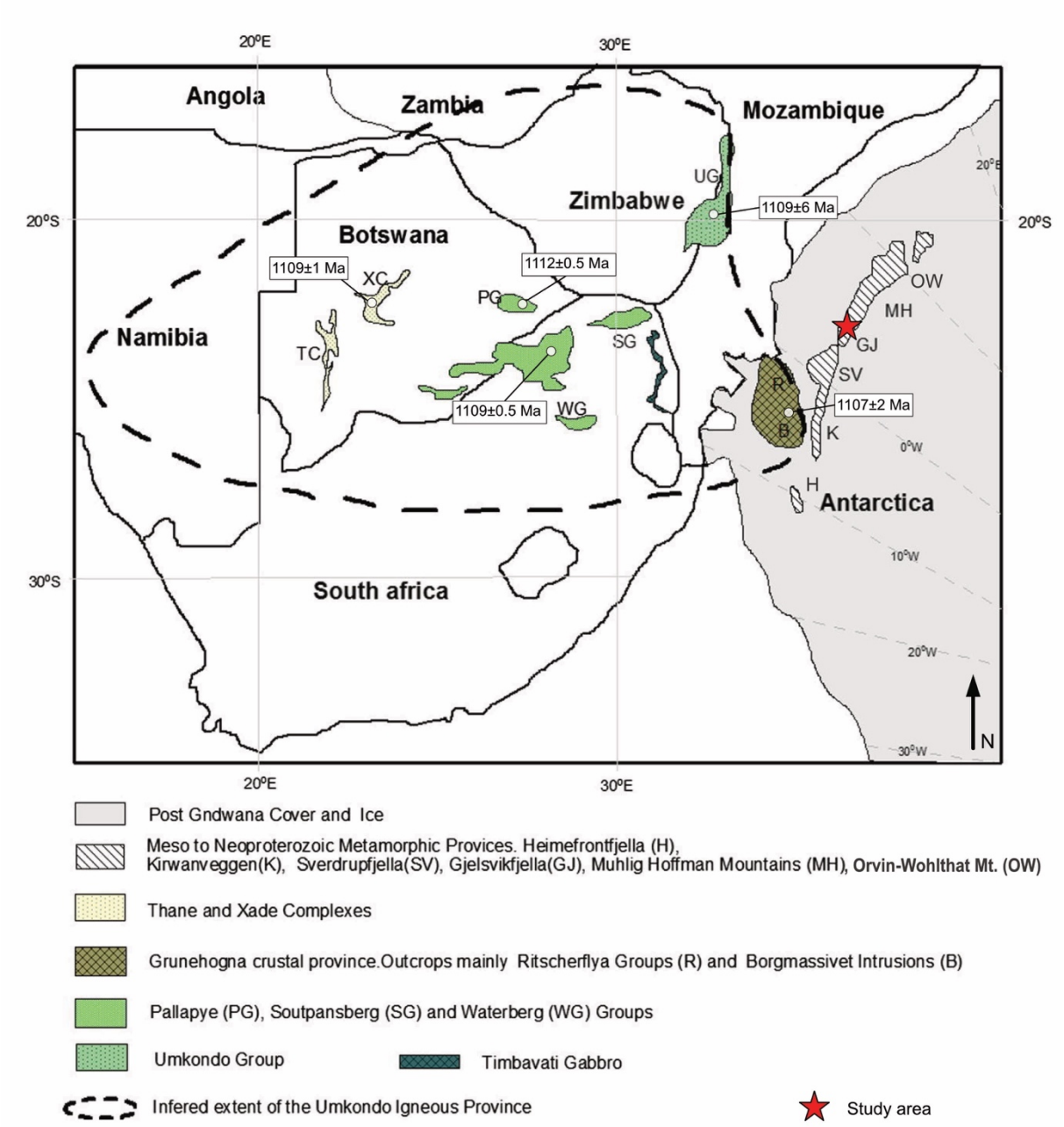

Figure 6.3: Illustration of the extend of the Umkondo Igneous Province within southern Africa and Antarctica. The generalized map shows the location for some of the intrusions that have been correlated with Umkondo magmatism. The U–Pb baddeleyite and zircon ages presented are representative igneous intrusion ages, from the work of Hanson et al. (2004) and Hanson et al. (2006), inferred to be emplaced during the intraplate magmatic event within the Kalahari Craton (~1110 Ma). Modified from Moabi et al. (2015) (after Hanson et al., 2004).

Other studies opine the short–lived magmatism to be a consequence of subduction–related magmatism and asthenospheric upwelling, resulting in mafic intrusions within the margin of the Grunehogna Craton, such as the Borgmassivet intrusions and volcanic activity in the Maud arc, synchronous to the Umkondo LIP magmatism (Grosch et al., 2015; Hokada et al., 2019). Wang et al. (2020) reported more juvenile Hf isotope compositions for the rocks crystallizing at ca. 1100 Ma in the Orvin–Wohlthat Mountains compared to the older dated rocks. These

findings may reflect a tectonic switching of the inboard subduction underneath the eastern margin of the Proto–Kalahari Craton. They infer the subduction to transform from advancing to retreating subduction–process, generating a significant magmatic pulse around 1100 Ma. The widespread ca. 1100 Ma magmatic activity within the Maud arc could then explain the older recorded metamorphic ages, such as the ca. 1105 Ma metamorphic age detected in this study, as well as the ca. 1098 Ma leucosome development reported in Kirwanveggen (Harris, 1999). Following, the Maud Belt was affected by a major metamorphic event and granitic magmatism around 1090–1030 Ma.

To conclude, most of the Grenville–age rocks within the Maud arc were emplaced through several episodes of magmatic activity, with the most prominent pulses peaking at ca 1140–1130 Ma, 1100 Ma, and 1090–1050 Ma (Fig. 6.2). Sample JT10 records two Mesoproterozoic metamorphic imprints at ca. 1128 Ma and ca. 1105 Ma. These ages indicate that some parts of the mountains underwent metamorphism prior to the so far major metamorphic event around 1090–1030 Ma. There are probably several episodes of metamorphism related to increased magmatic activity within the Maud Belt. The metamorphic ages presented in this study are coeval with magmatic pulses and could thus represent thermal imprints related to the igneous activity in the area. However, JT10 is a complex sample with a high number of discordant analyses. Further, the metamorphic overprints are constrained from a very limited number of rims overgrowths. This makes the metamorphic age data less reliable and needs to be interpreted with care. Further work is required to verify if these magmatic pulses triggered thermal imprints within some of the Mesoproterozoic basement rocks of the Maud Belt.

6.5 Evidence of late Neoproterozoic–early Paleozoic metamorphism

In late Neoproterozoic–early Paleozoic times, an extensive orogen, the East African–Antarctic Orogen (EAAO), was formed when various parts of West and East Gondwana collided (ca. 550) (Stern, 1994; Jacobs and Thomas, 2004). The Pan–African orogeny formed a long–lived orogenic plateau lasting for more than 150 Ma. During this time, the Mesoproterozoic basement of the Maud Belt experienced high–grade reworking. The Pan–African event in Dronning Maud Land involved two main metamorphic pulses revealed by zircon rim overgrowths at ca. 580–550 Ma and 530–500 Ma (Jacobs et al., 1998; Jacobs et al., 2003a; Bisnath and Frimmel, 2005; Jacobs et al., 2008a). Evidence of earlier metamorphism, ca. 650–600 Ma, is reported from the Schirmacher Oasis region (an isolated landmass of central DML, close to the coastline) as well as the eastern part of the main mountains of central Dronning Maud Land (Baba et al., 2010; Jacobs et al., 2020). Recent work has further detected igneous activity at ca. 600 Ma in the Schirmacher Oasis region (Jacobs et al., 2020). Similar ages have also been reported within the Orvin–Wohlthat Mountains by charnockite and anorthosite intrusions (Jacobs et al., 1998). These ca. 600 Ma metamorphic and magmatic ages are suggested to predate the main collisional event in central Dronning Maud Land (~550–500 Ma), possibly related to a back–arc extensional setting owing to a retreating subduction zone (Baba et al., 2010; Jacobs et al., 2020). Of the two main metamorphic pulses, the former pulse (~580–550 Ma) is suggested to represent the main collisional phase between the Kalahari Craton and East Antarctic Craton (part of East Gondwana), resulting in a pervasive high–grade reworking of the Grenville–age basement rocks in Dronning Maud Land (Jacobs et al., 1998). The latter metamorphic pulse (~530–500 Ma) is interpreted to represent delamination of the orogenic root causing partial melting of the bedrocks, followed by orogenic collapse generating large volumes of post–tectonic intrusions between ca 540–480 Ma (Jacobs et al., 2008a).

Two of the analysed samples (JT8 and JT35) with Grenville–age magmatic ages were later affected by Pan–African metamorphism. The metamorphic ages obtained from these two samples are 549±33 Ma and 496±9 Ma, respectively. Comparable late Neoproterozoic–early Paleozoic metamorphic ages have previously been reported within in the Maud Belt (Jacobs et al., 1998; Jacobs et al., 2003c; Jacobs et al., 2003a; Paulsson and Austrheim, 2003; Board et al., 2005; Bisnath et al., 2006; Baba et al., 2015; Wang et al., 2020).

Sample JT8, a granodioritic gneiss, is most likely related to the former metamorphic pulse (~580–550 Ma). The ca. 549 Ma age is detected from rim overgrowths with Th/U ratios <0.1,

typical of a metamorphic origin. Similar metamorphic ages have been widely reported in central Dronning Maud Land, as well as western DML by previous studies. For example, Bisnath et al. (2006) reported that Mesoproterozoic rocks from Gjelsvikfjella experienced Pan–African overprint at ca. 530 Ma. Just east of the study area, in Mühlig–Hofmannfjella, Jacobs et al. (2003a) reported Mesoproterozoic zircon cores characterized by metamorphic rim growth at 560–550 Ma and syn–tectonic leucosomes of ca. 560 Ma, which have been strongly deformed after their emplacement pointing towards high–grade metamorphic conditions. A tectono–thermal overprint is also recognized in the eastern part of the Maud Belt by Jacobs et al. (1998) constrained from zircon rim overgrowths between ca. 580–520 Ma. The U–Pb zircon metamorphic ages were obtained from both Mesoproterozoic felsic gneisses and orthogneisses and from ca. 600 Ma anorthosite and charnockite intrusions. This study further proposed the metamorphic rim ages between ca. 570–550 Ma to reflect the collisional phase. Within the same area, a similar age pattern has been reported by Wang et al. (2020), where several Mesoproterozoic felsic gneisses gave metamorphic rim overgrowths around ca. 550 Ma. In western Dronning Maud Land, a concordia age of 540±6 Ma was obtained from a paragneiss from H.U. Sverdrupfjella and was interpreted to reflect the timing of a metamorphic event (Board et al., 2005). Further south–west, a Mesoproterozoic felsic gneiss from Heimefrontfjella gave a metamorphic overgrowth age of 555±8 Ma (Jacobs et al., 2003c), interpreted as reflecting the assemblage of Gondwana. Therefore, this period is thus considered to have marked the extensive high–grade metamorphism in this region and to be related to the collisional assembly of East and West Gondwana.

The second sample (JT35), a migmatite gneiss, as previously mentioned, gave a concordant age of 1061±9 Ma for the oldest zircon cores and thus interpreted as the crystallization age, whereas a lower intercept age of 496±9 Ma was defined by analyses with ancient Pb loss. This age is consistent with the younger metamorphic pulse (~530–500 Ma) affecting the Maud Belt and the lower intercept age probably dates the migmatization of the rock, supported by field observations. The migmatization is considered to be a result of partial melting of the basement rock during delamination and isothermal decompression. A similar interpretation is suggested for the homogenous migmatite from Jutulhogget examined by Paulsson and Austrheim (2003). The migmatite revealed a protolith age of 1163±6 Ma and later experienced migmatization at 504±6 Ma, contemporaneous to the migmatitic gneiss of this study. Furthermore, just south of Jutulsessen, at Terningskarvet, Bisnath et al. (2006) investigated a migmatitic gneiss, which gave a crystallization age of 1143±41 Ma with metamorphic zircon overgrowths at 505±10 Ma

dating the migmatization of the rock. Similar tectono–thermal overprint ages at ca. 500 Ma have been reported both east and west of Gjelsvikfjella, e.g. in Heimefrontfjella (Jacobs et al., 2003c), H.U. Sverdrupfjella (Board et al., 2005), and the Orvin–Wohlthat Mountains (Wang et al., 2020).

6.6 Late Neoproterozoic–early Paleozoic magmatism

One of the investigated samples (JT27, granitic gneiss) in this study gave a concordant age of 497±4 Ma, which is interpreted as the emplacement age of the granitic protolith. Based on existing geochronological data, this age is associated with the late stage of the orogenic event affecting the region. As previously addressed, the latter metamorphic pulse (~530–500 Ma) was accompanied by large–scale post–tectonic A_2–type granitoids which intruded the metamorphic complex around 540–480 Ma (Jacobs et al., 1998; Roland, 2002; Paulsson and Austrheim, 2003; Jacobs et al., 2003a; Board et al., 2005; Bisnath et al., 2006; Jacobs et al., 2008a). The granitoids typically comprise of granitic, syenitic, charnockitic, gabbroic, or monzodioritic compositions. These voluminous granitoids are proposed to be a consequence of lithospheric delamination associated with extensional collapse of the EAAO (Jacobs et al., 2008a). The ca. 497 Ma age obtained from this study could represent a granitic post–tectonic intrusion resulting from renewed crustal thinning during the orogenic collapse. The age further agrees with previous dated post–tectonic intrusions within the Maud Belt, e.g. the emplacement of a granite (499±4 Ma) and charnockite (501±7 Ma) from Wolhthatmassivet (Jacobs et al., 2008a) and the Stabben syenite (500±8 Ma) from Jutulsessen (Paulsson and Austrheim, 2003). However, the Pan–African age obtained from this study will not be further analysed as this crystallization age is beyond this paper's scope.

7 Conclusion

Based on new U–Pb geochronological data obtained from six granitoids in this study, I propose the following conclusion for Jutulsessen, Gjelsvikfjella:

Mesoproterozoic evidence:

- Five of the investigated felsic meta–igneous samples constrain Grenville–age magmatism between ca. 1179 to 1061 Ma. These ages are consistent with the known Grenville–age magmatism for the basement rocks of Maud Belt.
- Late Mesoproterozoic metamorphism has been detected at ca. 1128 Ma and 1105 Ma from zircon rim overgrowths. This indicates metamorphism prior to the major metamorphic event between 1090–1030 Ma. Based on the magmatic activity recorded in the Maud Belt, these ages are inferred to reflect thermal imprints related to igneous emplacements during magmatic pulses.
- No igneous or metamorphic activity is recorded between ca. 1061 Ma and ca. 549 Ma within this study.
- One of the samples, which obtained an igneous Grenville–age, also records a potential inherited zircon at ca. 1240 Ma. Evidence of older inherited zircons supports newer publications suggesting a continental arc setting of the Maud Belt rather than a juvenile island arc setting.
- The petrological study revealed an average granodioritic composition, evident with crustal growth in a volcanic arc setting. The rocks are interpreted to have undergone at least upper amphibole–facies metamorphic conditions.

Pan–African evidence:

- The Mesoproterozoic basement show evidence of Pan–African tectono–thermal overprinting between ca. 549–496 Ma. These ages are reflecting the final amalgamation of various components of West and East Gondwana and processes related to the subsequent extensional orogenic collapse (EAAO).
- One sample reports a crystallization age of ca. 497 Ma. This sample is inferred to reflect a granitic post–tectonic intrusion during the Pan–African event.

8 References

Ahrens, L. 1955. The convergent lead ages of the oldest monazites and uraninites (Rhodesia, Manitoba, Madagascar, and Transvaal). *Geochimica et Cosmochimica Acta,* v. 7**,** p. 294-300.

Andersen, T., Elburg, M. A. & Magwaza, B. N. 2019. Sources of bias in detrital zircon geochronology: Discordance, concealed lead loss and common lead correction. *Earth-Science Reviews,* v. 197**,** p. 102899.

Arima, M., Tani, K., Kawate, S. & Johnston, S. T. 2001. Geochemical characteristics and tectonic setting of metamorphosed rocks in the Tugela terrane, Natal belt, South Africa. *Memoirs of National Institute of Polar Research,* Special Issue, 55**,** p. 1-39.

Arndt, N., Todt, W., Chauvel, C., Tapfer, M. & Weber, K. 1991. U-Pb zircon age and Nd isotopic composition of granitoids, charnockites and supracrustal rocks from Heimefrontfjella, Antarctica. *Geologische Rundschau,* v. 80**,** p. 759-777.

Baba, S., Hokada, T., Kaiden, H., Dunkley, D. J., Owada, M. & Shiraishi, K. 2010. SHRIMP zircon U-Pb dating of sapphirine-bearing granulite and biotite-hornblende gneiss in the Schirmacher Hills, east Antarctica: implications for Neoproterozoic ultrahigh-temperature metamorphism predating the assembly of Gondwana. *The Journal of Geology,* v. 118**,** p. 621-639.

Baba, S., Horie, K., Hokada, T., Owada, M., Adachi, T. & Shiraishi, K. 2015. Multiple collisions in the East African–Antarctica Orogen: constraints from timing of metamorphism in the Filchnerfjella and Hochlinfjellet terranes in central Dronning Maud Land. *The Journal of Geology,* v. 123**,** p. 55-77.

Barker, A. J. 2013. *Introduction to metamorphic textures and microstructures,* 2nd Edition, Routledge.

Bauer, W., Fielitz, W., Jacobs, J., Fanning, C. & Spaeth, G. 2003a. Mafic dykes from Heimefrontfjella and implications for the post-Grenvillian to pre-Pan-African geological evolution of western Dronning Maud Land, Antarctica. *Antarctic Science,* v. 15**,** p. 379-391.

Bauer, W., Jacobs, J., Fanning, C. & Schmidt, R. 2003b. Late Mesoproterozoic arc and back-arc volcanism in the Heimefrontfjella (East Antarctica) and implications for the palaeogeography at the southeastern margin of the Kaapvaal-Grunehogna Craton. *Gondwana Research,* v. 6**,** p. 449-465.

Bauer, W., Thomas, R. J. & Jacobs, J. 2003c. Proterozoic-Cambrian history of Dronning Maud Land in the context of Gondwana assembly. *Geological Society, London, Special Publications,* v. 206**,** p. 247-269.

Berhe, S. M. 1990. Ophiolites in Northeast and East Africa: implications for Proterozoic crustal growth. *Journal of the Geological Society,* v. 147**,** p. 41-57.

Best, M. G. 2002. *Igneous and Metamorphic Petrology. 2nd Edition,* New York: Wiley-Blackwell.

Bisnath, A., Frimmel, H., Armstrong, R. & Board, W. 2006. Tectono-thermal evolution of the Maud Belt: new SHRIMP U–Pb zircon data from Gjelsvikfjella, Dronning Maud land, East Antarctica. *Precambrian Research,* v. 150**,** p. 95-121.

Bisnath, A. & Frimmel, H. E. 2005. Metamorphic evolution of the Maud Belt: P–T–t path for high-grade gneisses in Gjelsvikfjella, Dronning Maud Land, East Antarctica. *Journal of African Earth Sciences,* v. 43**,** p. 505-524.

Board, W., Frimmel, H. & Armstrong, R. 2005. Pan-African tectonism in the western Maud Belt: P–T–t path for high-grade gneisses in the HU Sverdrupfjella, East Antarctica. *Journal of Petrology,* v. 46**,** p. 671-699.

Boekhout, F., Roberts, N. M., Gerdes, A. & Schaltegger, U. 2015. A Hf-isotope perspective on continent formation in the south Peruvian Andes. *Geological Society, London, Special Publications,* v. 389**,** p. 305-321.

Bohrmann, P. & Fritzsche, D. 1995. The Schirmacher Oasis, Queen Maud Land, East Antarctica, and its surroundings: . *Petermans Geograph Mitt Ergänzungsheft,* v. 289**,** p. 448.

Cawood, P. A., Hawkesworth, C. & Dhuime, B. 2012. Detrital zircon record and tectonic setting. *Geology,* v. 40**,** p. 875-878.

Cherniak, D. & Watson, E. 2001. Pb diffusion in zircon. *Chemical Geology,* v. 172**,** p. 5-24.

Cherniak, D. J. & Watson, E. B. 2003. Diffusion in zircon. *Reviews in mineralogy and geochemistry,* v. 53**,** p. 113-143.

Collins, W. 2002. Hot orogens, tectonic switching, and creation of continental crust. *Geology,* v. 30**,** p. 535-538.

Compston, W., Williams, I. & Meyer, C. 1984. U-Pb geochronology of zircons from lunar breccia 73217 using a sensitive high mass-resolution ion microprobe. *Journal of Geophysical Research: Solid Earth,* v. 89**,** p. 525-534.

Corfu, F., Hanchar, J. M., Hoskin, P. W. & Kinny, P. 2003. Atlas of zircon textures. *Reviews in mineralogy and geochemistry,* v. 53**,** p. 469-500.

Dalziel, I. W., Mosher, S. & Gahagan, L. M. 2000. Laurentia-Kalahari collision and the assembly of Rodinia. *The Journal of Geology,* v. 108**,** p. 499-513.

Dickin, A. P. 2018. *Radiogenic isotope geology,* 3rd ed., Cambridge, United Kingdom, Cambridge university press.

Elburg, M., Jacobs, J., Andersen, T., Clark, C., Läufer, A., Ruppel, A., Krohne, N. & Damaske, D. 2015. Early Neoproterozoic metagabbro-tonalite-trondhjemite of Sør Rondane (East Antarctica): Implications for supercontinent assembly. *Precambrian Research,* v. 259**,** p. 189-206.

Elburg, M. A., Andersen, T., Jacobs, J., Läufer, A., Ruppel, A., Krohne, N. & Damaske, D. 2016. One Hundred Fifty Million Years of Intrusive Activity in the Sør Rondane Mountains (East Antarctica): Implications for Gondwana Assembly. *The Journal of Geology,* v. 124**,** p. 1-26.

Engvik, A. K. & Elvevold, S. 2004. Pan-african extension and near-isothermal exhumation of a granulite facies terrain, Dronning Maud Land, Antarctica. *Geological Magazine,* v. 141**,** p. 1-12.

Engvik, A. K., Elvevold, S., Jacobs, J., Tveten, E., De Azevedo, S. & Njange, F. 2007. Pan-African granulites of central Dronning Maud Land and Mozambique: a comparison within the East-African-Antarctic orogen. Short Research Paper 065**,** p. 1-5.

Faure, G. & Mensing, T. M. 2005. *Isotopes: principles and applications*, 3rd ed, John Wiley & Sons.

Fitzsimons, I. C. W. 2003. Mix and match: using zircon geochronology to correlate late Mesoproterozoic metamorphic belts in Antarctica and Western Australia. *Geological Society of Australia Abstracts,* v. 72**,** p. 69.

Frimmel, H. E. 2004. Formation of a late Mesoproterozoic supercontinent: the South Africa-East Antarctica connection. In: Eriksson, P.G., Altermann, W., Nelson, D.R., Mueller, W.U., Catuneanu, O. (Eds.). *The Precambrium Earth: Tempos and Events. Developments in Precambrian Geology,* v. 12**,** p. 240-255.

Gaucher, C., Frei, R., Chemale, F., Frei, D., Bossi, J., Martínez, G., Chiglino, L. & Cernuschi, F. 2011. Mesoproterozoic evolution of the Río de la Plata Craton in Uruguay: at the heart of Rodinia? *International Journal of Earth Sciences,* v. 100**,** p. 273-288.

Golynsky, A. & Jacobs, J. 2001. Grenville-age versus pan-african magnetic anomaly imprints in Western Dronning Maud Land, East Antarctica. *The Journal of Geology,* v. 109**,** p. 136-142.

Grantham, G., Jackson, C., Moyes, A., Groenewald, P., Harris, P., Ferrar, G. & Krynauw, J. 1995. The tectonothermal evolution of the Kirwanveggen—HU Sverdrupfjella areas, Dronning Maud Land, Antarctica. *Precambrian Research,* v. 75**,** p. 209-229.

Grantham, G. H., Manhica, A. D. S. T., Armstrong, R. A., Kruger, F. J. & Loubser, M. 2011. New SHRIMP, Rb/Sr and Sm/Nd isotope and whole rock chemical data from central Mozambique and western Dronning Maud Land, Antarctica: Implications for the nature of the eastern margin of the Kalahari Craton and the amalgamation of Gondwana. *Journal of African Earth Sciences,* v. 59**,** p. 74-100.

Groenewald, P., Moyes, A., Grantham, G. & Krynauw, J. 1995. East Antarctic crustal evolution: geological constraints and modelling in western Dronning Maud Land. *Precambrian Research,* v. 75**,** p. 231-250.

Grosch, E. G., Bisnath, A., Frimmel, H. E. & Board, W. S. 2007. Geochemistry and tectonic setting of mafic rocks in western Dronning Maud Land, East Antarctica: implications for the geodynamic evolution of the Proterozoic Maud Belt. *Journal of the Geological Society,* v. 164**,** p. 465-475.

Grosch, E. G., Frimmel, H. E., Abu-Alam, T. & Košler, J. 2015. Metamorphic and age constraints on crustal reworking in the western HU Sverdrupfjella: implications for the evolution of western Dronning Maud Land, Antarctica. *Journal of the Geological Society,* v. 172**,** p. 499-518.

Grunow, A., Hanson, R. & Wilson, T. 1996. Were aspects of Pan-African deformation linked to Iapetus opening? *Geology,* v. 24**,** p. 1063-1066.

Hanson, R., Harmer, R., Blenkinsop, T. G., Bullen, D., Dalziel, I., Gose, W., Hall, R., Kampunzu, A., Key, R. & Mukwakwami, J. 2006. Mesoproterozoic intraplate magmatism in the Kalahari Craton: a review. *Journal of African Earth Sciences,* v. 46**,** p. 141-167.

Hanson, R. E., Crowley, J. L., Bowring, S. A., Ramezani, J., Gose, W. A., Dalziel, I. W., Pancake, J. A., Seidel, E. K., Blenkinsop, T. G. & Mukwakwami, J. 2004. Coeval large-scale magmatism in the Kalahari and Laurentian cratons during Rodinia assembly. *Science,* v. 304**,** p. 1126-1129.

Hanson, R. E., Martin, M. W., Bowring, S. A. & Munyanyiwa, H. 1998. U-Pb zircon age for the Umkondo dolerites, eastern Zimbabwe: 1.1 Ga large igneous province in southern Africa–East Antarctica and possible Rodinia correlations. *Geology,* v. 26**,** p. 1143-1146.

Harley, S. L. & Kelly, N. M. 2007. Zircon tiny but timely. *Elements,* v. 3**,** p. 13-18.

Harris, P. D. 1999. The geological evolution of Neumayerskarvet in the Northern Kirwanveggen, Western Dronning Maud Land, Antartica. *Unpublished Ph.D thesis,* Rand Afrikaans University, Johannesburg.

Harris, P. D., Moyes, A. B., Fanning, C. M. & Armstrong, R. A. 1995. Zircon Ion mircoscope results from the Maudheim high-grade gneiss terrane, western Dronning Maud Land, Antarctica. *Extended abstract, Centennial Geocongress,* Rand Afikaans University, Johannesburg.

Hiess, J., Condon, D. J., Mclean, N. & Noble, S. R. 2012. 238U/235U systematics in terrestrial uranium-bearing minerals. *Science,* v. 335**,** p. 1610-1614.

Hokada, T., Grantham, G. H., Arima, M., Saito, S., Shiraishi, K., Armstrong, R. A., Eglington, B., Misawa, K. & Kaiden, H. 2019. Stenian A-type granitoids in the Namaqua-Natal Belt, southern Africa, Maud Belt, Antarctica and Nampula Terrane, Mozambique: Rodinia and Gondwana amalgamation implications. *Geoscience Frontiers,* v. 10**,** p. 2265-2280.

Hoskin, P. W. & Schaltegger, U. 2003. The composition of zircon and igneous and metamorphic petrogenesis. *Reviews in mineralogy and geochemistry,* v. 53**,** p. 27-62.

Ireland, T. R. 2014. 15.21 - Ion Microscopes and Microscopes. *Treatise on Geochemistry,* v. 15**,** p. 385-409.

Ireland, T. R. & Williams, I. S. 2003. Considerations in zircon geochronology by SIMS. *Reviews in mineralogy and geochemistry,* v. 53**,** p. 215-241.

Jackson, C. 1999. Characterization of Mesoproterozoic to Palaeozoic crustal evolution of western Dronning Maud Land. Study 3: Deformational history and thermochronology of the central Kirwanveggen. *Unpublished report,* Council for Geoscience Open File Report: 1999-0135.

Jacobs, J., Bauer, W. & Fanning, C. 2003a. Late Neoproterozoic/Early Palaeozoic events in central Dronning Maud Land and significance for the southern extension of the East African Orogen into East Antarctica. *Precambrian Research,* v. 126**,** p. 27-53.

Jacobs, J., Bauer, W. & Fanning, C. M. 2003b. New age constraints for Grenville-age metamorphism in western central Dronning Maud Land (East Antarctica), and implications for the palaeogeography of Kalahari in Rodinia. *International Journal of Earth Sciences,* v. 92**,** p. 301-315.

Jacobs, J., Bauer, W., Spaeth, G., Thomas, R. & Weber, K. 1996. Litholog and structure of the Grenville-aged (≈ 1.1 Ga) basement of heimefrontfjella (East Antarctica). *Geologische Rundschau,* v. 85**,** p. 800-821.

Jacobs, J., Bauer, W., Weber, K., Spaeth, G. & Thomas, R. J. 2009. Geology of the Sivorg Terrane, Heimefrontfjella (East Antarctica), and new U-Pb Zircon provenance analyses of metasedimentary rocks. *Polarforschung,* v. 79**,** p. 11-19.

Jacobs, J., Bingen, B., Thomas, R. J., Bauer, W., Wingate, M. T. D. & Feitio, P. 2008a. Early Palaeozoic orogenic collapse and voluminous late-tectonic magmatism in Dronning Maud Land and Mozambique: insights into the partially delaminated orogenic root of the East African–Antarctic Orogen? *Geological Society, London, Special Publications,* v. 308**,** p. 69-90.

Jacobs, J., Elburg, M., Läufer, A., Kleinhanns, I. C., Henjes-Kunst, F., Estrada, S., Ruppel, A. S., Damaske, D., Montero, P. & Bea, F. 2015. Two distinct Late Mesoproterozoic/Early Neoproterozoic basement provinces in central/eastern Dronning Maud Land, East Antarctica: The missing link, 15–21°E. *Precambrian Research,* v. 265**,** p. 249-272.

Jacobs, J., Fanning, C. M. & Bauer, W. 2003c. Timing of Grenville-age vs. Pan-African medium-to high grade metamorphism in western Dronning Maud Land (East Antarctica) and significance for correlations in Rodinia and Gondwana. *Precambrian Research,* v. 125**,** p. 1-20.

Jacobs, J., Fanning, M. C., Henjes-Kunst, F., Olesch, M. & Paech, H.-J. 1998. Continuation of the Mozambique Belt into East Antarctica: Grenville-Age Metamorphism and Polyphase Pan-African High-Grade Events in Central Dronning Maud Land. *The Journal of Geology,* v. 106**,** p. 385-406.

Jacobs, J., Hansen, B. T., Henjes-Kunst, F., Thomas, R. J., Weber, K., Bauer, W., Armstrong, R. A. & Cornell, D. H. 1999. New Age Constraints on the Proterozoic/Lower Palaeozoic Evolution of Heimefrontfjella, East Antarctica, and Its Bearing on Rodinia/Gonwana. *Terra Antarctica Publication,* v. 6**,** p. 377-389.

Jacobs, J., Klemd, R., Fanning, C., Bauer, W. & Colombo, F. 2003d. Extensional collapse of the late Neoproterozoic-early Palaeozoic East African-Antarctic Orogen in central Dronning Maud Land, East Antarctica. *Geological Society, London, Special Publications,* v. 206**,** p. 271-287.

Jacobs, J., Mikhalsky, E., Henjes-Kunst, F., Läufer, A., Thomas, R. J., Elburg, M. A., Wang, C.-C., Estrada, S. & Skublov, G. 2020. Neoproterozoic geodynamic evolution of easternmost Kalahari: Constraints from U-Pb-Hf-O zircon, Sm-Nd isotope and geochemical data from the Schirmacher Oasis, East Antarctica. *Precambrian Research,* v. 342**,** p. 105553.

Jacobs, J., Pisarevsky, S., Thomas, R. J. & Becker, T. 2008b. The Kalahari Craton during the assembly and dispersal of Rodinia. *Precambrian Research,* v. 160**,** p. 142-158.

Jacobs, J. & Thomas, R. 1994. Oblique collision at about 1.1 Ga along the southern margin of the Kaapvaal continent, south-east Africa. *Geologische Rundschau,* v. 83**,** p. 322-333.

Jacobs, J., Thomas, R. & Weber, K. 1993. Accretion and indentation tectonics at the southern edge of the Kaapvaal craton during the Kibaran (Grenville) orogeny. *Geology,* v. 21**,** p. 203-206.

Jacobs, J. & Thomas, R. J. 2002. The Mozambique belt from an East Antarctic perspective. *Royal Society of New Zealand Bulletin,* v. 35**,** p. 3-18.

Jacobs, J. & Thomas, R. J. 2004. Himalayan-type indenter-escape tectonics model for the southern part of the late Neoproterozoic–early Paleozoic East African– Antarctic orogen. *Geology,* v. 32**,** p. 721-724.

Joshi, A., Pant, N. C. & Parimoo, M. L. 1991. Granites of Petermann Ranges, East Antarctica and implications of thir genesis. *Geological Society. India,* v. 38**,** p. 169-181.

Kamei, A., Horie, K., Owada, M., Yuhara, M., Nakano, N., Osanai, Y., Adachi, T., Hara, Y., Terao, M. & Teuchi, S. 2013. Late Proterozoic juvenile arc metatonalite and adakitic intrusions in the Sør Rondane Mountains, eastern Dronning Maud Land, Antarctica. *Precambrian Research,* v. 234**,** p. 47-62.

Kamenev, E. N., Kamenev, A. G. I. & Kovach, V. P. 1990. Zemlya Korolevy Maud. *In Ivanov, V. L and Kamenev, E. N., eds.,: Geologiya i Mineralnye Reursy Antarktidy: Moskva***,** p. 133-147.

Kriegsman, L. M. 1995. The Pan-African event in East Antarctica: a view from Sri Lanka and the Mozambique belt. *Precambrian Research,* v. 75**,** p. 263-277.

Kröner, A., Wan, Y., Liu, X. & Liu, D. 2014. Dating of zircon from high-grade rocks: Which is the most reliable method? *Geoscience Frontiers,* v. 5**,** p. 515-523.

Ksienzyk, A. K. & Jacobs, J. 2015. Western Australia-Kalahari (WAlahari) connection in Rodinia: Not supported by U/Pb detrital zircon data from the Maud Belt (East Antarctica) and the Northampton Complex (Western Australia). *Precambrian Research,* v. 259**,** p. 207-221.

Li, Z.-X., Bogdanova, S., Collins, A., Davidson, A., De Waele, B., Ernst, R., Fitzsimons, I., Fuck, R., Gladkochub, D. & Jacobs, J. 2008. Assembly, configuration, and break-up history of Rodinia: a synthesis. *Precambrian research,* v. 160**,** p. 179-210.

Loewy, S. L., Dalziel, I., Pisarevsky, S., Connelly, J., Tait, J., Hanson, R. & Bullen, D. 2011. Coats Land crustal block, East Antarctica: A tectonic tracer for Laurentia? *Geology,* v. 39**,** p. 859-862.

Ludwig, K. R. 1998. On the treatment of concordant uranium-lead ages. *Geochimica et Cosmochimica Acta,* v. 62**,** p. 665-676.

Ludwig, K. R. 2012. User's manual for Isoplot 3.75 - A geochronological toolkit for Microsoft Excel. *Berkeley Geochronology Center Special Publications,* v. 5**,** p. 75.

Marschall, H. R., Hawkesworth, C. J. & Leat, P. T. 2013. Mesoproterozoic subduction under the eastern edge of the Kalahari-Grunehogna Craton preceding Rodinia assembly: The Ritscherflya detrital zircon record, Ahlmannryggen (Dronning Maud Land, Antarctica). *Precambrian Research,* v. 236**,** p. 31-45.

Marschall, H. R., Hawkesworth, C. J., Storey, C. D., Dhuime, B., Leat, P. T., Meyer, H.-P. & Tamm-Buckle, S. 2010. The Annandagstoppane Granite, East Antarctica: evidence for Archaean intracrustal recycling in the Kaapvaal–Grunehogna Craton from zircon O and Hf isotopes. *Journal of Petrology,* v. 51**,** p. 2277-2301.

Mathieu, H. & Leonard, D. 1998. Use of post-ionisation techniques to complement SIMS analysis. A review with practical aspects. *High Temperature Materials and Processes,* v. 17**,** p. 29-44.

Mccourt, S., Armstrong, R., Grantham, G. H. & Thomas, R. J. 2006. Geology and evolution of the Natal belt, South Africa. *Journal of African Earth Sciences,* v. 46**,** p. 71-92.

Meert, J. G. 2003. A synopsis of events related to the assembly of eastern Gondwana. *Tectonophysics,* v. 362**,** p. 1-40.

Mendonidis, P., Thomas, R., Grantham, G. & Armstrong, R. 2015. Geochronology of emplacement and charnockite formation of the Margate Granite Suite, Natal Metamorphic Province, South Africa: implications for Natal-Maud belt correlations. *Precambrian Research,* v. 265**,** p. 189-202.

Merdith, A. S., Collins, A. S., Williams, S. E., Pisarevsky, S., Foden, J. D., Archibald, D. B., Blades, M. L., Alessio, B. L., Armistead, S. & Plavsa, D. 2017. A full-plate global reconstruction of the Neoproterozoic. *Gondwana Research,* v. 50**,** p. 84-134.

Mezger, K. & Krogstad, E. 1997. Interpretation of discordant U-Pb zircon ages: An evaluation. *Journal of metamorphic Geology,* v. 15**,** p. 127-140.

Mikhalsky, E., Beliatsky, B., Savva, E., Wetzel, H., Fedorov, L., Weiser, T.-I. & Hahne, K. 1997. Reconnaissance geochronologic data on polymetamorphic and igneous rocks of the Humboldt Mountains, central Queen Maud Land, East Antarctica. *The Antarctic region: Geological evolution and processes,* v. 45**,** p. 45-53.

Moores, E. M. 1991. Southwest US-East Antarctic (SWEAT) connection: a hypothesis. *Geology,* v. 19**,** p. 425-428.

Moyes, A. B. 1993. The age and origin of the Jutulsessen granitic gneiss, Gjelsvikfjella, Dronning Maud Land. . *S Afr J Antarctic Research,* v. 23**,** p. 25-32.

Muhongo, S. & Lenoir, J.-L. 1994. Pan-African granulite-facies metamorphism in the Mozambique Belt of Tanzania: U-Pb zircon geochronology. *Journal of the Geological Society,* v. 151**,** p. 343-347.

Ohta, Y., Tørudbakken, B. & Shiraishi, K. 1990. Geology of Gjelsvikfjella and western Mühlig-Hofmannfjella, Dronning Maud Land, East Antarctica. *Polar Research,* v. 8**,** p. 99-126.

Osanai, Y., Nogi, Y., Baba, S., Nakano, N., Adachi, T., Hokada, T., Toyoshima, T., Owada, M., Satish-Kumar, M. & Kamei, A. 2013. Geologic evolution of the Sør Rondane Mountains, East Antarctica: Collision tectonics proposed based on metamorphic processes and magnetic anomalies. *Precambrian Research,* v. 234**,** p. 8-29.

Owada, M., Baba, S., Laufer, A. L., Elvevold, S., Shiraishi, K. & Jacobs, J. 2003. Geology of eastern Muhlig-Hofmannfjella and Filchnerfjella in Dronning Maud Land, East Antarctica; a preliminary report of a Japan-Norway-Germany joint geological investigation. v. 16**,** p. 108-136.

Passchier, C. W. & Trouw, R. A. 2005. *Microtectonics*, 2nd ed. Springer Science & Business Media.

Paulsson, O. & Austrheim, H. 2003. A geochronological and geochemical study of rocks from Gjelsvikfjella, Dronning Maud Land, Antarctica—implications for Mesoproterozoic correlations and assembly of Gondwana. *Precambrian Research,* v. 125**,** p. 113-138.

Pisarevsky, S. A., Wingate, M. T. D., Powell, C. M., Johnson, S. & Evans, D. a. D. 2003. Models of Rodinia assembly and fragmentation. *Geological Society, London, Special Publications,* v. 206**,** p. 35-55.

Ravich, M. & Soloviev, D. 1966. Geologiya i petrologiya central'noj chasti gor zemli Korolevy Mod [Geology and petrology of the central part of the mountains of central Dronning Maud]. *Trudy Naucno-Isseldovatel'skogo Instituta Geologii Arktiki,* v. 141.

Ravich, M. G. & Kamenev, E. N. 1972. Kristallicheskii Fundament Antarkticheskoi Platformy. *Leningrad, Gidrometeoizdat***,** p. 658. (English ed., Crystalline basement of the Antarctic platform: Jerusalem, 1975, p. 547.

Riedel, S., Jacobs, J. & Jokat, W. 2013. Interpretation of new regional aeromagnetic data over Dronning Maud Land (East Antarctica). *Tectonophysics,* v. 585**,** p. 161-171.

Roland, N. 2002. Pan-African granitoids in central Dronning Maud Land, East Antarctica: Petrography, geochemistry, and plate tectonic setting. *Antarctica at the close of a millennium: Royal Society of New Zealand Bulletin,* v. 15**,** p. 85-91.

Roots, E. F. 1953. Preliminary note on the geology of western Dronning Maud Land. *Norsk Geologisk Tidsskrift,* v. 32**,** p. 17-33.

Schoene, B. 2014. *U-Th-Pb geochronology*, Princeton: Elsevier Ltd. p. 341-378.

Shiraishi, K., Dunkley, D., Hokada, T., Fanning, M., Kagami, H. & Hamamoto, T. 2008. Geochronological constraints on the Late Proterozoic to Cambrian crustal evolution of eastern Dronning Maud Land, East Antarctica: a synthesis of SHRIMP U–Pb age and Nd model age data. *Geological Society Special Publication,* v. 308**,** p. 21-67.

Shiraishi, K., Ellis, D., Hiroi, Y., Fanning, C., Motoyoshi, Y. & Nakai, Y. 1994. Cambrian orogenic belt in East Antarctica and Sri Lanka: implications for Gondwana assembly. *The Journal of Geology,* v. 102**,** p. 47-65.

Shrivastava, P. K., Dharwadkar, A., Asthana, R., Roy, S. K., Swain, A. K. & Beg, M. J. 2014. The sediment properties of glacial diamicts from the Jutulsessen area of Gjelsvikfjella, East Antarctica: A reflection of source materials and regional climate. *Polar Science,* v. 8**,** p. 264-282.

Stacey, J. T. & Kramers, J. 1975. Approximation of terrestrial lead isotope evolution by a two-stage model. *Earth and planetary science letters,* v. 26**,** p. 207-221.

Stern, R. J. 1994. Arc assembly and continental collision in the Neoproterozoic East African Orogen: implications for the consolidation of Gondwanaland. *Annual Review of Earth and Planetary Sciences,* v. 22**,** p. 319-351.

Stern, R. J., Johnson, P. R., Kröner, A. & Yibas, B. 2004. Neoproterozoic ophiolites of the Arabian-Nubian shield. *Developments in Precambrian Geology,* v. 13**,** p. 95-128.

Swanson-Hysell, N., Kilian, T. & Hanson, R. 2015. A new grand mean palaeomagnetic pole for the 1.11 Ga Umkondo large igneous province with implications for palaeogeography and the geomagnetic field. *Geophysical Journal International,* v. 203**,** p. 2237-2247.

Tera, F. & Wasserburg, G. J. 1972. U-Th-Pb systematics in three Apollo 14 basalts and the problem of initial Pb in lunar rocks. *Earth and Planetary Science Letters,* v. 14**,** p. 281-304.

Wang, C.-C., Jacobs, J., Elburg, M. A., Läufer, A., Thomas, R. J. & Elvevold, S. 2020. Grenville-age continental arc magmatism and crustal evolution in central Dronning Maud Land (East Antarctica): Zircon geochronological and HfO isotopic evidence. *Gondwana Research,* v. 82**,** p. 108-127.

Wendt, I. 1984. A three-dimensional U-Pb discordia plane to evaluate samples with common lead of unknown isotopic composition. *Chemical geology,* v. 46**,** p. 1-12.

Wetherill, G. W. 1956. Discordant uranium-lead ages, I. *Eos, Transactions American Geophysical Union,* v. 37**,** p. 320-326.

White, W. H. 2015. *Isotope Geochemistry*, 1st ed, John Wiley & Sons Inc, p. 77-99.

Whitehouse, M. J. & Kamber, B. S. 2005. Assigning dates to thin gneissic veins in high-grade metamorphic terranes: a cautionary tale from Akilia, southwest Greenland. *Journal of Petrology,* v. 46**,** p. 291-318.

Whitehouse, M. J., Kamber, B. S. & Moorbath, S. 1999. Age significance of U–Th–Pb zircon data from early Archaean rocks of west Greenland—a reassessment based on combined ion-microprobe and imaging studies. *Chemical geology,* v. 160**,** p. 201-224.

Online references

NORSK POLARINSTITUTT, 2020. Downloaded from (14.01.2020): *https://geologi.npolar.no/Html5Geo/index.html?viewer=Geology_DML*

Elvevold, S., Myhre, P. I., Engvik, A. K. & Jacobs, J. 2019. *Geological mapping of Norway's least explored mountains* [Online]. Framsenteret.no. Available: https://framsenteret.no/forum/2019/geological-mapping-of-norways-least-explored-mountains/ [Accessed 17.12.19].

9 Appendix

SIMS U–Pb zircon data

			Concentration (ppm)							Total (uncorrected) ratio				Radiogenic (corrected) ratio[5]				Calculated age ± σ (Ma)			
Sample ID	**Grain characteristics in CL[1]**	**Comment**	**U**	**Th**	**Pb**	**Th/U$_{meas}$[2]**	**^{206}Pb/^{204}Pb**	**f$_{206}$ (%)[3]**	**Disc.(%) conv.[4]**	**^{206}Pb/^{238}U**	**± σ (%)**	**^{207}Pb/^{206}Pb**	**± σ (%)**	**^{206}Pb/^{238}U**	**± σ (%)**	**^{207}Pb/^{206}Pb**	**± σ (%)**	**^{207}Pb/^{206}Pb**	**^{206}Pb/^{238}U**	**207-corr age[6]**	**Conc (%)[7]**
JT3, Granitic gneiss, Jutulhogget-W																					
N6144-JT3-14-1	CL-B, rim, UZ	Pb loss (recent)	755	551	175	0,73	7353	0,25	-9,4	5,5898	2,92	0,080384	0,50	5,6041	2,93	0,078458	0,65	1158 ± 13	1058 ± 29	1053 ± 30	91,4
N6144-JT3-13-1	CL-M, Z	rev. discordance	797	591	199	0,74	6571	0,28	4,5	5,2207	1,98	0,077657	0,92	5,2356	1,98	0,075493	1,31	1082 ± 26	1127 ± 21	1129 ± 22	104,1
N6144-JT3-12-1	CL-B, Z	Concordant	727	765	210	1,05	28409	0,07	4,5	4,8112	1,17	0,079380	0,33	4,8144	1,17	0,078882	0,34	1169 ± 7	1217 ± 13	>1200	104,1
N6144-JT3-11-1	CL-M, core, UZ	Pb loss (recent)	364	215	89	0,59	2038	0,92	-3,0	5,1476	3,03	0,085722	0,58	5,1953	3,06	0,078776	0,99	1166 ± 20	1135 ± 32	1133 ± 33	97,3
N6144-JT3-10-1	CL-M, Z	Concordant	588	340	148	0,58	298969	0,01	1,8	4,9601	1,37	0,078757	0,54	4,9604	1,37	0,078709	0,54	1165 ± 11	1184 ± 15	1185 ± 16	101,6
N6144-JT3-9-1	CL-M, Z	Concordant	560	283	143	0,51	198643	0,01	4,3	4,8129	1,38	0,079024	0,53	4,8133	1,38	0,078953	0,53	1170 ± 10	1217 ± 15	>1200	104
N6144-JT3-9-2	CL-D, rim, UZ	>10% rev. Discordance, highU	3797	225	876	0,06	25846	0,07	12,6	4,7348	1,46	0,077036	0,34	4,7383	1,46	0,076487	0,37	1108 ± 7	1234 ± 16	>1200	111,4
N6144-JT3-8-1	CL-M, Z	Concordant	548	330	139	0,60	118099	0,02	1,7	4,9509	1,85	0,078935	0,93	4,9517	1,85	0,078815	0,93	1167 ± 18	1186 ± 20	1187 ± 21	101,6
N6144-JT3-7-1	CL-M, Z	Concordant	611	435	160	0,71	109354	0,02	1,3	4,9348	1,19	0,079264	0,55	4,9357	1,19	0,079134	0,55	1175 ± 11	1189 ± 13	1190 ± 14	101,2
N6144-JT3-6-1	CL-M, Z	Concordant	570	446	153	0,78	148324	0,01	2,6	4,8745	1,21	0,079213	0,45	4,8751	1,21	0,079118	0,45	1175 ± 9	1203 ± 13	>1200	102,4
N6144-JT3-5-1	CL-M, Z	>5 % rev. discordance	520	271	134	0,52	95441	0,02	8,5	4,7670	2,01	0,077868	0,36	4,7679	2,01	0,077720	0,36	1140 ± 7	1227 ± 22	>1200	107,6
N6144-JT3-4-1	CL-M, Z	Concordant	923	761	246	0,82	173488	0,01	-0,1	4,9764	2,66	0,079443	0,81	4,9769	2,66	0,079362	0,81	1181 ± 16	1180 ± 29	1180 ± 30	99,9
N6144-JT3-3-1	CL-M, Z	Concordant	493	295	124	0,60	264244	0,01	0,8	5,0209	1,55	0,078646	0,44	5,0213	1,55	0,078592	0,45	1162 ± 9	1171 ± 17	1171 ± 18	100,8
N6144-JT3-2-1	CL-M, Z	Concordant	368	192	90	0,52	74437	0,03	2,3	5,0276	1,30	0,078124	0,88	5,0289	1,30	0,077934	0,89	1145 ± 18	1169 ± 14	1171 ± 15	102
N6144-JT3-1-1	CL-M, Z	Concordant	417	292	108	0,70	109322	0,02	0,9	4,9942	1,38	0,078928	0,48	4,9951	1,38	0,078798	0,48	1167 ± 10	1176 ± 15	1176 ± 16	100,8
JT8, Granodioritic gneiss, Death Valley																					
n6142-JT8-16-1	CL-D, UZ?	Pb loss, high common Pb	2816	984	297	0,35	727	2,57	-35,5	10,8533	2,19	0,086845	1,55	11,1398	2,24	0,067082	3,30	840 ± 69	554 ± 12	549 ± 12	65,9
n6142-JT8-15-1	CL-D, UZ?	Pb loss, highPb incl, highU	10545	1097	758	0,10	4948	0,38	-43,6	20,4569	3,06	0,061040	11,93	20,5346	3,07	0,058101	12,78	534 ± 283	301 ± 9	304 ± 10	56,4
n6142-JT8-14-1	CL-D, UZ?	>5% rev. discordance	3127	194	298	0,06	16954	0,11	7,1	11,3033	1,16	0,058363	0,44	11,3158	1,16	0,057504	0,46	511 ± 10	546 ± 6	547 ± 6	106,8
n6142-JT8-13-1	CL-D, UZ?	Pb loss, high common Pb	4283	373	272	0,09	339	5,52	-48,8	16,6059	9,64	0,104894	3,98	17,5769	10,20	0,062165	8,78	680 ± 188	357 ± 35	353 ± 34	98,9
n6142-JT8-12-1	CL-D, Z	Pb loss (recent)	1173	1177	258	1,00	4078	0,46	-13,5	5,8416	1,13	0,081961	0,59	5,8685	1,13	0,078489	0,65	1159 ± 13	1014 ± 11	1007 ± 11	87,5
n6142-JT8-11-1	CL-D, Z?	Pb loss, high common Pb	1991	1269	397	0,64	912	2,05	-10,5	6,1530	2,17	0,090110	1,55	6,2818	2,21	0,074507	4,05	1055 ± 82	952 ± 20	948 ± 20	90,2
n6142-JT8-10-1	CL-D, UZ	Pb loss	2586	518	471	0,20	4486	0,42	-14,4	6,0649	7,95	0,080535	1,23	6,0902	7,98	0,077374	1,63	1131 ± 32	980 ± 73	973 ± 75	99,3
n6142-JT8-9-1	CL-D, Z	Pb loss	911	625	210	0,69	28626	0,07	-4,5	5,5606	1,49	0,077120	0,63	5,5643	1,49	0,076624	0,64	1111 ± 13	1065 ± 15	1063 ± 15	95,9
n6142-JT8-8-2	CL-D, rim, UZ	wtd. av ^{206}Pb/^{207}Pb	2526	285	231	0,11	7789	0,24	5,9	11,6330	1,69	0,059140	0,29	11,6610	1,69	0,057271	0,43	502 ± 10	530 ± 9	531 ± 9	105,6
n6142-JT8-8-1	CL-D, Z	Pb loss	945	415	177	0,44	8999	0,21	-14,0	6,2097	1,78	0,077949	0,41	6,2227	1,78	0,076371	0,47	1105 ± 9	961 ± 16	954 ± 16	99,3
n6142-JT8-7-1	CL-D, Z	Pb loss	1286	1083	300	0,84	5223	0,36	-4,2	5,5474	1,21	0,079210	0,25	5,5673	1,21	0,076491	0,32	1108 ± 6	1065 ± 12	1063 ± 12	96,1
n6142-JT8-5-1	CL-D, rim, UZ	wtd. av ^{206}Pb/^{207}Pb	5949	57	572	0,01	84799	0,02	4,6	11,0199	1,07	0,058342	0,19	11,0223	1,07	0,058171	0,20	536 ± 4	560 ± 6	560 ± 6	104,5
n6142-JT8-6-1	CL-D, Z	Concordant	603	551	151	0,91	12279	0,15	-3,2	5,2763	1,65	0,079312	0,58	5,2844	1,65	0,078159	0,61	1151 ± 12	1117 ± 17	1115 ± 18	97
n6142-JT8-4-1	CL-D, Z	Concordant	1156	720	285	0,62	63289	0,03	3,0	5,1176	1,68	0,077143	0,40	5,1191	1,68	0,076918	0,42	1119 ± 8	1150 ± 18	1152 ± 19	102,8
n6142-JT8-3-1	CL-D, UZ, mix of core-rim	wtd. av ^{206}Pb/^{207}Pb	1649	133	242	0,08	1479	1,26	-19,0	7,3801	1,72	0,081653	2,92	7,4746	1,73	0,071997	4,69	986 ± 96	809 ± 13	803 ± 14	99,2
n6142-JT8-2-1	CL-D, Z	Concordant	753	337	169	0,45	48229	0,04	-3,9	5,3886	1,84	0,077930	0,40	5,3907	1,84	0,077636	0,41	1138 ± 8	1097 ± 19	1095 ± 20	96,4
n6142-JT8-1-1	CL-B, Z	Concordant	403	336	102	0,83	9578	0,20	-2,6	5,2499	1,55	0,079590	0,85	5,2602	1,55	0,078111	0,89	1150 ± 18	1122 ± 16	1120 ± 17	97,6
JT10, Granodioritic gneiss, Death Valley																					
n6141JT10-17-1	CL-M, SZ	wtd av. ^{206}Pb/^{207}Pb	539	629	155	1,17	202232	0,01	0,3	4,9856	1,15	0,079202	0,36	4,9860	1,15	0,079132	0,37	1175 ± 7	1178 ± 12	1179 ± 13	100,2
n6141JT10-16-2	CL-D, rim, UZ	Concordant?	1600	591	368	0,37	18054	0,10	2,1	5,1172	1,49	0,078056	0,22	5,1225	1,49	0,077270	0,27	1128 ± 5	1150 ± 16	1151 ± 7	101,1
n6141JT10-16-1	CL-M, core, UZ	Pb loss	314	344	56,0	1,10	1664	1,12	-9,1	6,5901	1,20	0,080537	2,22	6,6650	1,20	0,071954	2,62	985 ± 53	901 ± 10	898 ± 11	91,5
n6141JT10-15-1	CL-B, SZ	wtd av. ^{206}Pb/^{207}Pb	185	261	58	1,41	82073	0,02	4,6	4,7801	1,64	0,079306	0,64	4,7811	1,64	0,079134	0,65	1175 ± 13	1224 ± 18	>1200	104,2
n6141JT10-14-1	CL-B, UZ	Pb loss	233	287	54	1,23	26958	0,07	-10,2	6,3290	1,64	0,074635	0,64	6,3334	1,64	0,074107	0,68	1044 ± 14	945 ± 14	941 ± 15	90,5
n6141JT10-13-1	CL-M, UZ	wtd av. ^{206}Pb/^{207}Pb	425	165	101	0,39	81932	0,02	4,4	5,0265	1,46	0,077304	0,81	5,0276	1,46	0,077131	0,81	1125 ± 16	1169 ± 16	1172 ± 17	103,9
n6141JT10-13-2	CL-D, rim, UZ	Concordant	1073	100	220	0,09	360942	0,01	-1,2	5,3740	1,25	0,076698	0,27	5,3742	1,25	0,076658	0,27	1112 ± 5	1100 ± 13	1099 ± 13	98,9
n6141JT10-11-1	CL-D, weakly Z	inheritance?	1861	1708	583	0,92	95010	0,02	4,0	4,3292	1,24	0,084158	0,26	4,3301	1,24	0,084010	0,27	1293 ± 5	1339 ± 15	>1200	103,5
n6141JT10-10-1	CL-D, Z	>5 % rev. discordance	3647	1605	912	0,44	23017	0,08	8,9	4,7874	1,15	0,077954	0,31	4,7913	1,15	0,077338	0,33	1130 ± 6	1222 ± 13	>1200	108,1
n6141JT10-9-1	CL-B, Z	Pb loss	186	73	40	0,39	51448	0,04	-7,1	5,4925	2,21	0,078518	0,61	5,4945	2,21	0,078243	0,63	1153 ± 12	1078 ± 22	1074 ± 23	93,5
n6141JT10-9-2	CL-D, rim, UZ	Concordant	2635	308	553	0,12	69950	0,03	1,7	5,2888	1,10	0,076359	0,22	5,2902	1,10	0,076156	0,23	1099 ± 5	1116 ± 11	1117 ± 12	101,5
n6141JT10-8-1	CL-D, UZ	wtd av. ^{206}Pb/^{207}Pb	893	726	234	0,81	310793	0,01	1,0	5,0332	1,29	0,078472	0,92	5,0335	1,29	0,078427	0,92	1158 ± 18	1168 ± 14	1169 ± 15	100,9
n6141JT10-7-1	CL-D, Z, mix M-D mantle	rev. discordance	1424	494	325	0,35	54378	0,03	3,6	5,1727	1,29	0,076555	0,23	5,1745	1,29	0,076294	0,23	1103 ± 5	1139 ± 13	1141 ± 14	103,3
n6141JT10-6-1	CL-D, UZ	>5 % rev. discordance	1868	1747	476	0,94	4732	0,40	7,5	5,1467	2,56	0,077947	0,42	5,1672	2,57	0,074941	0,50	1067 ± 10	1140 ± 27	1145 ± 28	106,8
n6141JT10-5-1	CL-D, UZ	>10% rev. discordance	3101	937	771	0,30	143128	0,01	17,7	4,7869	2,38	0,074543	0,34	4,7875	2,38	0,074443	0,34	1053 ± 7	1223 ± 27	>1200	116,1
n6141JT10-4-1	CL-D, UZ	>10% rev. discordance	7700	18750	2900	2,44	122096	0,02	58,9	4,1249	10,08	0,069677	2,49	4,1255	10,08	0,069559	2,49	915 ± 51	1399 ± 128	>1200	152,9
n6141JT10-3-1	CL-D, UZ	Pb loss	842	557	148	0,66	8585	0,22	-8,3	6,2334	1,29	0,075502	0,37	6,2470	1,29	0,073842	0,70	1037 ± 14	957 ± 11	954 ± 12	92,3
n6141JT10-2-1	CL-D, Z	Pb loss	386	141	81	0,37	89587	0,02	-6,1	5,6544	1,67	0,076831	1,54	5,6555	1,67	0,076672	1,55	1113 ± 31	1050 ± 16	1046 ± 17	94,3
n6141JT10-1-1	CL-D, weakly Z	Pb loss	448	182	83	0,41	68924	0,03	-10,9	6,4652	1,56	0,073833	0,71	6,4670	1,56	0,073627	0,72	1031 ± 15	927 ± 13	923 ± 14	89,9

JT25, Granitic-granodioritic gneiss, Sesseggen																				
N6143-JT25-1-1	CL-D, Z	Concordant	443	389	114	0,88	97837	0,02	0,4	5,2041	1,38	0,077428	0,41	5,2051	1,38	0,077283	0,42	1129 ± 8	1133 ± 14	1133 ± 15	100,3
N6143-JT25-2-1	CL-D, Z, parallel	Concordant	170	157	43	0,92	29003	0,06	-3,2	5,3325	2,42	0,078234	0,96	5,3359	2,42	0,077745	0,99	1140 ± 20	1107 ± 25	1106 ± 26	97,1
N6143-JT25-3-1	CL-D, Z, parallel?	Concordant	165	91	41	0,55	69206	0,03	3,3	5,0384	1,39	0,077658	0,66	5,0398	1,39	0,077453	0,67	1133 ± 13	1167 ± 15	1169 ± 16	103
N6143-JT25-4-1	CL-D, Z, parallel	Concordant	254	255	68	1,00	64997	0,03	2,3	5,1224	1,49	0,077391	0,53	5,1238	1,49	0,077172	0,55	1126 ± 11	1149 ± 16	1151 ± 17	102
N6143-JT25-5-1	CL-M, Z, weakly parallel	Concordant	220	213	59	0,97	66928	0,03	2,0	5,0513	1,21	0,078074	0,78	5,0527	1,21	0,077863	0,79	1143 ± 16	1164 ± 13	1165 ± 14	101,8
N6143-JT25-6-1	CL-D, Z	Concordant	160	99	40	0,62	55327	0,03	2,2	5,0994	1,24	0,077645	0,67	5,1011	1,24	0,077389	0,69	1131 ± 14	1154 ± 13	1155 ± 14	102
N6143-JT25-7-1	CL-D, Z, parallel?	Concordant	440	588	126	1,34	43167	0,04	0,9	5,1269	1,15	0,078031	0,70	5,1292	1,15	0,077703	0,71	1139 ± 14	1148 ± 12	1149 ± 13	100,8
N6143-JT25-8-1	CL-D, Z, weakly parallel	Concordant	397	377	107	0,95	116148	0,02	2,2	5,0376	1,32	0,078018	0,61	5,0384	1,32	0,077896	0,61	1144 ± 12	1167 ± 14	1168 ± 15	102
N6143-JT25-9-1	CL-M, core, Z, parallel	Concordant	282	290	78	1,03	56682	0,03	3,3	4,9927	1,51	0,078050	0,55	4,9944	1,51	0,077800	0,57	1142 ± 11	1177 ± 16	1179 ± 17	103,1
N6143-JT25-10-1	CL-D, UZ	>5% rev. discordance, highU	1487	33	138	0,02	145215	0,01	7,5	11,4282	2,10	0,057439	0,49	11,4296	2,10	0,057339	0,50	505 ± 11	541 ± 11	541 ± 11	107,1
N6143-JT25-11-1	CL-D, core, Z	Concordant	372	380	99	1,02	35049	0,05	0,4	5,1846	1,26	0,077840	0,44	5,1874	1,26	0,077436	0,50	1132 ± 10	1136 ± 13	1137 ± 14	100,3
N6143-JT25-12-1	CL-D, core, UZ	>5% rev. discordance	466	351	123	0,75	41744	0,04	7,1	4,9202	1,55	0,077297	0,55	4,9224	1,55	0,076957	0,57	1120 ± 11	1192 ± 17	1197 ± 18	106,4
N6143-JT25-12-2	CL-mix bright and dark mantle	Concordant	282	223	72	0,79	16352	0,11	1,4	5,1036	1,37	0,078521	0,52	5,1094	1,37	0,077655	0,62	1138 ± 12	1152 ± 15	1153 ± 15	101,2
N6143-JT25-13-1	CL-B, UZ?	>5% rev. discordance	117	63	29	0,54	48310	0,04	5,9	5,0030	1,20	0,077008	0,79	5,0049	1,20	0,076714	0,81	1114 ± 16	1174 ± 13	1178 ± 14	105,4
N6143-JT25-15-1	CL-D, Z, parallel	Concordant	549	516	148	0,94	94290	0,02	1,8	5,0583	1,18	0,078030	0,37	5,0593	1,18	0,077880	0,37	1114 ± 7	1163 ± 13	1164 ± 13	104,4
N6143-JT25-14-1	CL-B, rim, UZ	>10% rev. discordance	347	72	53	0,21	1129	1,66	120,9	7,1082	1,70	0,067440	1,08	7,2280	1,72	0,054494	6,77	392 ± 152	835 ± 14	848 ± 14	213
JT27, Granitic gneiss, Jutulhogget-SE																				
N6146-JT27-17-1	CL-D, Z?	Pb loss	3573	1473	247	0,41	11400	0,16	-15,9	17,2156	5,15	0,056717	0,33	17,2439	5,16	0,055437	0,44	430 ± 10	363 ± 18	363 ± 18	84,4
N6146-JT27-16-1	CL-D, Z?	Concordant	2807	1328	270	0,47	32365	0,06	1,5	12,4600	0,96	0,057415	0,45	12,4672	0,96	0,056965	0,49	490 ± 11	497 ± 5	497 ± 5	101,4
N6146-JT27-15-1	CL-D, Z?	Concordant	905	216	83	0,24	297	6,29	4,0	11,5653	1,41	0,105768	2,14	12,3413	1,47	0,056795	5,56	484 ± 123	502 ± 7	503 ± 8	103,7
N6146-JT27-14-1	CL-D, Z?	Concordant	1600	46	137	0,03	99663	0,02	-0,3	12,4804	0,99	0,057325	0,39	12,4828	0,99	0,057178	0,40	498 ± 9	497 ± 5	497 ± 5	99,8
N6146-JT27-13-1	CL-D, Z?	Concordant	1960	1141	195	0,58	1092	1,71	3,5	12,1831	1,23	0,070149	1,62	12,3955	1,25	0,056807	3,13	484 ± 69	500 ± 6	500 ± 6	103,3
N6146-JT27-12-1	CL-D, Z?	>5% rev. discordance	4229	3564	443	0,84	42133	0,04	5,4	12,4923	4,97	0,056840	0,33	12,4979	4,97	0,056494	0,36	472 ± 8	496 ± 24	497 ± 24	105,1
N6146-JT27-11-1	CL-D, Z?	>5% rev. discordance	5116	3378	545	0,66	189702	0,01	5,8	11,8310	3,19	0,057180	0,22	11,8322	3,19	0,057103	0,23	496 ± 5	523 ± 16	523 ± 16	105,4
N6146-JT27-9-1	CL-D, Z?	>10% rev. discordance	1689	420	155	0,25	4320	0,43	11,3	12,3356	1,78	0,059353	1,16	12,3893	1,79	0,055977	2,09	451 ± 46	500 ± 9	501 ± 9	110,9
N6146-JT27-10-1	CL-D, Z?	>5% rev. discordance	3094	2619	343	0,85	34890	0,05	6,6	11,8881	1,36	0,057361	0,41	11,8944	1,36	0,056943	0,43	489 ± 10	520 ± 7	521 ± 7	106,3
N6146-JT27-8-1	CL-D, Z?	>5% rev. discordance	4176	4753	468	1,14	44773	0,04	6,7	11,9929	1,06	0,057158	0,24	11,9979	1,06	0,056832	0,27	485 ± 6	516 ± 5	517 ± 5	106,4
N6146-JT27-6-1	CL-D, Z?	Pb loss, highU and Th	6100	6309	379	1,03	4886	0,38	-10,4	21,1780	5,89	0,056020	0,66	21,2594	5,91	0,053025	0,84	330 ± 19	296 ± 17	296 ± 17	89,7
N6146-JT27-7-1	CL-D, Z?	Concordant	1490	194	131	0,13	24775	0,08	0,3	12,5043	1,05	0,057653	0,47	12,5138	1,05	0,057065	0,50	494 ± 11	496 ± 5	496 ± 5	100,4
N6146-JT27-5-1	CL-D, Z?	Concordant	2825	2433	306	0,86	18072	0,10	1,0	12,2140	1,04	0,058071	0,96	12,2266	1,04	0,057265	1,04	502 ± 23	507 ± 5	507 ± 5	101,1
N6146-JT27-4-1	CL-D, Z?	Concordant	685	56	59	0,08	154916	0,01	-1,6	12,6529	1,05	0,057264	0,69	12,6545	1,05	0,057170	0,69	498 ± 15	490 ± 5	490 ± 5	98,4
N6146-JT27-3-1	CL-D, Z?	>10% rev. discordance	767	90	67	0,12	1014	1,85	23,0	12,2875	1,18	0,069248	2,76	12,5185	1,19	0,054841	4,96	406 ± 111	495 ± 6	497 ± 6	121,9
N6146-JT27-2-1	CL-D, Z?	Concordant	882	383	81	0,43	9527	0,20	-0,3	13,0136	2,37	0,058173	0,51	13,0392	2,38	0,056643	0,61	478 ± 13	476 ± 11	476 ± 11	99,6
N6146-JT27-1-1	CL-D, Z?	Pb loss, High common Pb	2646	2480	291	0,94	896	2,09	-8,8	12,0526	0,96	0,074769	3,65	12,3096	0,97	0,058547	6,57	550 ± 144	504 ± 5	503 ± 5	91,6
JT35, Migmatitic gneiss, Klåvingen																				
N6145-JT35-1-1	CL-B, Z	Concordant	156	50	33	0,32	32762	0,06	0,6	5,5263	1,85	0,075333	1,16	5,5295	1,85	0,074898	1,18	1066 ± 24	1072 ± 18	1072 ± 19	100,6
N6145-JT35-2-1	CL-D, Z?	Discordant, high common Pb	1402	714	209	0,51	870	2,15	-12,6	7,5221	7,80	0,085329	1,66	7,6874	7,97	0,068847	4,20	894 ± 87	788 ± 59	785 ± 60	88,1
N6145-JT35-3-1	CL-M. Z	Pb loss	518	211	98	0,41	2857	0,65	-9,2	6,0263	1,13	0,080220	1,02	6,0660	1,13	0,075243	1,21	1075 ± 24	984 ± 10	980 ± 11	91,5
N6145-JT35-4-1	CL-D, weakly Z	Concordant	766	152	156	0,20	46364	0,04	-1,0	5,5835	2,24	0,075425	0,32	5,5857	2,24	0,075118	0,34	1072 ± 7	1062 ± 22	1061 ± 23	99,1
N6145-JT35-5-1	CL-D, UZ	Pb loss	2538	132	246	0,05	2731	0,68	-10,4	10,9507	1,39	0,065805	0,78	11,0262	1,40	0,060495	1,03	621 ± 22	560 ± 8	558 ± 8	90,2
N6145-JT35-6-1	CL-D, Z	Pb loss	2828	550	322	0,19	1574	1,19	-22,1	9,6742	3,26	0,074780	0,64	9,7905	3,29	0,065632	1,24	795 ± 26	627 ± 20	623 ± 20	78,9
N6145-JT35-7-1	CL-D, weakly Z	>5% rev. disc, highPb incl or zoning	2470	441	295	0,18	766	2,44	21,6	8,9699	2,69	0,077563	2,49	9,1944	2,74	0,058594	8,27	552 ± 181	666 ± 17	668 ± 18	120,6
N6145-JT35-8-1	CL-D, UZ	Pb loss	4945	9	[337]	0,002	2264	0,83	-5,5	15,5089	6,19	0,061689	2,66	15,6381	6,24	0,055241	4,65	422 ± 104	400 ± 24	399 ± 24	94,8
N6145-JT35-9-1	CL-D, UZ	Pb loss	2537	553	335	0,22	3730	0,50	-16,3	8,5707	1,73	0,070851	0,36	8,6139	1,73	0,066997	0,64	838 ± 13	708 ± 12	704 ± 12	84,5
N6145-JT35-10-1	CL-D, core, UZ	Discordant, high common Pb	955	874	180	0,92	652	2,87	-6,7	6,3958	1,10	0,093450	0,46	6,5848	1,10	0,071517	0,90	972 ± 18	911 ± 9	909 ± 10	93,7
N6145-JT35-11-1	CL-D, core, UZ	Concordant	637	260	135	0,41	20153	0,09	-1,9	5,6165	1,43	0,075906	0,70	5,6217	1,43	0,075200	0,72	1074 ± 15	1055 ± 14	1054 ± 15	98,2
N6145-JT35-12-1	CL-B, Z	Pb loss	1224	360	200	0,29	1820	1,03	-11,7	7,0521	1,64	0,078623	0,64	7,1253	1,65	0,070761	1,07	951 ± 22	847 ± 13	843 ± 13	89,1
N6145-JT35-13-1	CL-D, UZ	Pb loss	3367	1116	366	0,33	2697	0,69	-19,5	10,7024	2,31	0,068218	2,76	10,7772	2,33	0,062859	3,65	703 ± 78	572 ± 13	569 ± 13	81,4
N6145-JT35-14-1	CL-M, core, UZ	Pb loss	1170	273	140	0,23	1233	1,52	-9,7	9,2519	3,10	0,075028	0,86	9,3944	3,14	0,063310	1,69	719 ± 36	652 ± 20	650 ± 20	90,7
N6145-JT35-15-1	CL-D, Z	Pb loss	668	130	104	0,20	4316	0,43	-9,9	7,2382	2,33	0,072898	0,76	7,2697	2,33	0,069579	0,86	916 ± 18	831 ± 18	828 ± 19	90,7
N6145-JT35-16-1	CL-D, core, UZ	Concordant	843	371	177	0,44	25966	0,07	-3,1	5,7808	1,26	0,075167	0,41	5,7850	1,26	0,074619	0,44	1058 ± 9	1028 ± 12	1026 ± 12	97,2
N6145-JT35-17-1	CL-D, core, UZ	Discordant, high common Pb	631	279	110	0,44	796	2,35	-11,9	6,5917	1,18	0,090475	2,90	6,7502	1,18	0,072552	5,77	1001 ± 117	891 ± 10	886 ± 11	89
N6145-JT35-18-1	CL-mix M-D mantle	Pb loss	745	172	128	0,23	20775	0,09	-10,7	6,6826	1,18	0,073122	0,37	6,6886	1,18	0,072435	0,41	998 ± 8	898 ± 10	894 ± 10	90,1

1: CL = Cataluminisence, B = bright, M = Moderate, D = Dark, UZ = unzoned, Z = Zoned (osciallltory zoned), SZ = sector zoned.

2: Ratios are based on the measured Th and U signals.

3: f206 is the precentage of common Pb estimated from 204Pb counts; in parentheses these are insignificant.

4: Positive numbers are reverse discordance.

5: Ratios after correction. The samples used 207-corrected ratios.

6: Age based on projecting a line in inverse concordia diagram from assumed common Pb through the total (uncorrected) ratios into concordia (Ludwig, 2012).

*7: Concordance in %. Measured from calculating (206Pb/238U ages / 207Pb/206Pb ages) * 100.*

Analyses which are greyed-out represents analyses with >10% discordance and are omitted from the concordia plots.